IntechOpen

Copper
From the Mineral to the Final Application

Edited by Daniel Fernández-González
and Luis Felipe Verdeja González

Copper - From the Mineral to the Final Application

Edited by Daniel Fernández-González and Luis Felipe Verdeja González

Notice

Statements and opinions expressed in the chapters are these of the individual contributors and not
necessarily those of the editors or publisher. No responsibility is accepted for the accuracy of
information contained in the published chapters. The publisher assumes no responsibility for any
damage or injury to persons or property arising out of the use of any materials, instructions, methods
or ideas contained in the book.

We are IntechOpen,
the world's leading publisher of
Open Access books
Built by scientists, for scientists

6,700+
Open access books available

181,000+
International authors and editors

195M+
Downloads

156
Countries delivered to

Our authors are among the
Top 1%
most cited scientists

12.2%
Contributors from top 500 universities

CLARIVATE ANALYTICS
BOOK CITATION INDEX
INDEXED

WEB OF SCIENCE™

Selection of our books indexed in the Book Citation Index
in Web of Science™ Core Collection (BKCI)

Interested in publishing with us?
Contact book.department@intechopen.com

Meet the editors

Daniel Fernández-González graduated with a bachelor's and master's degree in mining engineering in 2013, and he earned a Ph.D. in Materials from the Oviedo School of Mines, Energy, and Materials at the University of Oviedo, Spain, in 2019. He has worked as a researcher at the Nanomaterials and Nanotechnology Research Center, Spanish National Research Council since 2021. His research deals with the synthesis of materials, the production of metals, ceramics, and composite materials, and the characterization of materials. He has also focused on sustainable metallurgical processes based on solar energy and the recycling of industrial wastes. He has published forty articles and six books. He has been a visiting researcher at the Universidad Panamericana, Mexico, the AGH University of Science and Technology, Poland, and the Processes, Materials and Solar Energy (PROMES) laboratory, National Centre for Scientific Research (CNRS), France. He has participated in different research projects on materials synthesis and sintering funded by public agencies and private companies.

Luis Felipe Verdeja González is a Professor of Materials Science and Metallurgy and Head of the Siderurgy, Metals and Materials Group at the University of Oviedo. He was previously the head of the Department of Materials Science and Metallurgical Engineering, University of Oviedo, Spain. He is a member of the American Ceramic Society, The Minerals, Metals, and Materials Society, Iron and Steel Institute of Japan, and the Institute of Materials, Minerals and Mining. His research focuses on the application, maintenance, and wear of refractory linings in blast furnaces and other metal and steel production processes, and non-ferrous extractive metallurgy. He has published more than 100 articles and 9 books and has participated in more than 40 public and private research projects.

Contents

Preface

Copper has accompanied human development for thousands of years in different fields and forms. During the Copper Age, copper was employed in its native form. Later, bronze comprising copper and tin was discovered. The wide utilization of copper in the form of this alloy, and some others that appeared later, including brass (Cu-Zn) or alpaca (Cu-Ni-Zn), highlighted copper metallurgy's importance. These alloys were widely used in bells, ornamental parts, weapons, body armors, and more due to their excellent properties, including their high mechanical, corrosion, and wear resistance. In addition, the discoveries of Michael Faraday in the electricity field represented a new use for copper. He constructed the first electrical generator, and subsequent developments in electricity led to the current importance of copper as an electrical conductor. This widespread use of copper in the field of electrical conduction, and in heat transfer applications, has led to an increase in copper production. Copper is being used in new applications, such as those in biomedicine, increasing its importance as a fundamental functional material.

Written by expert researchers from around the world, this book is organized into two sections: "Copper Mining and Processing" and "Copper Applications." Section 1, "Copper Mining and Processing", includes three chapters dedicated to copper mining and metallurgy.

Chapter 1 provides an overview of copper, from the ore to the final metal. It includes a description of the main ores, the technologies used to produce copper, and its final applications. The chapter concludes with a novel process of copper extraction from slags using solar energy.

Chapter 2 focuses on a theoretical and experimental study of an electroosmotic drainage technique applied to copper mining. It provides an interesting study about water permeability in a copper mine pile.

Chapter 3 emphasizes the refractory lining of the furnaces used to produce copper. It analyzes the different processes and materials and how they interact with the refractories. It also describes the families employed in copper metallurgy.

Section 2, "Copper Applications", includes four chapters on different copper applications in different fields.

Chapter 4 analyzes the problem of halogenated organic compounds and how to deal with them using a system comprising metallic copper and borohydride as an alternative to nano zerovalent iron (nZVI) and palladium (Pd). This system might be an attractive alternative for the treatment of water and wastewater.

Chapter 5 studies the influence of non-covalent interactions on the complexes formed by various biomolecules with the copper cation using the method of density functional theory. This study is interesting for biomedical applications.

Chapter 6 focuses on additive manufacturing applied to copper. It describes the relevant technologies and applications while examining the current technological gaps and proposing strategies to overcome them.

Finally, Chapter 7 concludes with a study of modelling and theoretical aspects of copper-nickel alloy.

The process of publishing this book was long and complicated and thus I want to thank everyone for their support. Moreover, I want to acknowledge the authors for their interesting contributions, willingness to share their research and experience, and for their hard work in making this book possible. I also want to acknowledge Professor of Metallurgy Luis Felipe Verdeja from the Oviedo School of Mines, University of Oviedo, Spain for his support during the preparation of this book. Finally, I want to express my gratitude to IntechOpen for the initiative to publish this book about copper. Edited books are always a good platform to share knowledge from a multidisciplinary point of view.

Daniel Fernández-González
Center for Research in Nanomaterials and Nanotechnology-Spanish
National Research Council (CINN-CSIC),
El Entrego, Asturias, Spain

Luis Felipe Verdeja González
University of Oviedo,
Oviedo-Uviéu, Asturias, Spain

Section 1

Copper Mining and Processing

Chapter 1

Copper Overview: From the Ore to the Applications – A Case Study of the Application of Concentrated Solar Energy to the Treatment of Copper Metallurgy Slags

Daniel Fernández-González and Luis Felipe Verdeja González

Abstract

Copper is a metal that is widely used in different applications mainly due to its thermal and electrical conductivities, together with its corrosion resistance, particularly when it is alloyed. This chapter intends to be a summary of the copper metallurgy: from the historical aspects and mineral deposits or statistics to the different technologies used to produce metallic copper together with the distinct applications (of copper and copper alloys). Environmental issues are deeply rooted in industrial policies to improve the recovery of the metal as well as to minimize the residues generated in the process, which are a problem from the environmental point of view but also from the economic standpoint. Therefore, this document concludes with a research work carried out with the aim of treating copper slags with concentrated solar energy to recover valuable elements from these slags, as iron and copper. Results from this investigation suggest that solar energy could have an enormous potential in the copper metallurgy.

Keywords: copper slag cleaning, copper metallurgy, electrowinning, flash smelting, copper applications

1. Introduction

Copper has been associated to the human history from the moment when it was discovered in native state. It was the first metal used by humans and the second most used after iron through the ages. The name "copper" derives from the Latin word "cuprum", and this word comes from the Roman name of the island Cyprus, where copper was extracted in that period. Nevertheless, there is a historic period known as the Chalcolithic or Copper Age, also termed as the Eneolithic or Aeneolithic, now

regarded as part of the broader Neolithic, where copper was used for utensils, ornaments, tools, and weapons before the Roman Empire appearance. In the Chalcolithic period, copper predominated in metalworking technology and can be defined as a transitional period between the Neolithic and the Bronze Age, where humans discovered that by adding tin to copper, it was possible to create bronze, a metal alloy harder and stronger than either component. Anyway, the utilization of copper significantly increased in the nineteenth and twentieth centuries with the spread of the electricity utilization. Nowadays, approximately 50% of the copper production is employed in the electric power industry and around 25% in construction. The main copper alloys are: brass (Cu-Zn), bronze (Cu-Sn), and cupronickels (Cu-Ni) or aluminum bronze (Cu-Al), widely used in the naval industry and in several piping applications due to its corrosion resistance [1].

The chemical element copper is a reddish metal at the head of group IB in the periodic table, with oxidation states +1 and + 2. Its symbol is Cu; atomic number, 29; and atomic weight, 63.546. The physical properties of the copper depend on the purity as well as on the ore and on the process used to obtain it. This way, impurities in solid solution or segregated phases at the grain boundaries due to the treatment of the metal can have a relevant influence on the properties of the metal. Dislocations or substitutional solid solutions have a significant influence on the thermal and electrical conductivities of the copper, on the plastic behavior as well as on the corrosion resistance. This way, high-purity copper is very ductile; although work hardening increases the hardness and the resistance while the annealing reduces the hardening (elements in substitutional solid solution play the same role). Pure copper can be hot worked, without brittleness, but the resistance at high temperature is poor. Several impurities produce this deterioration of the resistance: S, Bi, Sb, Pb, and Se. The electrical conductivity of copper is the highest among the metals after silver (0.6% of the electrical conductivity of this metal). Cu (2+) is the most stable state but above 800°C, Cu (1+) is more important, which is relevant in pyrometallurgical processes. Copper is a relatively noble element as it can be deduced from its high potential of standard reduction. It gets covered with a thin layer of cuprous oxide under dry air at room temperature. At high temperature (under air), cuprous oxide is first formed but cupric oxide appears later [1]. In the ambient atmosphere, copper surface oxidizes with the years and forms a thin layer, decorative and protective, of green color, mainly formed by basic carbonates and sulfates of copper, which is quite typical from the roofs of historical buildings in central Europe (**Figure 1**).

Copper in a dry atmosphere resists the attack of aggressive products although it exhibits great affinity for the halogen elements and sulfur. Non-oxidizing acids (sulfuric, hydrochloric, and other diluted organic) badly attack the copper. Copper is soluble in oxidizing acids such as nitric and chromic, and in non-oxidizing (sulfuric) having an oxidizing agent (such as oxygen or hydrogen peroxide). Pure water does not corrode copper, but sea water produces a moderate attack. Sulfides are attacked in hydrometallurgy using solutions of ferric salts. Regarding alkaline solutions, there is passivation and the attack at acid pH requires great potential. Oxygen solubility in liquid copper has certain importance. SO_2 dissolves in liquid copper and forms sulfides. Hydrogen is soluble in liquid copper and also remains dissolved after the solidification, being the quantity controlled by reaction with the oxygen (forms water vapor that evaporates and generates residual porosity). Hydrocarbons do not, in general, react with the copper except acetylene. **Table 1** collects the values of several important physical and chemical properties of the copper [1].

Figure 1.
Greenish roofs made of copper and covered with a layer of basic carbonates and sulfates of copper.

Property	Value					Property	Value
Density (g/cm^3)	9.0981–5.7385·10^{-4}·T (theoretical) 8.96 (99.999% Cu) at 20°C (pure) 7.99 at 1083°C (liquid)					Young's modulus (GPa)	100–120 (annealed); 120–130 (cold work)
Melting point (°C)	1083					Elongation (%)	30–40 (annealed); 3–5 (cold work)
Boiling point (°C)	2595					Tensile strength (MPa)	200–250 (annealed); 300–360 (cold work)
Latent heat of fusion (J/g)	211					Brinell hardness (HB)	40–50 (annealed); 80–110 (cold work)
Latent heat of volatilization (J/g)	4.813					Electron configuration	[Ar] 3d^{10}4s^1
Average specific heat (J/g·K)	0.385					Crystalline system	Face centered cubic
Thermal conductivity (W/m·K)	T (°C)	−100	0	20	100	200	Isotopes	^{63}Cu (68.94%) and ^{65}Cu (31.06%)
		435	398	394	385	381		
Electrical conductivity (MS/m)	T (°C)	−100	0	20	100	200	Ionic radius (nm)	(+1): 0.096; (+2): 0.069
		110	60	58	44	34		
Magnetic susceptibility (cm^3/g)	−0.085·10^{-6} (20 °C)					Standard potential of reduction (V)	Cu^{2+}/Cu^0:+0.338; Cu^{1+}/Cu^0:+0.512
Coefficient of thermal expansion (1/K)	16.9·10^{-6} (0–100°C)					Electronegativity	1.9

Table 1.
Physical and chemical properties of the copper.

2. Deposits, minerals, and trends

First copper utensils, ornaments, tools, and weapons were manufactured with casted native copper, but soon other techniques were applied to use other copper sources. In this line, around 80% of the copper that is mined nowadays comes from low-grade ores containing 2% or less of Cu. In this way, even when the copper sulfides metallurgy is relatively recent, it is possible that a few centuries BC metallic copper was obtained from a matte by means of repeated roasting and smelting cycles. This method was applied for centuries, and it was not until the 19th century when the reductant capacity of sulfur was considered. Anyway, before starting with the copper metallurgy, it is convenient to introduce the main copper minerals because they define the process that is nowadays used to produce metallic copper. In fact, copper content in the Earth's crust reaches 70 ppm. This way, more than 160 minerals that contain copper are known but only two main families have importance: oxidized ore (cuprite, Cu_2O; tenorite, CuO) and mainly sulfide ores (chalcopyrite, $CuFeS_2$; bornite, Cu_5FeS_4; chalcocite, Cu_2S). Deposits are mined when the ores contain 0.5% Cu in open-pit mining and 0.7–6% Cu in underground mining. However, significant research is appearing in the field of complex copper ores due to the increasing demand and the potential depletion and decline of good copper ore grades. Low-grade sulfide ores are subjected to concentration operations, which include flotation, to obtain dry concentrates of around 30% of copper with 10–200 μm of grain size [1]. Within this context, it is possible to mention Velásquez-Yévenes and Lasnibat's research [2] about the simultaneous recovery of copper and manganese from "exotic-Cu" deposits in Chile, characterized by the refractoriness to dissolution under acidic and oxidative conditions, or the research of Godirilwe and collaborators about the extraction of copper from complex carbonaceous sulfide ore, characterized by their mineralogical complexity and impurities of organic carbon and carbonates [3]. Other research in this line that can be mentioned is that of Corin and coauthors about complex copper ore (sulfide, oxide, and mixed) in Zambia [4], or Liu and researchers that reported the beneficiation of complex copper oxide ores rich in malachite [5] or the research of Hu et al. about low-grade copper ores with high contents of oxide ore and carbonate gangue (malachite, chrysocolla, chalcopyrite, and chalcocite with gangue minerals as quartz, limonite, calcite, and dolomite) from Yunnan province in China [6].

Porphyry copper deposits are currently the largest source of copper ore. The copper reserves are estimated in 2021 in 880 Mt. (Million tons) according to the United States Geological Survey. Half of these reserves are concentrated in five countries: Chile (200 Mt), Australia (93 Mt), Peru (77 Mt), the USA (48 Mt), and China (26 Mt). Regarding the production/demand of copper, this has grown since the eighteenth century, particularly in the last decades: 10000 tons in 1700, 18,000 tons in 1800, 450,000 tons in 1900, 2.5 Mt. in 1950, 4.5 Mt. in 1960, 7.3 Mt. in 1970, 9.3 Mt. in 1980, 10.9 Mt. in 1990, 15.1 Mt. in 2000, 19.1 Mt. in 2010, 23.1 Mt. in 2015, and 25.3 Mt. in 2020 (year with production significantly affected by the COVID-19 pandemic situation; the estimation for 2021 was 26 Mt). These values refer to the total consumption/production of copper, but it is important to make a distinction between copper mine production and refined copper. This way, approximately 80% of the copper produced worldwide comes from copper extracted from mining operations. Regarding the principal mine copper producers, the main countries are (2021): Chile, 5.6 Mt.; Peru, 2.2 Mt.; China, 1.8 Mt.; USA, 1.2 Mt.; Australia, 0.9 Mt. Regarding the main refinery copper producers of copper, it is possible to indicate (2021): China, 10 Mt.; Chile, 2.2 Mt.; Japan, 1.5 Mt.; the USA, 1 Mt.; Germany, 0.63 Mt.; Australia, 0.45

Mt.; Peru, 0.35 Mt. With respect to the price, the minimum price in 10 years was reached in December 2015 (4577 $/ton) and March, 2020 (4789 $/ton, coincident with the quarantine period resulted from COVID-19), while the maximum price in 10 years was reached in March 7, 2022 (10,729 $/ton, after the Russian invasion of Ukraine).

Aligned with the above-mentioned questions, the equilibrium between the supply and the demand of raw materials or semifinished and finished products is almost unattainable. The reasons of this disequilibrium can be explained by an irrational gathering of raw materials, a sanitary problem (i.e., COVID-19), or military reasons (i.e., Russian invasion of Ukraine). Basic resources (materials, energy, and food) are the first resources in being affected in one or other manner by the distortions of the markets, and this has a significant impact on the development of the poorest countries and regions, in the growth of emerging countries and regions and in the sustainability of developed countries and regions. In this line, countries are identifying strategical minerals or elements whose scarcity would have a significant impact on the chain value. Copper is one of these elements. This metal has still enormous importance in the market despite of its utilization for hundreds of years. In fact, it has gained significant interest in the last centuries due to the electricity market and, it will probably attract more interest with the development of both the sustainable methods of producing electricity and the electric vehicles. In this context, considering the data of the National Renewable Energy Laboratory (NREL) of the USA, 0.7–1.8 tons of copper and 110 tons of steel are required for each MW of installed wind energy [7].

In general, it is important for the beneficiation of the basic resources, particularly copper, to study the evolution of the price of the raw materials in a period of time comparable to the proposed duration of the project (development, exploitation, and conclusion). For this reason, it is realistic to analyze the copper market from 1980 [8]. The copper price in 1980, which approximately coincided with the end of the second oil crisis, was 2400 $/ton, while in 1995 it was not far from the price in 1980: 2976 $/ton. However, the irrational development of the real-estate market in the period 1995–2010 made the copper price to grow 2.2 times, while in the period 1980–1995, the growth was only 0.24 times. After the real-estate bubble, the price descended to a minimum of 4553 $/ton in 2015 and started to progressively grow up to an average value around 6000 $/ton before another minimum coincident with the COVID-19 lockdown in March 2020 in 4789 $/ton. The copper price has sharply grown since that minimum until reaching values never seen before, after the Russian invasion of Ukraine (>10,000$/ton). It is possible to think, as it is indicated by Brinded [9], that the copper market is mad. Maybe this term is not the most adequate because it sounds better to say that the copper market is in crisis. There is not a single reason to justify this situation, but it is necessary to consider several variables in the implementation of a mining project: the price of the metal in the London Metal Exchange, the tons of proven metal reserves in the deposit, and the grade-concentration of the metal in the proven reserves. Therefore, it seems not reasonable to start a mining project considering only the highest prices in the market but an average value over a long period (and different scenarios) together with the other variables indicated in this paragraph, as otherwise, for instance, projects started under the current copper prices could lead the mining project to fail whether the prices descend. Moreover, the project should consider its complete duration (from the early stages of reserves estimation to the land rehabilitation after the end of the project). Therefore, economic resources obtained from the sale of the metal in the market are approximately distributed as follows: 14% for the exploration, 44% for the mining-exploitation-concentration operations and environmental conservation, 23% for the extractive metallurgy, 6% for general costs

and management of the project, and 13% of economic profit, for successful project implementation, based on previous works within this field and considering the economic evaluation of mine implementation projects [10, 11].

3. Copper metallurgy and refining

### 3.1 Introduction

The primary source of Cu is porphyry deposits. The treatment of primary copper ores by the pyrometallurgical process is responsible for about 80% of the world's copper production [12]. However, the production of copper taking advantage of copper sulfides' characteristics is relatively recent. The production of copper in the Middle Age (as it is collected in *De Re Metallica* of Georgius Agricola) was based on the Mansfeld process, which involved seven operations of roasting and melting. First, the slagged gangue was separated from the matte with low metallic content, and then, this was enriched by concentrating smelting, carrying to the slag, by oxidation, the iron content. The enriched matte was dead roasted to obtain an oxide that was treated by reducing smelting to obtain black copper, which was later refined. It was in 1700 when the Welsh process was introduced, which significantly modified the method of obtaining copper. It consisted of 10 operations at the beginning, although it involved 6 or 7 stages in 1830. The main difference was the extensive utilization of the roasting process or double decomposition process, where sulfur was used as reductant reagent. At the beginning of the Modern Age, Germany was the leader in copper production, but in 1800 England became the biggest copper producer. Chile became the first copper producer in 1859 and, from that moment, this country is the biggest copper producer in the world. Even when, as we have already seen, copper has been produced for several centuries, the greatest developments in technique are from the last centuries: the application of air/oxygen blowing as in the Bessemer converter, the development in Finland of the flash smelting process after the World War II, industrial electrowinning in the second half of the nineteenth century or the discovery of the differential flotation of sulfides also in the second half of the nineteenth century. These developments, as well as the applications of copper in construction and electricity, have made this metal one of the five most produced worldwide [13].

3.2 Principles of the process used to obtain the matte

Pyrometallurgical copper smelting processes are based on the principle of partial oxidation of sulfide concentrates [1]. The methods based on the total oxidation of sulfides with posterior reduction of the metal oxide, without formation of a copper matter, are generally not used due to both the high consumption of combustible, the formation of copper-rich slags and the obtaining of crude copper with high level of impurities. This way, the smelting of sulfide concentrates, partially roasted or without roasting, with the addition of impurities, produces two immiscible phases: one heavy containing most of sulfides that is known as matte; other oxidized and ferrous is known as slag. The reactions of oxidation of the sulfur of sulfides and iron, both exothermic, produce the matte with adequate composition and it is possible to use the heat of the reaction if the suitable technology is used. The formation of the slag, by reaction of the iron (II) oxide with the silica, which is used as a flux to form fayalite

(main component of the slag) and separate the iron from the matte, is also exothermic. The reactions involved in the formation of the matte are described as follows:

$$4CuSFeS(s) + 5O_2(g) \leftrightarrow 2(Cu_2S \cdot FeS)(dis; matte) + 2FeO(s) + 4SO_2(g) \qquad (1)$$
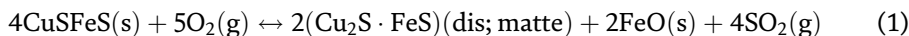
that is an exothermic reaction, as the next one:

$$2FeO(s) + SiO_2(s) \leftrightarrow 2FeO \cdot SiO_2(dis; slag) \qquad (2)$$

The most important equilibrium, between the phases (matte and slag), is the following one, which is displaced to the right side of the equation:

$$Cu_2O(dis; slag) + FeS(dis; matte) \leftrightarrow Cu_2S(dis; matte) + FeO(dis; slag) \qquad (3)$$
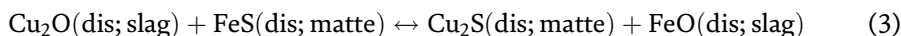
The presence in the matte of liquid iron sulfide reduces the iron (III) oxide to iron (II) oxide:

$$3Fe_3O_4(s) + FeS(s) \leftrightarrow 10FeO(s) + SO_2(g) \qquad (4)$$
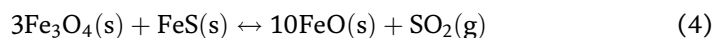
The previous reaction can be used to eliminate part of the magnetite, with the presence of silica because the magnetite is detrimental for the operations in the furnace due to its high melting point (>1500°C), which increases the viscosity of the slag and increases the quantity of copper in the slag.

Therefore, the process used to obtain the matte is a copper concentration process in this phase. There are several elements that accompany the copper that are essentially reduced. Thus, calcium, magnesium, and aluminum go directly to the slag, while precious metals go to the matte. The other metals, Ni, Co, Pb, Zn, As, Sb, Bi, etc., distribute between both phases or, separate with the gases of the furnace. The matte is fundamentally a mixture of sulfides in the pseudo binary Cu_2S-FeS system. The density of the matte is in the range of 4.9–5.3 g/cm^3 depending on the state (liquid or solid) and the copper content. On the contrary, the slag has a density 1 g/cm^3 lower and comprises a 30–40% of iron as oxides and 25–40% of silica, mainly as iron silicate (fayalite). The smelting process involves an almost complete separation of the matte and slag due to the different densities and the different nature of the chemical bonding (covalent in the matte and ionic in the slag). Some technologies of fusion (reverberatory furnace) produce slags with 0.6% of copper and others, as the flash smelting Outokumpu (introduced by this Finnish company) [1], produce slags with 1.2% of copper that must be treated by either reduction in an electric furnace with additions of carbon and pyrite or flotation after milling.

3.3 Traditional smelting of copper sulfides

The most traditional form of obtaining copper in the fifties of the twentieth century consisted in roasting the concentrates of sulfides and melting the products in reverberatory furnaces, sometimes in electric furnaces and less frequently in shaft furnaces. A matte was obtained, which was later subjected to oxidation in Pierce-Smith converters. The main advantage of this technology is the production of slags that can be directly sent to controlled landfill. Within this group of technologies, it is also possible to mention the Noranda and Teniente processes [1], which in fact are big converters adapted for the smelting to obtain the matte. In these technologies, the

concentrate is mixed and flows in a turbulent bath matte/slag; additionally, the Fe and S of the concentrate oxidize to form a rich matte, a slag that cannot be disregarded, and a gas with high SO_2 content. The matte (70–75% Cu) is sent to the converter to obtain blister copper. In the particular case of the Noranda process, it was set at the beginning as a continuous process to directly produce blister copper, but it failed. The idea/objective of obtaining copper in a single stage was one of the industrial research objectives for years, as we are going to see later. Returning to the Noranda process, the system involved the simultaneous presence of three phases (slag, matte, and metal) and, it was not possible to achieve a good recovery of copper from the slag. The metal was obtained with great contamination and, therefore, several problems arose during the electrowinning.

3.4 Flash smelting

The flash smelting is the dominant technology in the market. It can be autogenous or not, but the main characteristic is the rapidness of the smelting process resulting from the utilization of a burner with preheated air, enriched with oxygen, or with industrial oxygen. The process will be autogenous if the following condition is accomplished: the partial oxidation of sulphides generates enough heat to melt the matte and the slag and have them as separated phases in the furnace (due to density difference). Heat is usually provided to ensure the reactions matte-slag and the separation of both phases. In flash smelting, the stages of roasting and oxidizing smelting happen simultaneously taking advantage of the heat generated in the process. The only autogenous technology is the INCO process that uses industrial oxygen and a design of the furnace that allows copper slag with 0.7% Cu. The other technologies have the disadvantage of high copper content in the slag due to the high oxidizing environment of the process and the high quantities of magnetite in these conditions (which is in solid state when it is in excess), which makes it almost impossible to empty the slag from copper using the Eqs. (3) and (4).

The Outokumpu process of flash smelting is the most important technology to produce copper (8 of 20 biggest copper smelters according to the ICSG Directory of Copper Mines and Plants use this technology). This process was developed in Finland
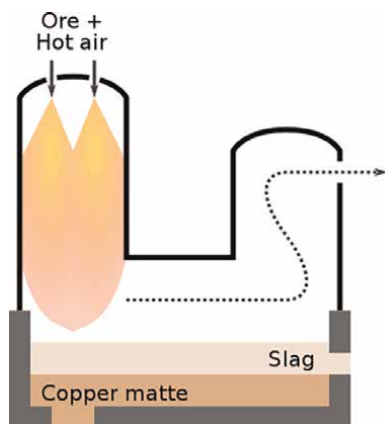
Figure 2.
Scheme of the Outokumpu smelting process (source: Wikicommons).

in the fifties of the last century and has great productivity and easy control. The scheme of the process appears in **Figure 2**.

The furnace can be divided into three sections [1]: tower, for the partial roasting and smelting of the dry concentrate in suspension; horizontal zone, where the matte and the slag are separated; and, chimney, for the exit of gases that end in the acid plant after pretreatments to use the heat and remove the particulate matter. The process in the tower is almost autogenous but the heat for the separation of the matte and the slag is provided by gas or fuel. The copper content in the slag is around 2% of copper, which involves a posterior treatment in an electric furnace with pyrite and carbon to reduce the copper content in the slag (the slag can be sold as abrasive or material for roads). The hot gases collected in the process are used in a boiler and the powders that they contain are collected with mechanical separators or electrostatic filters. These powders (5–10%) are recycled again in the furnace or treated depending on the concentration of volatile elements.

Other technologies of flash smelting are the INCO process, cyclonic smelting KIVCET, Isasmelt process, Vanyukov process, and Contop process.

3.5 Conversion

Conversion is the process where the matte generated in the smelting process, which is in molten state, is treated by injecting oxygen to the melt, mainly in Peirce-Smith converters. The process consists of two stages:

- The first is known as "slagging stage" and a phase formed essentially by copper sulfides, white metal, where there are less than 1% of iron sulfides, is obtained. The converter is filled again with copper matte to obtain more white metal by oxygen injection. The process is repeated several times (5 or 6 [1]) until the moment when the converter is filled with copper sulfide. The main reaction of this first stage is:

$$2FeS(dis; matte) + 3O_2(g) \leftrightarrow 2FeO(dis; slag) + 2SO_2(g) \qquad (5)$$
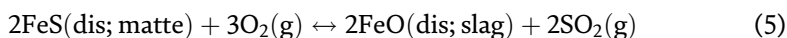
The ferrous slag of the first stage is separated, normally, by addition of silica (fayalite) as in the Eq. (2).

- The second stage allows obtaining blister copper by oxygen injection to the white metal. The reactions in this stage are:

$$2Cu_2S(dis) + 3O_2(g) \leftrightarrow 2Cu_2O(dis) + 2SO_2(g) \qquad (6)$$

$$2Cu_2O(dis) + Cu_2S(dis) \leftrightarrow 6Cu(l) + SO_2(g) \qquad (7)$$
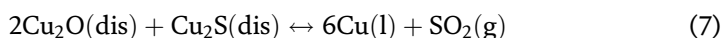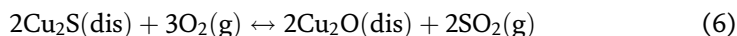
Even when there is 1% of FeS at the end of the first stage [1], it is impossible to avoid the formation of magnetite due to the high oxidizing potential inside of the converter and the inefficiency of the reaction indicated in Eq. (4) to destroy the magnetite. For that reason, the excess of magnetite crystals (with high melting point) produces a viscous slag that involves the pass of significant quantities of copper oxide to the slag (15% Cu). This way, converter slag must be recycled.

The conversion stage is used, apart from to eliminate sulfur and iron, to refine the content in metallic elements. Nobler metals as nickel and cobalt remain in the blister

copper. On the contrary, the slag enriches in zinc, although part volatilizes during the process. As, Sb and part of the Sn, Pb, and Bi can be found in the particulate matter collected before the chimneys (the rest remains in the slag, and only very small quantities in the metal, mainly the bismuth). Finally, blister copper contains 1% S, 0.5–0.6% O and traces of the above-mentioned metals. The conversion process is highly exothermic, making the process autogenous, which allows the charge in the converter of scraps, cemented copper or even concentrates to control the temperature of the process. Therefore, recent investigations in this line are focused on the application of mathematical modeling to minimize copper losses [14] and to increase the energy efficiency of the process [15].

3.6 Flash smelting to produce copper

We have already pointed out that one of the objectives in the copper industry has been to obtain blister copper in a single step. The process required to use air highly enriched with oxygen, which resulted in installations with low capacity of operation because of the rapid deterioration of the tuyeres. Different technologies were proposed in this line, as the Noranda process as it was already pointed out, or the Mitsubishi, which is not based in a single step, among others. Mitsubishi process consists of three interconnected furnaces (smelting furnace to produce the matte, furnace to recover copper from slags and converter furnace) and is installed at least in Birla Copper (Dahej) in India according to the ICSG Directory of Copper Mines and Plants. Further information about the Mitsubishi process can be found in Ref. [16].

3.7 Copper hydrometallurgy

This route of production of primary copper accounts for approximately 15% of the total world production. This route is particularly useful for low-grade ores or low-grade sulfide residues. This is because oxide ores are very limited worldwide. The copper hydrometallurgy is very extensive. Here we present a summary of the most common techniques (further details about copper hydrometallurgy can be found in the reference [17]). Lixiviation can be applied: in situ to low-grade ores, in spoil tips for piled-up material, in boxes by percolation for fine-grained material, or in stirred reactor with or without pressure or temperature for fine-grained material. As leaching agents, it is usual to employ diluted sulfuric acid (for copper oxide ores, carbonates, basic sulfates, and silicates), iron (III) salts solutions prepared or formed *in situ* in presence of oxygen during the lixiviation process from iron (III) sulfate (these solutions, the same as chlorides, are oxidizing and are adequate for copper sulfides), chloride solutions with an oxidizing agent (which are adequate for copper sulfides) and ammonia solutions with ammonia salts, as the ammonium carbonate, for oxidized ores as well as for native copper in presence of carbonate gangue. Rich solutions obtained in the lixiviation process are filtered and sometimes purified to remove polluting dissolved elements. Finally, copper is obtained by cementation, electrolysis, or precipitation of compounds. Cemented copper is melted and fire-refined and subjected to electrowinning. The electrodeposit is sold or melted in ingots because it has its own market (99.9% Cu), or it is subjected to electrowinning. The application of hydrometallurgy in the recovery of wastes is gaining interest, particularly to treat waste that is generated in large quantities in the copper pyrometallurgy as the copper slag. Within this context, Mussapyrova and colleagues [18] reported the copper

selective leaching from mechanically activated copper smelter slag with copper recovery of 87.3% and maximum copper selectivity of 97.9%.

3.8 Fire refining and electrowinning

The refining traditionally involves two stages: fire refining and electrowinning. The product obtained at the end of the first stage usually has 99.9% Cu, which can be insufficient for most applications and electrowinning is required to achieve a purity of 99.995% [1], required for electrical applications. It is possible to obtain a purity of 99.9999% Cu by repeated electrowinning processes or zone melting. This quality is used in research or electronics.

Fire refining (applied in the case of blister copper or in the products of the hydrometallurgical route) consists in eliminating the sulfur (to thousandths of percentage point) and reducing the oxygen content below 0.1%, by reduction, until having a free flat surface of metal resulted from the compensation of the volume of the pores by release of water vapor and gases retained in the metal. The equilibrium sulfur-oxygen in the blister copper can be expressed as follows:

$$S(dis; metal) + 2O(dis; metal) \leftrightarrow SO_2(g) \tag{8}$$
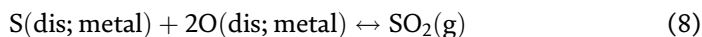
with an equilibrium constant of:

$$k_{eq(Eq.8)} = \frac{[SO_2]}{[O]^2 \cdot [S]} \tag{9}$$

The value of this constant between 1200 and 1300°C is 25, which for a pressure of SO_2 of 0.1 atm gives $[O]^2 \cdot [S] = \mathbf{4 \cdot 10^{-3}}$. This implies that for a sulfur content of 0.02%, the oxygen content would be around 0.5%, and in the case of 2 ppm of sulfur, copper would admit oxygen content above 1%. However, the part of the copper oxidizes to copper (I) oxide during the blowing stage, being dissolved in the metal, and this phase is a selective oxidizing agent as it is expressed in the following equation:

$$S(dis; metal) + 2\,Cu_2O(s) \leftrightarrow 4Cu(l) + SO_2(g) \tag{10}$$
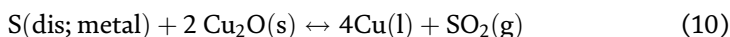
Figure 3.
Copper anodes for the electrowinning process (source: Wikicommons).

The fire refining process is carried out in modern cylindrical furnaces (and sometimes in reverberatory furnaces) and at the end of the process high copper content slags are obtained, which are recycled, and the metal with very low sulfur and oxygen content, which is casted in anodes for the electrowinning process (**Figure 3**).

More than 80% of the world's copper production is refined by electrowinning, which yields high electrical conductivity copper and the separation of the impurities (the precious metals can be recovered at this stage). The process is carried out in cells with 50 g/l of copper in sulfuric medium at temperatures of around 60°C [1]. Periodic purges of the electrolyte are required to eliminate the metals that could compete with the copper in the electrolysis process (As, Sb, Bi, Ni, Co, and Fe). Nobler metals than the copper end in the anodic lodes. The contamination with silver is controlled with small additions of chloride. Sulfur, selenium, and tellurium fall to the anodic lodes, the same as the lead and tin because of not being soluble in sulfate medium. The purification of the electrolyte is carried out by crystallization of the copper pentahydrate sulfate salt and posterior precipitation of the metals by pH control or by means of additives (it is also possible to precipitate the competing metals in an impure cathode that is later recycled in previous stages). The copper cathodes have a purity of >99.99% Cu, which is the electric quality as we will describe later. Anodic slime represents a quantity <1% in weight but they contain precious metals, so they are periodically collected from the bottom of the cells. They are later filtered and dried and subjected to treatments to recover the valuable metals: initial treatments allow to solubilize the copper, later selenium and tellurium are recovered and precious metals finally are melted in an alloy that is known as bullion or doré. Further details about the anode slime are available in Ref. [19].

3.9 Copper foundry

Copper cathodes can be sold as produced but it is quite common to melt the metal to obtain semifinished products. This way, cathodes are melted in furnaces where the metal is cleaned, and alloying elements are added to finally cast the metal. There are different processes of casting: semicontinuous casting, continuous casting, or casting in ingot molds. Different types of furnaces are used for this purpose, but combustibles must be free of sulfur to avoid the contamination of the copper with this element [1], with a maximum of 10 ppm of sulfur because greater contents have a noticeable influence in the mechanical properties of the copper. Semifinished copper products include wires, strips, and rods, among others, and for some specific applications, copper powders are gaining interest. Powders are manufactured from aqueous solutions by cementation or precipitation with hydrogen at high pressure, or also by atomization or by electrolytic method. Finally, three different copper qualities are defined [20]: Refined copper or electrically refined cathode (Electrolytic-tough Pitch Copper, ETP): 99.99% Cu with $0.03 \pm 0.01\%$ Cu_2O, which can be easily worked and has high electrical conductivity (100% IACS) but poor weldability (80% of the world copper production is from this quality).

- Phosphorus deoxidized copper: almost free of oxygen and is produced by the addition of reductant reagents. It can be welded. The electrical resistivity can be increased due to the presence of phosphorus, being this copper (0.04% P) used in applications where electrical conductivity is not required.

- Copper free of oxygen (Oxygen-free copper [OFC], or oxygen-free high thermal conductivity [OFHC]): obtained whether molten copper is kept under an inert or reductant atmosphere. This allows an oxygen content <0.001%. It is used in electronics due to the high electrical conductivity.

Finally, there is another quality of copper obtained by electrical recovery: 99.9%, with poor applications, maybe in some alloys. Research in this line is gaining interest in order to minimize the waste. For instance, the recovery of copper from electric cable waste is derived from the automotive industry by corona-electrostatic separation (99.8% Cu) [21] or waste printed circuit boards utilizing recycling of leachate (99.9% in electrowinning) [22].

4. Applications of copper

Copper, and copper phases, has many different applications due to the excellent properties. Here we present a summary of the main traditional uses of copper. In this line, 50% of the copper is employed because of its excellent electrical conductivity, particularly in low-voltage applications (electric machines, including engines or transformers, among others). Another important application of copper is in semiconductor interconnects in integrated circuits [23].

Copper also exhibits high thermal conductivity and, therefore, it is used for vessels and heat exchange tubes. Other of the main applications of copper is in chemistry or feeding industries, as well as in automotive or naval industries due to the corrosion resistance, particularly when it is alloyed as brass (Cu-Zn), bronze (Cu-Sn), and cupronickels (Cu-Ni) or aluminum bronze (Cu-Al).

Copper is also used in the construction industry for conductions and coatings, and also in appliances, ornamental, and coins. It is also applied in antifriction bearings and several parts of powder metallurgy, and also in the manufacture of ammunition. Copper salts, mainly sulfates and oxides of copper, represent 1% of the world's production. Copper sulfate pentahydrate is used in agriculture to avoid fungi in fruit trees and vegetables due to the efficiency and low toxicity. Soluble copper is also added to feed and food, and also other copper compounds are used as insecticides and preservatives. Metallic copper and some of the copper compounds are used as catalyzers in numerous organic reactions, or as pigments for glass, ceramics, or enameling. Certain copper compounds have applications in the petroleum industry.

We mention here some novel potential applications of copper, copper alloys, or copper phases, as, for instance, complex copper alloys for extreme conditions applications (novel CuCrZrFeTiY alloy for fusion reactor [24]) or bulk metallic glasses [25]. It is also gaining interest due to the bactericidal activity against important human pathogens [26].

5. Environmental issues

Regarding environmental issues, the most relevant points to be considered for action are: control of emissions to the atmosphere, and protection of water and disposal of solid residues. We might indicate here the growing importance of obtaining copper from secondary materials or scraps, as it was already mentioned, in order to reduce the volume of residues and the energy consumption (which is smaller

in the case of recycling copper). In this line, apart from the practice carried out in other metallurgical industries with respect to environmental issues, two points have special relevance: SO_2 emissions and copper slags. In the case of SO_2, this is unavoidably formed in the production of copper during the smelting and conversion, but the final application of this gas is the manufacture of sulfuric acid. The production of sulfuric acid implies cleaning and drying the gases of the furnace followed by the catalytic oxidation of SO_2 to SO_3 and the absorption of the resulting SO_3 by the water to generate H_2SO_4 with 98% concentration. This process is autogenous when we start from gases with 4 vol. % of SO_2 or greater content, bigger contents involve specific treatments. Modern plants of double absorption can even recover 99.5% of the SO_2 at the entrance. The manuscript of Alexander and colleagues about the environmental performance of modern copper smelting technologies is an interesting review about the environmental issues in copper metallurgy [27].

Copper slags are a problem in copper metallurgy due to the large quantity that is generated of this by-product: 2.2–3.0 tons slag for every ton of copper produced [28]. The applications of this residue are very limited since the researchers have still not found a massive utilization for this material [29]. Copper slags have been used as abrasives (polishing and cleaning) for metallic structures [30, 31] and mainly in the building industry: concrete manufactured with copper slag [32]; copper slags as fine particles in concrete manufacturing [33]; copper slag as a replacement for the sand in cement [34]; copper slag as a filler in glass–epoxy composites [35]; and copper slag as a construction material in bituminous pavements [36]. However, due to the high iron and copper contents (>40 wt. % and 1–2 wt. %, respectively), copper slags could become a secondary source for metal recovery [37, 38]. A total of 20 Mt. of primary copper is produced worldwide, and this involves 45 Mt. of slag generated in the process (2.2–3 tons of slag/ton copper [28]), which would represent >20 Mt. Fe and 0.5–1 Mt. Cu yearly sent to controlled landfills. Therefore, copper slag represents an environmental impact [39]: risks of heavy metals lixiviation, a visual impact, and sometimes occupation of cultivable areas. Moreover, research has also focused on the recovery of iron from the slag due to the high iron content in the copper slags: by using coke as a reductant of the copper oxide and the magnetite [40]; by modifying the molten slag with the purpose of promoting the mineralization of recoverable mineral phases and inducing the growth of the mineral phases [41]; by using a method based on coal, Direct Reduction Iron (DRI), and magnetic separation [42]; by means of a process based on aluminothermic reduction [43]; by reduction in an electric furnace with the objective of obtaining a Cu-Pb-Fe alloy [44]; by carbothermal reduction to transform the copper slag into pig iron and glassy material [45]; by irradiation with a microwave as a support of the carbothermal method [46]; or by reduction with coke powders and magnetic separation [47]. In the following section, we present a study about the application of concentrated solar energy to recover valuable metals from copper slags.

6. Case study: Application of concentrated solar energy to the treatment of copper metallurgy slags

6.1 Introduction

The term solar energy is often associated with the generation of heat or electric power. Nevertheless, solar energy, when it is adequately concentrated offers

enormous possibilities in the field of materials science and metallurgy, including the recycling of residues from these industries, because of the high temperatures that can be reached by using this technology (up to 3500 K [48]). In this context, solar energy has been used in metallurgy and materials science for centuries [48]. The legend tells that Archimedes destroyed the Roman army during the Syracuse Siege using mirrors (213–212 BC), although the most traditional application of solar energy in the field of materials was the drying of adobe bricks for the construction of houses. More technical applications appeared during the early Modern period (17th century), when a German mathematician, Ehrenfried Walter Von Tschirnhaus, designed, constructed, and worked with lenses and mirrors to concentrate solar energy [48] and melted iron and obtained ceramics (porcelain). Other researchers worked with concentrated solar energy during the Modern period as Cassini (seventeenth century), who designed a lens with 1 meter in diameter to reach temperatures of around 1000°C and melted iron and silver, or Lavoisier (eighteenth century), who melted iron and approached the melting point of platinum, and also treated metals under special atmosphere such as nitrogen [48]. Anyway, it was after World War II when the investigation in the field of solar energy applications definitely emerged with the construction of the first solar furnace in Mont-Louis (France) in 1949, which was the precursor of the Odeillo solar furnace (Font-Romeu-Odeillo-Via, France; construction from 1962 to 1968; start of operations in 1969, **Figure 4**) under the figure of Felix Trombe, who demonstrated how to employ solar energy to melt high melting point refractory ceramics (alumina, chromium oxide, zirconia, hafnia, and thoria) [48]. Nowadays, there are several installations where it is possible to research within this topic: PSA-CIEMAT (Plataforma Solar de Almería, Centro de Investigaciones Energéticas, Medioambientales y Tecnológicas, in Spain), PROMES-CNRS (Procédés, Matériaux et Énergie Solaire, Centre National de la Recherche Scientifique, in France), Solar Laboratory at the Paul Scherrer Institute (in Switzerland), Weizmann Institute of Science (in Israel), or National Solar Thermal Test Facility and National Renewable Energy Laboratory (in USA), among others, which have made significant contributions to the development of solar-based metallurgical processes. From these original researchers of Von Tschirnhaus, many other researchers have made significant contributions to the progress in the field of concentrated solar energy applications in the field of metallurgy and materials science. These researchers can be read in the extended review published in 2018 in the journal *Solar Energy* with the title *Concentrated solar energy applications in materials science* by Fernández-González and collaborators [48].

Figure 4.
Odeillo solar furnace (font-Roméu-Odeillo-via, France).

Focusing on our research group, the investigation has focused on the: synthesis of calcium aluminates [49], iron metallurgy [50, 51], the treatment of Basic Oxygen Furnace (BOF) slag [52], the production of silicomanganese [53], and transformations in the Ca-Si-O system [54]. The objective of the present Case Study is to present an application of concentrated solar energy in the copper metallurgy: potential recovery of copper and iron from copper slag using solar energy as heat supply for the process.

6.2 Materials and methods

As raw material for experiments, original copper slag from the cleaning furnace was used. It consisted of (wt. %): Fe, 42.82; O, 36.15; Si, 10.36; Al, 3.24; Cu, 1.84; Ca, 1.76; Na, 0.99; S, 0.52; others, 2.32, determined by X-ray fluorescence. X-ray diffraction technique was employed to determine the form in which the crystalline phases of the above indicated elements were: fayalite (Fe_2SiO_4), $85.80 \pm 1.30\%$ in the quantitative analysis; other important crystalline phases were magnetite (Fe_3O_4) and copper–iron oxide (cuprospinel, $CuFe_2O_4$, with Cu^{2+} and Fe^{3+}), $7.90 \pm 1.60\%$ and $6.20 \pm 1.80\%$, respectively, in the quantitative analysis [37].

Tests were performed in a vertical axis 1.5 kW solar furnace located in Font Romeu-Odeillo-Via. The functioning of the solar furnace consists of making solar radiation converge on a small surface (12–15 mm in diameter), called the focal point (where the experimental device is located), using a parabolic concentrator (2.0 m in diameter) and a heliostat that directs sun radiation to the parabolic concentrator. A scheme of the process is represented in **Figure 5**. Several experiments were carried out. They lasted between 15 and 30 minutes, with values of power from 563 to 1409 W.
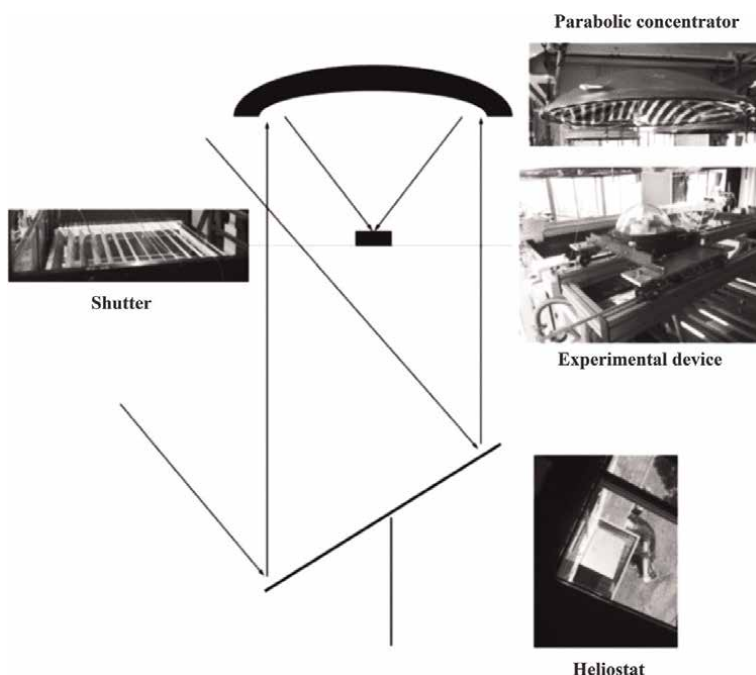
Figure 5.
Scheme of the equipment used for the experiments [37].

6.3 Results and discussion

From visual macroscopic analyses of the samples, it was possible to check that the sample became magnetic after the treatment of the slag with concentrated solar energy. Moreover, occluded matte (copper sulfides) decomposed at the temperatures of the treatment as it is deduced from the investigation carried out by Winkel (metallic copper, iron sulfide, and elemental sulfur can be obtained after the treatment of copper concentrates at a high temperature under an inert atmosphere) [55]. This was corroborated by the fact that there was sulfur in the opposite face to the solar beam, which was the result of the decomposition, according to the above indicated mechanism, of the occluded matte under an ambient in this zone characterized by the low oxygen content.

Samples were subjected to Scanning Electron Microscope (SEM) observations, which confirmed the partial transformation of the copper (as sulfides or oxide) into rich nodules of copper (60–85 wt. % Cu), and also the partial transformation of the fayalite ($FeSiO_4$) into magnetite (iron spinel). SEM images can be observed in **Figure 6**.

The average composition of the copper nodules (as those in **Figure 6**) was 65–85 wt. % Cu; 5–10 wt. % Fe; 2–10 wt. % O; <3 wt. % S, while the size was between 5 and 10 μm, although nodules with a larger size were detected in some samples (between 20 and 35 μm).

Samples were subjected to crushing and grinding down to 40 μm. Then, they were separated into two fractions: magnetic and non-magnetic. The ratio of magnetic to non-magnetic was >80 (average value: 83.3625, in weight). Each fraction was analyzed by X-ray diffraction and X-ray fluorescence. The copper concentrated in the non-magnetic phase 3–6.5 times with respect to the initial slag (1.84 wt. % Cu), non-magnetic fraction contained >7 wt. % Cu. The grade in mining is an important factor about how much a deposit is worth, as it was mentioned at the beginning of this manuscript. The average grade of copper ores in the 21st century is below 0.6% Cu for outside mining operations. This would mean that copper slags might become a potential secondary source of copper, particularly if copper could be concentrated using solar energy. Further information can be read in *Recovery of Copper and Magnetite from Copper Slag Using Concentrated Solar Power (CSP)* [37].
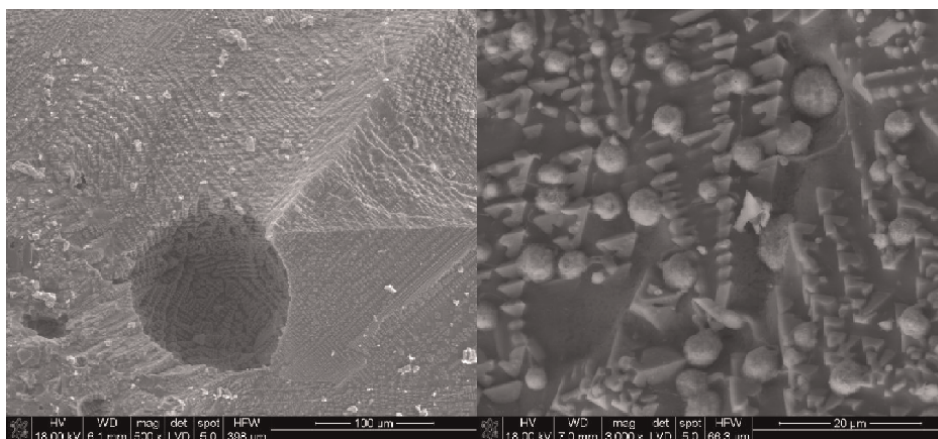
Figure 6.
SEM images of the copper slag treated with concentrated solar energy.

7. Conclusions

This chapter includes a brief review of all the processes used in copper production. The document begins with the introduction of the properties of copper as well as the correlation of the applications with the properties, where it is important to mention the application of copper in electrical and mechanical applications due to its excellent values of thermal and electrical conductivities. The chapter continues with a brief description of the main copper ores, the copper sulfides, which define the subsequent processes that are employed to obtain the metal. The main copper producers are highlighted later. Here it is possible to see the importance of porphyry copper deposits in Latin American countries (as Chile and Peru). However, refined copper is mainly produced in China, Chile, and Japan. Regarding the price of copper, it has significantly increased since the end of the COVID-19 restrictions and has reached the maximum just after the Russian invasion of Ukraine, although this situation could be transitory and copper prices for projects should be based on a long period not in a short period, combined other variables as the proven reserves or the copper grade in the deposit. The process of copper production, including all existing technologies, is described later, from the principles of the matte production to the different qualities of copper that are obtained at the end of the process. The manuscript concludes with a case study about the utilization of concentrated solar energy to treat copper slags in attempts to recover copper and iron from these slags. This document should be seen as an overview of the copper production process.

Author details

Daniel Fernández-González[1*] and Luis Felipe Verdeja González[2]

1 Center for Research in Nanomaterials and Nanotechnology-Spanish National Research Council (CINN-CSIC), El Entrego, Asturias, Spain

2 University of Oviedo, Oviedo-Uviéu, Asturias, Spain

*Address all correspondence to: d.fernandez@cinn.es

IntechOpen

References

[1] Sancho J, Verdeja LF, Ballester A. Metalurgia Extractiva. Volumen II: Procesos de Obtención. 1st ed. Madrid: Ed. Síntesis; 2000. 428 p

[2] Velásquez-Yévenes L, Lasnibat R. Simultaneous recovery of copper and manganese from exotic copper ore in acid chloride media using cane molasses as the reducing agent. Hydrometallurgy. 2021;**199**:105531. DOI: 10.1016/j.hydromet.2020.105531

[3] Godirilwe LL, Magwaneng RS, Sagami R, Haga K, Batnasan A, Aoki S, et al. Extraction of copper from complex carbonaceous sulfide ore by direct high-pressure leaching. Minerals Engineering. 2021;**173**:107181. DOI: 10.1016/j.mineng.2021.107181

[4] Corin KC, Kalichini M, O'Connor CT, Simukanga S. The recovery of oxide copper minerals from a complex copper ore by sulphidisation. Minerals Engineering. 2017;**102**:15-17. DOI: 10.1016/j.mineng.2016.11.011

[5] Liu W, Tang M, Tang C, He J, Yang S, Yang J. Dissolution kinetics of low-grade complex copper ore in ammonia-ammonium chloride solution. Transactions of Nonferrous Metals Society of China. 2010;**20**:910-917. DOI: 10.1016/S1003-6326(09)60235-1

[6] Hu K, Wu A, Wang H, Wang S. A new heterotrophic strain for bioleaching of low-grade complex copper ore. Minerals. 2016;**6**:12. DOI: 10.3390/min6010012

[7] Morris L. Sustainability in mining. Mining a better world. Materials World. 2020;**28**:31-33

[8] Crowson P. Minerals Handbook 1996-97. In: Statistic, Analysis of the World Minerals Industry. New York: Stockton Press; 1996. pp. 108-120

[9] Binded A. Metal madness. Materials World. 2022;**30**:5-8

[10] Oraee K, Sayadi AR, Tavassoli SMM. Economic evaluation and sensitivity-risk analysis of Zarshuran gold mine project. In: SME Annual Meeting, Feb 27-Mar 02, 2011. Colorado, USA: Society for Mining, Metallurgy & Exploration; 2011

[11] ESFC Investment Group. Mine construction cost: How much does it cost to build a mine or quarry?. Available from: https://esfccompany.com/en/articles/construction/mine-construction-cost-how-much-does-it-cost-to-build-a-mine-or-quarry/ [Accessed: October 11, 2023]

[12] Schlesinger ME, King MJ, Sole KC, Davenport WG. Extractive Metallurgy of Copper. 5th ed. Oxford: Elsevier; 2011. pp. 252-256

[13] Pero-Sanz JA, Fernández-González D, Verdeja LF. Structural Materials: Properties and Selection. 1st ed. Cham: Springer International Publishing; 2019. DOI: 10.1007/978-3-030-26161-0

[14] Ahmed H, Ricardez-Sandoval L, Vilkko M. Optimal scheduling of the Peirce-smith converter in the copper smelting process. PRO. 2021;**9**:2004. DOI: 10.3390/pr9112004

[15] Pineda JA, Plascencia G. Exergy in copper converting and its relation to SO_2 emissions. Journal of Sustainable Metallurgy. 2016;**2**:265-272. DOI: 10.1007/s40831-016-0058-4

[16] Shibasaki T, Hayashi M. Top-blown injection smelting and converting: The

Mitsubishi process. JOM. 1991;**43**:20-26. DOI: 10.1007/BF03222230

[17] Rumbu R. Review on Copper Hydrometallurgy: Roasting-Leaching-SX-Electrowinning. 1st ed. Morrisville, North Carolina: Lulu Press, Inc.; 2018. 362 p

[18] Mussapyrova L, Nadirov R, Balaz P, Rajnak M, Bures R, Balaz M. Selective room-temperature leaching of copper from mechanically activated copper smelter slag. Journal of Materials Research and Technology. 2021;**12**: 2011-2025. DOI: 10.1016/j. jmrt.2021.03.090

[19] Hait J, Jana RK, Sanyal SK. Processing of copper electrorefining anode slime: A review. Mineral Processing and Extractive Metallurgy, Transactions of the Institutions of Mining and Metallurgy: Section C. 2009; **118**:240-252. DOI: 10.1179/ 174328509X431463

[20] Pero-Sanz JA, Quintana MJ, Verdeja LF. Solidification and Solid-State Transformations of Metals and Alloys. 1st ed. Boston: Elsevier; 2017

[21] Catinean A, Dascalescu L, Lungu M, Dumitra LM, Samuila A. Improving the recovery of copper from electric cable waste derived from automotive industry by corona-electrostatic separation. Particulate Science and Technology, An International Journal. 2021;**39**: 449-456. DOI: 10.1080/02726351. 2020.1756545

[22] Rajahalme J, Peramaki S, Budhathoki R, Vaisanen A. Effective recovery process of copper from waste printed circuit boards utilizing recycling of leachate. Advances in Process Metallurgy. 2021;**73**:980-987. DOI: 10.1007/s11837-020-04510-z

[23] Cheng Y-L, Lee C-Y, Huang Y-L. Copper metal for semiconductor interconnects. In: Seehra MS, Bristow AD, editors. Noble and Precious Metals. London: IntechOpen; 2018. Chapter 10. pp. 215-250

[24] Li M, Wang H, Guo Y, Wang H, Zheng D, Shan J, et al. Microstructures and mechanical properties of the novel CuCrZrFeTiY alloy for fusion reactor. Journal of Nuclear Materials. 2020;**532**: 152063. DOI: 10.1016/j.jnucmat.2020. 152063

[25] Suárez M, Fernández-González D, Díaz LA, Diologent F, Verdeja LF, Fernández A. Consolidation and mechanical properties of $ZrCu_{39.85}Y_{2.37}Al_{1.8}$ bulk metallic glass obtained from gas-atomized powders by spark plasma sintering. Intermetallics. 2021;**139**:107366. DOI: 10.1016/j. intermet.2021.107366

[26] Montero DA, Arellano C, Pardo M, Vera R, Gálvez R, Cifuentes M, et al. Antimicrobial properties of a novel copper-based composite coating with potential for use in healthcare facilities. Antimicrobial Resistance & Infection Control. 2019;**8**:3. DOI: 10.1186/ s13756-018-0456-4

[27] Alexander C, Johto H, Lindgren M, Pesonen L, Roine A. Comparison of environmental performance of modern copper smelting technologies. Cleaner Environmental Systems. 2021;**3**:100052. DOI: 10.1016/j.cesys.2021.100052

[28] Criado M, Ke X, Provis JL, Bernal SA. 7 - alternative inorganic binders based on alkali-activated metallurgical slags. In: Savastano H, Fiorelli J, dos Santos SF, editors. Sustainable and Nonconventional Construction Materials Using Inorganic Bonded Fiber Composites. London: Woodhead Publishing; 2017. pp. 185-220

[29] Murari K, Siddique R, Jain KK. Use of waste copper slag, a sustainable material. Journal of Material Cycles and Waste Management. 2015;**17**:13-26. DOI: 10.1007/s10163-014-0254-x

[30] Kambham K, Sangameswaran S, Datar SR, Kura B. Copper slag: Optimization of productivity and consumption for cleaner production in dry abrasive blasting. Journal of Cleaner Production. 2007;**15**:465-473. DOI: 10.1016/j.jclepro.2005.11.024

[31] Jiménez-Padilla B. Armado de Tuberías. FMEC0108. 1st ed. IC Editorial: Antequera, Spain; 2014

[32] Coursol P, Cardona N, Mackey P, Bell S, Davis B. Minimization of copper losses in copper smelting slag during electric furnace treatment. JOM. 2012;**64**:1305-1313. DOI: 10.1007/s11837-012-0454-6

[33] Cendoya P. Efecto en la resistencia de las escorias de fundición de cobre como agregado fino en el comportamiento resistente del hormigón. Ingeniare Revista Chilena de Ingeniería. 2009;**17**:85-94. DOI: 10.4067/S0718-33052009000100009

[34] Nazer A, Pavez O, Rojas F. Use of copper slag in cement mortar. REM Revista Escola de Minas. 2012;**65**:87-91. DOI: 10.1590/S0370-44672012000100012

[35] Biswas S, Satapathy A. Use of copper slag in glass-epoxy composites for improved wear resistance. Waste Management & Research Journal for a Sustainable Circular Economy. 2010;**28**:615-625. DOI: 10.1177/0734242X09352260

[36] Pundhir NKS, Kamaraj C, Nanda PK. Use of copper slag as construction material in bituminous pavements. Journal of Scientific & Industrial Research. 2005;**64**:997-1002

[37] Fernández-González D, Prazuch J, Ruiz-Bustinza I, González-Gasca C, Gómez-Rodríguez C, Verdeja LF. Recovery of copper and magnetite from copper slag using concentrated solar power (CSP). Metals. 2021;**11**:1032. DOI: 10.3390/met11071032

[38] Potysz A, Van Hullebusch ED, Kierczak J, Grybos M, Lens PNL, Guibaud G. Copper metallurgy slags – Current knowledge and fate: A review. Critical Reviews in Environmental Science and Technology. 2015;**45**:2424-2488. DOI: 10.1080/10643389.2015.1046769

[39] Nazer A, Pavez O, Rojas F, Aguilar C. Una revisión de los usos de las escorias de cobre. In: Proceedings of the IBEROMET XI. X CONAMET/SAM. Viña del Mar, Chile: SOCHIM/PUC Valparaiso; Nov 2010. pp. 2-5

[40] Busolic D, Parada F, Parra R, Sánchez M, Palacios J, Hino M. Recovery of iron from copper flash smelting slags. Mineral Processing and Extractive Metallurgy. Transactions of the Institutions of Mining and Metallurgy: Section C. 2011;**120**:32-36. DOI: 10.1179/037195510X12772935654945

[41] Guo Z, Zhu D, Pan J, Wu T, Zhang F. Improving beneficiation of copper and iron from copper slag by modifying the molten copper slag. Metals. 2016;**6**:86. DOI: 10.3390/met6040086

[42] Xian-Lin Z, De-Qing Z, Jian P, Teng-Jiao W. Utilization of waste copper slag to produce directly reduced iron for weathering resistant steel. ISIJ International. 2015;**55**:1347-1352. DOI: 10.2355/isijinternational.55.1347

[43] Heo JH, Chung Y, Park JH. Recovery of iron and removal of hazardous elements from waste copper slag via a novel aluminothermic smelting reduction (ASR) process. Journal of Cleaner Production. 2016;**137**:777-787. DOI: 10.1016/j.jclepro.2016.07.154

[44] Siwiec G, Sozanska M, Blacha L, Smalcerz A. Behaviour of iron during reduction of slag obtained from copper flash smelting. Meta. 2015;**54**: 113-115

[45] Sarfo P, Wyss G, Ma G, Das A, Young C. Carbothermal reduction of copper smelter slag for recycling into pig iron and glass. Minerals Engineering. 2017;**107**:8-19. DOI: 10.1016/j.mineng. 2017.02.006

[46] Liao Y, Zhou J, Huang F. Separating and recycling of Fe, Cu, Zn from dumped copper slag by microwave irradiation assisted carbothermic method. Journal of Residuals Science and Technology. 2016;**13**:S155-S160. DOI: 10.12783/issn.1544-8053/13/2/S22

[47] Li K, Ping S, Wang H, Ni W. Recovery of iron from copper slag by deep reduction and magnetic beneficiation. International Journal of Minerals, Metallurgy, and Materials. 2013;**20**:1035-1041. DOI: 10.1007/s12613-013-0831-3

[48] Fernández-González D, Ruiz-Bustinza I, González-Gasca C, Piñuela-Noval J, Mochón-Castaños J, Sancho-Gorostiaga J, et al. Concentrated solar energy applications in materials science and metallurgy. Solar Energy. 2018;**170**: 520-540. DOI: 10.1016/j.solener.2018. 05.065

[49] Fernández-González D, Prazuch J, Ruiz-Bustinza I, González-Gasca C, Piñuela-Noval J, Verdeja LF. Solar synthesis of calcium aluminates. Solar Energy. 2018;**171**:658-666. DOI: 10.1016/j.solener.2018.07.012

[50] Mochón J, Ruiz-Bustinza Í, Vázquez A, Fernández D, Ayala JM, Barbés MF, et al. Transformations in the iron-manganese-oxygen-carbon system resulted from treatment of solar energy with high concentration. Steel Research International. 2014;**85**:1469-1476. DOI: 10.1002/srin.201300377

[51] Fernández-González D, Prazuch J, Ruiz-Bustinza I, González-Gasca C, Piñuela-Noval J, Verdeja LF. Iron metallurgy via concentrated solar energy. Metals-Basel. 2018;**8**:873. DOI: 10.3390/met8110873

[52] Fernández-González D, Prazuch J, Ruiz-Bustinza I, González-Gasca C, Piñuela-Noval J, Verdeja LF. The treatment of basic oxygen furnace (BOF) slag with concentrated solar energy. Solar Energy. 2019;**180**:372-382. DOI: 10.1016/j.solener.2019.01.055

[53] Fernández-González D, Prazuch J, Ruiz-Bustinza I, González-Gasca C, Piñuela-Noval J, Verdeja LF. Transformations in the Mn-O-Si system using concentrated solar energy. Solar Energy. 2019;**184**:148-152. DOI: 10.1016/j.solener.2019.04.004

[54] Fernández-González D, Prazuch J, Ruiz-Bustinza I, González-Gasca C, Piñuela-Noval J, Verdeja LF. Transformations in the Si-O-Ca system: Silicon-calcium via solar energy. Solar Energy. 2019;**181**:414-423. DOI: 10.1016/j.solener.2019.02.026

[55] Winkel HE. Thermal decomposition of copper sulfides under concentrated irradiation [PhD thesis] Swiss Federal Institute of Technology Zurich, Zurich, Switzerland. 2006

Chapter 2

Electroosmotic Drainage Applied to Mining Waste

Leonardo Romero, Manuel Cánovas and Juan Sanchez-Perez

Abstract

One factor affecting the stability of mining stockpiles is the moisture defined mainly by copper solution trapped in the porous by capillary. This moisture is not easy to remove if conventional methods are applied which use pressure or gravity as driving force. In the case of saturated or partially saturated soils with water, containing a large fraction of fine material, electroosmosis not only allows to reduce the humidity but also changes the structure, giving a higher strength and stability to the soils. Since the movement of the water, due to the electric gradient, is from the anode toward the cathode, the soil water content will decrease at the anode and will increase at the cathode. Water accumulated at the cathode then can be discharged by providing a drainage system at the cathode. This chapter presents theoretical and experimental aspects on electroosmotic drainage technique, based in works realized by the authors of this chapter. To explain the water flow through a mining residue containing a certain fraction of fine material and that in addition presents a high humidity, a model for the fluid flow in porous media is described here, taking into consideration two driving forces, defined by hydraulic and electric potentials.

Keywords: electroosmosis, electroosmotic, drainage, electroosmotic flux, driving force

1. Introduction

Mine waste represents one of the critical aspects of mining activity due to the environmental and social impacts that could generated not only in the period of extraction and processing of mineral but also in the post-closure period of the mining activity. Whether extraction and processing are stages that generate large quantities of waste that are stored above ground where they may constitute a potential risk of groundwater contamination or they may present structural stabilization problems by its humidity.

In waste from copper leaching, the remaining humidity is due to the solution trapped in the capillary interstices of the solid matrix. To avoid structural stabilization problems, it is necessary to reduce the moisture of the waste. One possibility is to let the humidity reduce naturally, by letting the water drain gravitationally. The action of this technique is limited, since gravity has no action on capillary trapped water. Thus, to reduce the remaining moisture content of the solid material and accelerate the

drainage process, electroosmotic drainage technique is proposed. Electroosmotic drainage consists of applying a low electric potential to dewater a porous medium, in this case the solid mining waste. This technique was employed in the 50 years to consolidated clay soils as a simple and efficient way to accelerate the dewatering process in soils with low hydraulic conductivity [1, 2]. Since then, electroosmotic drainage has been successfully applied mainly to the drying process of sediments, and remediation of contaminated soils with heavy metals [3–10]. Applications of this technique in mining activities are still under development. In a previous work, through the realization of mining waste drainage experiments, at laboratory and bench scale, the conceptual validation of the technique was demonstrated [7, 10, 11]. Electroosmotic drainage is more efficient than conventional drainage techniques such as vacuum filtering, belt filter pressing and centrifuging in terms of collected solution, time of drained solution, and energy consumption [12]. Water in a porous material can be divided into four types: free water, interstitial or capillary water, surface or vicinal water and intracellular water [13]. While conventional drainage techniques, which are based on mechanical pressure, are effective at removing free water, electroosmotic drainage can be applied to remove free, interstitial, and vicinal water [14].

The establishment of an electric field, in a porous medium with high humidity, in addition to the removing of the capillary trapped water, causes the ionic species present in solution to migrate toward the oppositely charged electrode (anode or cathode), and this ion migration is called electromigration, while the mechanism that govern the movement of the water toward the positively charged electrode (cathode) is called electroosmosis. In this chapter, the theoretical basis, complemented with experimental data at laboratory and bench scale, is established, describing conceptual and mathematically; in addition to the gravitational drainage, the electroosmotic flow as a transport mechanism allows an additional drainage of solution in a process of heap pile copper leaching. The importance of the application of this mechanism is that it allows a larger volume of solution to be drained than that could be drained naturally, in which the gravity is the only driving force acting on the medium. Keeping in mind that with the application of an electric field to the medium, the electroosmotic mechanism acts mainly on that fraction of solution trapped capillary, and this occurs in the fine solid fraction.

2. Flow of fluid in porous media

Flow of water in porous media is a relevant subject in applications such as hydrogeology and in multiple branches of engineering. At large physical scales, Darcy's law is used, which provides a macroscopic description of flow in porous media. At smaller physical scales, flow and transport are simulated using more detailed descriptions such as Hagen-Poiseuille or Navier-Stokes flow. In the past decades, the topic of multiphase flow in porous media has received widespread attention. There are numerous pore-scale simulation and experimental studies on single-phase and multiphase flow and transport in porous media. However, very few studies of flow and transport in charged porous media have been reported [15–17]. When the porous medium and the fluids present in the pore space are exposed to an electric field, a number of electrokinetic and electro-hydrodynamic effects or mechanisms can take place, such as electromigration, electrophoresis, and electroosmosis. These phenomena have been used in applications, such as electrophoretic migration of contaminants in soils [4], microfluidics [18], or enhanced oil recovery [19].

2.1 Conceptualization of the electroosmotic waterflow

Electroosmosis is the flow of water induced by the application of an electric field [20, 21]. This waterflow, named electroosmotic flow, is generated by the electrical interaction between the surface of the solid particles and the fluid, which leads to charge separation at a "double layer" interface. The volumetric flow of water is dependent of the double-layer properties, the chemical composition of the porous material, the type of fluid in the pores, the geometry and size of the pores, the saturated condition of the medium, and the intensity of the applied electric potential [22]. Fluid flow usually occurs in the same direction as the applied electric potential, from anode to cathode [23, 24].

One of the earliest and most widely used theoretical models of the electroosmosis process is based on a model introduced by Helmholtz in 1879 and refined by Smoluchowski in 1914 [25]. Thus, to estimate the electroosmotic flow of water per unit of area (q_{eo}) in a saturated porous media, the Helmholtz-Smoluchowski model (H-S model) is used [22]. This flux of water (q_{eo}), expressed in units of water volume per unit of area and unit of time is formulated as:

$$q_{eo} = -\frac{\varepsilon_p \varepsilon_w \zeta}{\eta} \frac{\Delta\varnothing}{\Delta L} \qquad (1)$$

where ε_p is the soil porosity, ε_w is the electrical permittivity of the soil, ζ is the zeta-potential, η is the dynamic viscosity of the fluid, $\Delta\phi$ is the applied electric voltage difference between electrodes, and ΔL is the separation distances between electrodes.

The direction of the electroosmotic flow, relative to the electric potential, is solely determined by whether the zeta-potential is positive or negative. Most soils and porous ceramics exhibit a negative zeta-potential causing the direction of the electroosmotic flux to be from the anode toward the cathode. As the zeta-potential (ζ) is a parameter dependent of the pH value, the movement of the water may be in one direction, toward the cathode, or toward the anode, [23–25]. The electroosmotic flow can be expressed in terms of the electric gradient and the electroosmotic permeability of the porous media (k_{eo}), which is a measure of the fluid flux per unit area of the porous media. The value of k_{eo} is assumed to be a function of the zeta-potential of the soil-pore fluid interface, the viscosity of the pore fluid, the porosity, and electrical permittivity of the soil:

$$k_{eo} = \frac{\varepsilon_p \varepsilon_w \zeta}{\eta} \qquad (2)$$

The electroosmotic permeability is pH-dependent as the z-potential (ζ) do it. Taken as reference the Kaolinite, an increase of the pH from 0 to 14 makes the electroosmotic permeability increases in the rage of (3 to 8) $\times 10^{-9}$ (m^2/V/s) [26].

2.2 Flux of water for the case of saturated medium

The fluid flux is the consequence of three gradients: hydraulic gradient $\nabla(-h)$ (Darcy's law), electrical gradient $\nabla(-\phi)$, and a chemical gradient. The latter, chemical gradient, is significant only in the presence of large molecular chains and in very active clay deposits. Assuming that the chemical gradient is not significant [27, 28], the porous fluid mass flux (J_w), expressed in mass flow of water per unit of area, is thus estimated by two contributions:

$$J_W = J_h + J_{eo} \tag{3}$$

where J_h, and J_{eo} (kg/m^2/s) are the hydraulic and electroosmotic mass flux of water, respectively. Both fluxes, J_h y J_{eo}, are defined by a driven force times the conductivity coefficient (K) that describes the ease with which a fluid (water) can move through pore spaces. Thus, rewriting the mass flux in terms of the volumetric flux (q) gives:

$$J_W = J_h + J_{eo} = \rho_w(q_h + q_{eo}) = \rho_w[K_h \nabla(-H) + K_{eo} \nabla(-\varnothing)] \tag{4}$$

where ρ_w (kg/m^3) is water density, q_h and q_{eo} (m^3/m^2/s) are hydraulic and electroosmotic flow velocity, respectively, H is hydraulic head (m), and ϕ is the applied electric potential (V). The K_h (m/s) and K_{eo} (m^2/V/s) are the hydraulic and electroosmotic conductivity, respectively. The negative sign indicates that flow of water occurs from large to small hydraulic head, for the hydraulic flow, and from anode to cathode, opposite to the electric gradient, for the electroosmotic flow. The hydraulic head, H, in length units, at any point in the soil is defined as the summa of the elevation head, z, and the pressure head (Ψ):

$$H = \frac{p_c}{\rho_w g} + z = \Psi + z \tag{5}$$

where p_c is the pore water pressure, ρ_w is the density of the fluid (solution), and g is the gravitational acceleration. Then, the equation for the mass flux, Eq. (4), may be rewritten as:

$$J_W = J_h + J_{eo} = \rho_w(q_h + q_{eo}) = -\rho_w[K_h \nabla(\Psi + z) + K_{eo} \nabla(\varnothing)] \tag{6}$$

The relative importance of the hydraulic and electroosmotic contributions, to the flow of water, is determined by the ratio of the electroosmotic to the hydraulic conductivity, expressed as K_{eo}/K_h. This ratio is affected by the soil type, microstructure, and pore fluid conditions. In coarse-grained soil, the ratio is very low, due to the almost nonexistent electroosmotic flow and relatively high hydraulic conductivity ($>10^{-3}$ cm/s) of such soils. In soft, fine-grained soils, the ratio is significant as K_{eo} is usually on the order of 10^{-5} cm^{2}V^{-1}s^{-1}, while K_h varies between 10^{-5} cm/s for fine sand and 10^{-9} cm/s for bentonite [27–29]. Therefore, for moving liquid through fine-grained soils, the electrical gradient is more effective than the hydraulic gradient.

The hydraulic conductivity value (K_h) is always positive, and therefore, the hydraulic gradient always determines the direction of the hydraulic flow. In contrast, the K_{eo} can be either positive or negative resulting in flow with or against the electric potential. On the other hand, the magnitude of the K_h is dependent of the pore size distribution. However, K_{eo} is independent of pore size (**Figure 1**). In low-permeability zones such as clay, particle size smaller than 0.002 mm in diameter, the electroosmotic flow is easier to achieve than hydraulic flow (pressure-driven) (see **Figure 1**).

When water is trapped between fine solid particles, the electroosmotic technique is more efficient than the technique driven by pressure [29], because electroosmotic flow is based on the surface and colloidal characteristics of particles in suspension and is independent of pore size, unlike conventional hydraulic flow, which falls off significantly with pore size [30]. For copper mining waste, as a reference, tailing material from mineral processing, finely ground waste with particle size range 0.06–0.002 mm (similar to fine
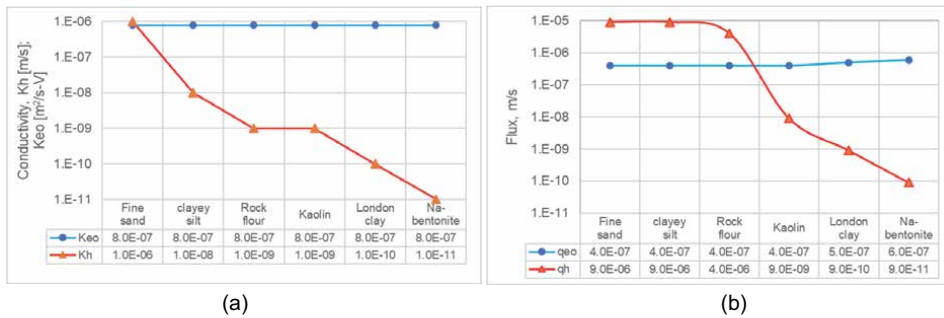
Figure 1.
a) Electro osmotic (K_{eo}) and hydraulic (K_h) conductivity for selected sediments; b) Comparison of hydraulic (q_h) and electro osmotic (q_{eo}) flow rates [24].

sand/coarse silt), the hydraulic conductivity is 1.65×10^{-7} m/s [31]. Since pressure dewatering is a popular technique to reduce the water content of solid waste, some works have combined electroosmotic drainage and pressure dewatering [32, 33].

3. Humidity and fraction of fine material on the drained solution

The total fluid flowing in a porous material under the effects of an electrical potential and the gravitational force is mainly caused by two gradients: the hydraulic gradient (Darcy's law) and the electrical gradient (electroosmosis). The contributions of each of the gradients are affected by soil type, soil microstructure, and pore fluid conditions [28]. For example, in coarse-grained soils, the ratio of electroosmotic to hydraulic flow is very low, and it means that the electroosmotic flow is almost nonexistent, while in fine-grained soils the ratio is high [34]. Therefore, a large electrical gradient is more effective than a hydraulic gradient for moving liquid through fine-grained soils.

Experimental tests have been carried out, at laboratory scale, to evaluate the effect of the initial moisture degree and the fraction of fine material contained in the mining residues, over the volume of solution drained out from the electroosmotic cell containing the residues [35]. All the tests were done in 20-liter electroosmotic cells as shown in **Figure 2**, using a linear configuration of stainless steel electrodes, 24 V of constant applied voltage between electrodes, and an operating time of 48 hours. The tests followed a 3^2 factorial design experiment with and without replication,

Figure 2.
(a) electroosmotic drainage cell; and (b) gravitational drainage cell [35].

Material	10% fine particle		15% fine particle		20% fine particle	
	Weight (kg)	**%**	**Weight (kg)**	**%**	**Weight (kg)**	**%**
Gravel	0.28	4	0.2	3	0.13	2
Gross sand	1.86	27	1.65	25	1.46	23
Fine sand	4.07	59	3.77	57	3.49	55
Clay	0.69	10	0.99	15	1.27	20

Table 1.
Distribution of the particle size fraction of the solid matrix [35].

considering two factors with three levels each. The factors were the fraction of fine material and the moisture of the sample, and the levels of them were 10, 15, and 20% for fine material and 10, 20, and 30% for the moisture. The volume of drained solution was defined as the response variable.

The solid matrix is made up of two materials: coarse material made up of solid particles of different granulometric sizes (gravel, coarse, and fine sand) and fine material made up of clay material (**Table 1**).

The highest percentage of fine material (FP) was that established by slope safety regulations, while the other two were chosen to study the influence of lower levels of fine material content. The initial moisture (IM) levels of 10, 20, and 30% were defined based on mining applications. The first value of 10% is typical in leaching residues, while 30% is the typical level in tailings.

Two series of experimental test were run, differencing them only in the applying of an electrical field. In both tests act the gravity as one of the forces responsible of the volume of solution drained. In the first one test (**Figure 2a**), a voltage of 24 [V] between stainless electrodes was applied, following a lineal configuration of electrodes with a separation distance of 20 cm. In the other one test (**Figure 2b**), no voltage was applied, acting only the gravity as the force responsible of the drained volume of solution.

Test	% Fine particles (FP)	Initial Moisture	% Final moisture (FM)		Contribution[*]
		%, (IM)	**FM_{GD}**	**$FM_{G\&EOD}$**	**C_{EOD}, (%)**
1	10	10	10	10	0
2	10	20	17.53	18.01	3.15
3	10	30	18.27	19.49	6.26
4	15	10	10	10	0
5	15	20	16.65	18.03	7.65
6	15	30	16.81	21.1	20.33
7	20	10	10	10	0
8	20	20	15.89	18.11	12.26
9	20	30	14.8	21.2	30.19

[*]C_{EOD}: contribution of EOD to final moisture, $C_{EOD} = (FM_{G\&EOD} - FM_{GD})/FM_{G\&EOD}$

Table 2.
Data series collected from carried out run with electroosmotic and gravitational drainage, following a 3^2-factorial design [35].

% Initial moisture	% Fine particles		
	A1	**A2**	**A3**
B1	0	0	0
B1-replica	0	0	0
B2	12.33	16.76	20.54
B2-replica	11.80	16.95	19.98
B3	39.11	43.96	50.67
B3-replica	36.37	41.20	50.01

Table 3.
Data series collected from carried-out tests run with electroosmotic and gravitational drainage, following a 3^2 factorial design with replica [35].

Source of variation	Sum of square	Degrees of freedom	Quadratic mean	F-ratio	p-Value
A: % Fine material	4.35202	1	4.35202	311.83	0.0001
B: % Initial moisture	65.8691	1	65.8691	4719.68	0.0000
AB	3.01022	1	3.01022	215.69	0.0001
BB	22.8038	1	22.8038	1633.95	0.0000
Residual	0.055825	4	0.0139562		
Total	96.0909	8			
R^2	99.9419%				

Table 4.
*ANOVA, using the data series as shown in **Table 2** and the software Statgraphics, for the experimental run applying electrical field [35].*

An operating time of 48 hours was determined for each of the tests carried out, whose results are summarized in **Tables 2** and **3**.

For the data series in **Table 2**, an ANOVA was applied based on the proposed 3^2 factorial design test to identify the influence of the relevant factors and their interaction (**Table 4**). Subsequently, a nonlinear regression was applied to obtain a mathematical model.

The analysis of variance for the quadratic model, with a confidence interval of 95%, showed that four p-values are less than 0.05 (see **Table 4**), which means that the null hypothesis (zero contribution to the final moisture) is rejected by the four effects (A, B, AB, and BB), while the effect AA on the final moisture is not significant. The resulting statistic model is formulated by Eq. (7) and is graphically shown in **Figure 3**:

$$Final\ Moisture\ (\%) = -6.093 + 0.177(A) + 1.942(B) - 0.017(A*B) - 0.034(B)^2 \tag{7}$$

If the contribution of electroosmotic drainage on the final moisture level is analyzed, the analysis of variance for the quadratic model, with a confidence of 95%, showed that the three p-values are less than 0.05, which means that three null hypothesis is rejected for the effects A, B, and AB. The effects AA and BB did not significantly affect the final moisture level. The model describing the contribution of electroosmotic drainage, C_{eod}, to the final moisture is:

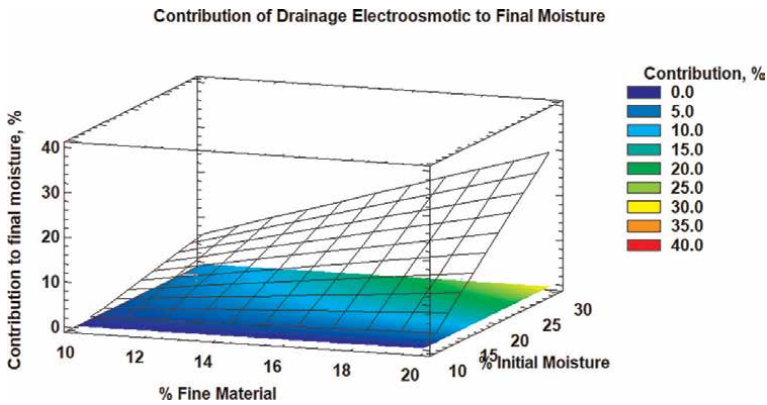**Final moisture distribution by applying Electroosmotic Drainage**
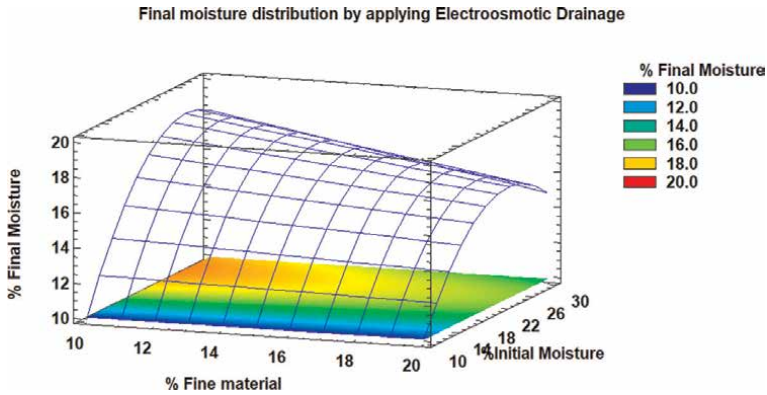
Figure 3.
Final moisture affected by the % of fine material and the % of initial moisture when an electric potential is applied [35].

Contribution of Drainage Electroosmotic to Final Moisture

Figure 4.
Contribution of the electroosmotic drainage technique on final moisture [35].

$$C_{eod} = 9.55 - 0.47(A) - 1.56(B) + 0.12(A \times B) \qquad (8)$$

Figure 4 represents the contribution of electroosmotic drainage on the final moisture level of the sample. The results show that the higher the initial moisture, the greater the reduction of moisture when an electric field is induced. As can be seen, the tests with natural drainage were less efficient. This electroosmotic contribution is greater as the % fine particles of the solid matrix increases.

3.1 Model describing the volume of drained solution from the solid matrix

A 3^2 factorial design test with replication was used to determine the effect of the factors (fraction of fine particles (FP) = B and initial moisture (IM) = A, notation in **Table 2**), and their interaction against the drained volume as response variable. **Table 3** summarizes data series collected from the carried-out tests.

According to the realized ANOVA, four p-values were less than 0.05, which means that the null hypothesis (zero contribution to the final moisture) is rejected for the effects A, B, AB, and BB on the drained volume, while the effect AA results to be not Significative (see **Table 4**). The equation representing the electroosmotic model is:
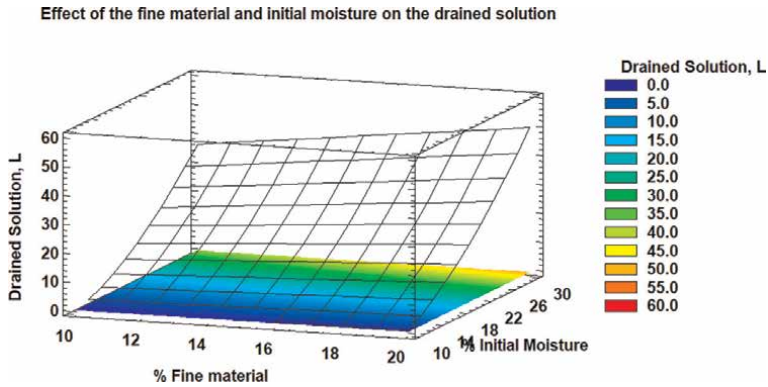
Figure 5.
Representation of the model for the volume of drained solution from the sample by applying the electroosmotic technique [35].

$$V_{drained} = 2.876 - 0.567(A) - 0.921(B) + 0.063(AB) + 0.054(B)^2 \qquad (9)$$

where $V_{drained}$ is the drained volume of the solution in cubic centimeter. **Figure 5** graphically represents the electroosmotic drainage model.

3.2 Comparison in the drained solution by the two techniques

The dewatering experimental tests realized to compare the electroosmotic technique with the conventional technique (gravitational dewatering) were done in the 20-liter electroosmotic cells at laboratory scale as those shown in **Figure 2**. The results plotted in **Figure 6** shows that the volume of collected solution using the electroosmotic technique may reach three times more than the collected by the gravitational technique (0.32 over
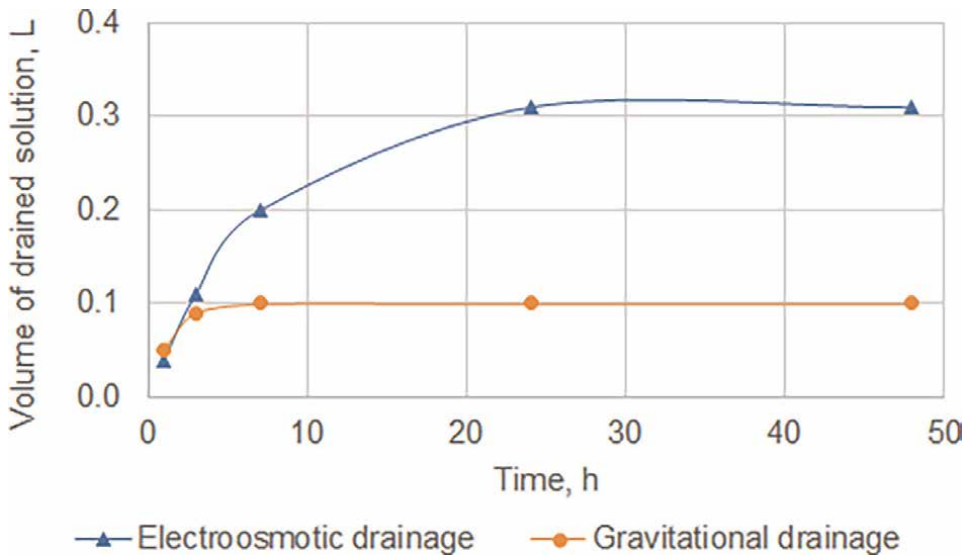
Figure 6.
Solution collected by electroosmotic and gravitational drainage technique in cells containing 7 kg of dried material with an induced humidity of 15% [35].

0.1 L, respectively). This difference of 0.22 L may be explained for the high fraction of fine particles contained in the sample material. The capacity of drained solution, defined as the volume of collected solution per mass of sample material, is estimated in 0.046 L/kg, value that varies depending of the fine solid fraction which is directly related to the high volume of water trapped by capillary. Thus, the larger the fraction of fine material in the mining waste, the larger the volume of drained solution by electroosmotic flow.

4. Flux of water for the case of unsaturated medium

For the case of a saturated medium, the conductivity (K), associated to the fluid properties, density and viscosity, and of the soil, intrinsic permeability (k), is constant. But when the medium is partially saturated it is not, because the permeability (k) varies with the saturation degree (S_e). In the case of an unsaturated medium, as the pore space is occupied by two fluids (in this study water and air), the conductivity coefficient (K) is redefined by an effective permeability coefficient (K_e) related to one fluid. The subscript "e" to the coefficient K indicates that the conductivity is not necessarily that of a medium occupied by only one fluid. Usually, the effective conductivity (K_e) will be smaller than the conductivity (K) when only one fluid occupies the totality of the porous medium cavities, at saturated conditions. Then, the ratio K_e/K_{sat} is defined as the relative permeability (k_r) which reaches its maximum value of 1 at saturation (the cavities or the porous of the soil are fully with water). Then, rewriting the mass flux Eq. (6) for the effective conductivity (K_e) in terms of the relative permeability (k_{rel}) and the conductivity at saturated conditions (K_{sat}) gives

$$J_w = \rho_w \left(q_w^h + q_w^{eo}\right) = -\rho_w \left[K_{sat}^h k_{rel}^h \nabla(\Psi + z) + K_{sat}^{eo} k_{rel}^{eo} \nabla(\varnothing)\right] \tag{10}$$

where K_{sat}^h *and* k_{rel}^h are the saturated conductivity and the relative hydraulic permeability of the soil, respectively, and K_{sat}^{eo} *an* k_{rel}^{eo} are the electroosmotic saturated conductivity and the relative electroosmotic permeability of the soil, respectively. Then, both hydraulic and electroosmotic conductivities are defined as products of a permeability, depending on the microstructural properties of the porous medium, and a nondimensional relative permeability coefficient, which accounts for the effects of partial saturation on soil.

Relative permeabilities are functions of the saturation degree (S_e), and the estimates of them are especially difficult to obtain, partly and mainly because of its extensive variability in the field. Models have been used for calculating the unsaturated conductivity from the more easily measured soil-water retention curve, and analytical expressions have also been developed [36, 37]. To simplify the analysis of the present work, the model formulated by Eqs. (11) and (12), defined by the power law of the effective saturation, is adopted for the relative hydraulic and electroosmotic permeabilities, respectively [38]:

$$k_{rel}^h = a_h (S_e)^{b_h} \tag{11}$$

$$k_{rel}^{eo} = a_{eo} (S_e)^{b_{eo}} \tag{12}$$

where a_h, a_{eo}, b_h and b_{eo} are numerical curve fitting parameters. For a wide variety of soils, proposed values of b_h, for hydraulic flow, vary between 3 and 3.5 [34, 38–40]. For the case of compacted clay material, a value of $b_h = 5$ was suggested [41].
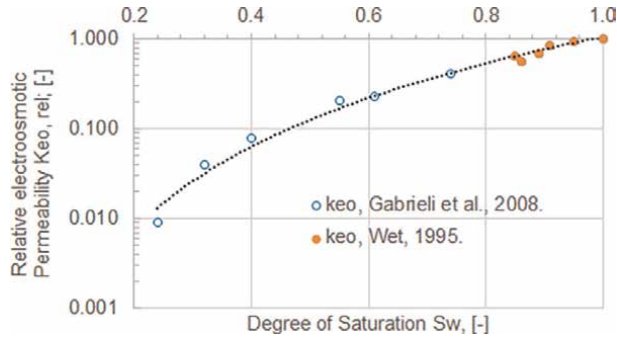
Figure 7.
Relative electro-osmotic permeability vs. saturation. The data adjusts well to the model expressed by eq. (12), with a value of 1 for a_{eo}, and a value of 3.2 for b_{eo} [38, 42, 43].

For the case of electroosmotic flow, the dependence of the saturation degree on the electroosmotic permeability was experimentally investigated in electrokinetic filtration tests [43]. The experimental results compare well with the results reported in **Figure 7** [43].

Rewriting Eq. (10) for the total mass flux, by inserting Eqs. (11) and (12) gives

$$J_w = -\rho_w \left[K_{sat}^h (S_e)^{b_h} \nabla(\varPsi + z) + K_{sat}^{eo}(S_e)^{b_{eo}} \nabla(\varnothing) \right] \tag{13}$$

4.1 Governing equations of electroosmotic flow in a porous media partially saturated

Unsaturated flow conditions in porous media correspond to a particular case of two-phase flow. Generally, the "non-wetting" phase, which in this case corresponds to the gas phase, is such that its pressure is constant, thus, this phase is considered as a stagnant or inactive phase.

4.1.1 Balance of the drained water mass flux

For the case of a porous media under the application of an electrical potential, the balance of the mass of water per unit volume in a porous medium is given by the expression:

$$\frac{\partial m_w}{\partial t} = \nabla J_w \tag{14}$$

where J_w is the total mass flux of water ($kg\,m^{-2}\,s^{-1}$), defined by two contributions, hydraulic and electroosmotic flow. The mass of water, m_w, per unit of total volume ($kg\,m^{-3}$) is defined as:

$$m_w = \varepsilon_p S_e \rho_w \tag{15}$$

where ε_p is the porosity of the soil, ρ_w is the water density, and S_e is the effective saturation. S_e is defined as the fraction of the total pore space occupied by the wetting phase, fraction dependent of the pressure head, and that can vary from point to point within the medium. The S_e is defined as:

$$S_e = \frac{(\theta - \theta_r)}{(\theta_s - \theta_r)} \tag{16}$$

with θ as the volumetric water content, defined as the volume of water per unit volume of soil (m^3/m^3), θ_s as the water content at saturation, and θ_r as the residual water content. By inserting Eq. (13), for the total mass flux, and Eq. (15), for the mass of water in the porous, into Eq. (14), the following equation is obtained:

$$\frac{\partial(\varepsilon_p S_e)}{\partial t} + \nabla\left[K_{sat}^h (S_e)^{b_h} \nabla(\Psi + z) + K_{sat}^{eo} (S_e)^{b_{eo}} \nabla(\emptyset)\right] = 0 \tag{17}$$

The conductivity coefficient, K_{sat}, is constant and determined at saturation conditions. The saturation degree, S_e, is dependent of the pressure head, ψ, and to solve this equation it is necessary also to solve the continuity equation for the current density (J_e) that is obtained by doing a charge electric balance.

4.1.2 Balance of electric charge

In the presence of an external electric field, the balance of electric charge equation is expressed as:

$$\nabla \cdot J_e + \frac{\partial Q_e}{\partial t} = 0 \tag{18}$$

where J_e is the electric current density and Q_e is the charge density per unit volume. Neglecting the soil electric capacitance, the source term in Eq. (18) vanishes and the equation reduces to:

$$\nabla \cdot J_e = 0 \tag{19}$$

Neglecting the contribution of streaming currents produced by liquid flow, the equation for the electric current density, J_e, is provided by the Ohm's law for the porous medium:

$$J_e = -k_e \nabla \emptyset \tag{20}$$

where k_e is the effective electric conductivity of the unsaturated porous medium that can be expressed as the sum of two terms [44]:

$$k_e = k_{es} + k_{esat} k_{erel} \tag{21}$$

where k_{es} is the apparent electric conductivity of the solid and generally assumed negligible, k_{esat} is the apparent electric conductivity of bulk pore water under saturated conditions, and k_{erel} is the relative electrical conductivity, accounting for the effects of partial saturation. The following power law has been assumed in this work [44, 45]:

$$k_{erel} = a_e (S_e)^{b_e} \tag{22}$$

where a_e and b_e are fitting parameters, with a_e = 1 and b_e = 2, as suggested by literature experimental data [45, 46]. Then, by inserting Eqs. (20)–(22) into Eq. (19), the following equation is obtained:

$$\nabla \cdot k_{esat}(S_e)^{b_e} \nabla \emptyset = 0 \qquad (23)$$

4.1.3 Approach of the effective Saturation

Then, to solve the system of Eqs. (17) and (23), it is necessary to find some mathematical model that correlates the dependence of S_e with the pressure head. In scientific literature, numerous models of soil-water retention curve and permeability have been reported, showing that dependence [36, 46]. Then the effective saturation, S_e, could be estimated using van Genuchten's retention curve model formulated as:

$$S_e = \left[\frac{1}{1 + (\alpha \cdot \Psi)^n} \right]^m \qquad (24)$$

where "α", "n", and "m" are fitting parameters, and "ψ" is the matric suction defined by the pressure difference at the interface between the gas (air) and liquid (water) and named as pressure head. Combining Eqs. (16) and (24), the following equation is obtained:

$$\theta = \theta_r + \frac{(\theta_s - \theta_r)}{[1 + (\alpha \Psi)^n]^m} \qquad (25)$$

where, the pressure head, ψ, is positive, and the parameters "m" and "n" are correlated by Mualem's model [45] as:

$$m = 1 - \frac{1}{n} \qquad (26)$$

Eq. (25) contains four independent parameters (θ_r, θ_s, α, and n), which must be estimated from observed soil-water retention data. A graphical methodology may be found in a paper written by Van Genuchten (1980) [45].

The functional relationship of S_e, Eq. (24), used to estimate the relative permeability of the unsaturated porous media, has not a unique value because it is affected by hysteresis. The value of k_{rel} is different if S_e is obtained by starting with a dry medium and increasing the liquid saturation than if S_e is obtained by removing liquid from an initially vacuum-saturated medium. Hereby, as this paper is concerned with the drainage of liquid, by the moment, the hysteresis problem will be not considered, only as a way of simplifying the estimate of k_{rel}.

5. Application of the electroosmotic flow model

Once the copper is extracted from the ore through a heap leaching process, an acid-wetted solid waste is left with a 15–18% moisture. At the beginning of the leaching cycle, the agglomerated mineral has a good permeability, approximately 10^{-4} cm/s, but at the end, because of the drag of fine material (mainly clay or some precipitate generated during the leaching cycle) by the leaching solution, the permeability at the bottom of the heap become lower, making not easy the drainage of solution by gravity. The application of the electroosmotic model will be done to a copper leaching heap in its last stage of the leaching process, in the drainage step before to dispose the waste material left after the copper extraction.

The drainage electroosmotic model formulated by Eqs. (14)–(26) describes the partial saturated heap with a volumetric water content, θ, varying with height of the heap, showing larger water content at the bottom than at the top of the heap, *at t =* 0, $H = -(y + 2)$, where (H) is the hydraulic head and (y) is the independent variable of position related to the y-axis. The hydraulic head H is related to the water volumetric content θ by developing Eqs. (5) and (25). The initial electric field is assumed to be zero everywhere: *at t = 0, V = 0*. The boundary conditions (BCs) are no flow across the boundary top and through the right vertical side of the heap pile. At the left wall, a symmetry boundary is assumed (**Figure 8** shows the sketch of the 2D pile). At the bottom, the boundary condition is open and free draining. For the electric BC, the voltages are maintained at the top and bottom, whereas all other boundaries are assumed to be isolated to the electric current. The parameters required by the model are listed in **Table 5**.

The results of the simulation, including hydraulic and electroosmotic flow, are represented in **Figure 8** for the volumetric water content θ at initial time and after 480 minutes. These results are only demonstrative, because the data used in the simulation are only slightly approximated to the studied case. In addition to the volumetric water content, **Figure 8** shows the schematic view of the 2D pile to be simulated (8 meters wide and 2 meters high). The anode and cathode bars, represented by circles, locate at the top and bottom, respectively.

The simulation results represented in **Figure 8** show the dewatering evolution of the heap leaching in a situation where the mineral bed presents a very low hydraulic permeability and high electroosmotic conductivity (see **Table 5**). This means that the relevant driving force, responsible of the drainage process, is the electroosmotic force. This situation may be realistic only if during the leaching process, it exists a great drag of fine material toward the bottom of the pile that could difficult the drainage of solution from the pile. Due to the lack of field data, (permeability, porosity, volumetric water content, and soil-water characteristic curve (SWCC)) for the studied case, it is not possible to make a comparison with results obtained from an experimental pilot test of one cubic meter of acid mining waste, realized and documented previously [11].
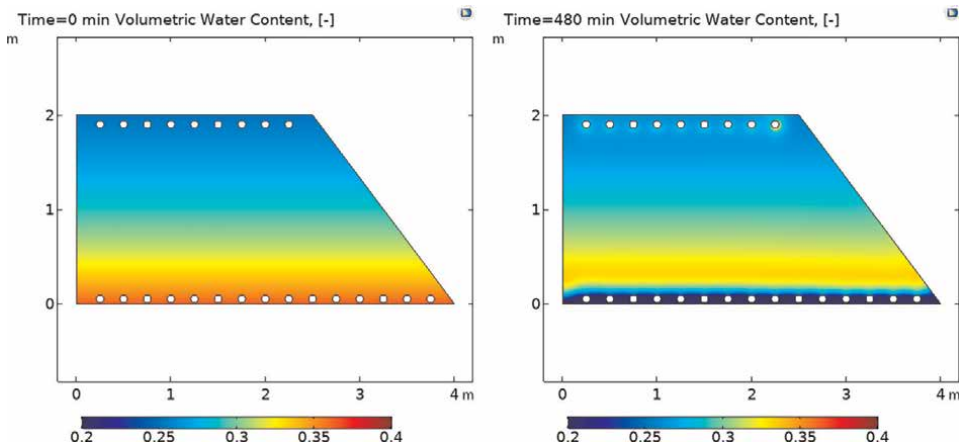
Figure 8.
Volumetric water content, in cm³ of water per cm³ of soil, varying between 0 and 1, of the leaching pile in 2D, at (a) initial time; and (b) time of 480 minutes. (Software Comsol Multiphysics).

Parameter	Value	Description	Unit
ε_p	0.1–0.7	Porosity	—
θ_r	0.13	Residual volumetric water content	—
θ_s	0.70	Volumetric water content at saturation	—
α_{cr}	1.70	Parameter of the water retention curve model	1/m
n_{cr}	1.38	Parameter of the water retention curve model	—
K_{sath}	10^{-6}–10^{-11}	Hydraulic conductivity at saturation	m/s
K_{sateo}	10^{-9}–10^{-8}	Electroosmotic conductivity at saturation	$m^2/V/s$
K_{sate}	3.5×10^{-4}	Electric conductivity at saturation	S/m
sign	1 or -1	Sign of the zeta-potential	—
b_h	3.5	Parameter of hydraulic relative conductivity model	—
b_{eo}	3	Parameter of electroosmotic relative conductivity model	—
b_e	2	Parameter of electric relative conductivity model	—
ρ_b	1012	Bulk density of solution	Kg/m^3
σ_e	0.01–1.0	Electric conductivity coefficient of the soil	S/m
V_{anode}	200	Anode voltage	V
$V_{cathode}$	0	Cathode voltage	V

Table 5.
Parameters utilized in the simulations for the case of a heap leaching.

6. Conclusion

The two-phase fluid flow in porous media may be used to explain the drainage from a residue with high humidity, taking into consideration two driving forces, defined by the hydraulic and electric potentials. Electroosmotic flow is significative only when water is trapped capillary, as in those samples where the fraction of fine material is considerable. In an electroosmotic process, the movement of the water is from the anode toward the cathode; thus, the soil water content will decrease at the anode and will increase at the cathode. Thus, to discharge the water, a drainage system has to be provided at the cathode proximity.

To apply the electroosmotic model in the dewatering process of mining waste, it is necessary to know beforehand some hydraulic and electrical parameters such as permeability, porosity, volumetric water content, and the soil-water characteristic curve.

Acknowledgements

Conflict of interest

The authors declare no conflict of interest.

Author details

Leonardo Romero[1]*, Manuel Cánovas[2] and Juan Sanchez-Perez[3]

1 Department of Chemical Eng., Universidad Católica del Norte, Antofagasta, Chile

2 Department of Metallurgy and Mines, Universidad Católica del Norte, Antofagasta, Chile

3 Department of Applied Physics and Naval Technology, Universidad Politécnica de Cartagena, Spain

*Address all correspondence to: leon@ucn.cl

IntechOpen

References

[1] Casagrande L. Electroosmosis in soils. Geotechnique. 1949;**1**:159-177

[2] Casagrande L. Electroosmotic stabilization of soils. Journal of the Boston Society of Civil Engineers. 1952;**39**:51-83

[3] Runnells D, Wahli C. In situ electromigration as a method for removing sulphate, metals and other contaminants from groundwater. Ground Water Monitoring & Remediation. 1993;**13**(1):121-129

[4] Shapiro AP, Probstein RF. Removal of contaminants from saturated clay by electroosmosis. Environmental Science & Technology. 1993;**27**(2):283-291

[5] Reddy KR, Urbanek A, Khodadoust AP. Electroosmotic dewatering of dredged sediments: Bench-scale investigation. Journal of Environmental Management. 2006;**78**(2):200-208

[6] Fourie AB, Johns DG, Jones CF. Dewatering of mine tailings using electrokinetic geosynthetics. Canadian Geotechnical Journal. 2007;**44**(2):160-172

[7] Bertolini L, Coppola L, Gastaldi M, Redaelli E. Electroosmotic transport in porous construction materials and dehumidification of masonry. Construction and Building Materials. 2009;**23**(1):254-263

[8] Pham AT, Sillanpää M, Virkutyte J. Sludge dewatering by sand-drying bed coupled with electro-dewatering at various potentials. International Journal of Mining, Reclamation and Environment. 2010;**24**(2):151-162

[9] Xue Z, Tang X, Yang Q, Wan Y, Yang G. Comparison of electroosmosis experiments on marine sludge with different electrode materials. Drying Technology. 2015;**33**(8):986-995

[10] Burns CJ, Wright D. Electrokinetic leaching. Hydrometallurgy. 1997;**46**(3):394

[11] Valenzuela J, Romero L, Acuña C, Canovas M. Electroosmotic drainage, a pilot application for extracting trapped capillary liquid in copper leaching. Hydrometallurgy. 2016;**163**:148-155

[12] Yoshida H. Practical aspects of dewatering enhanced by electro-osmosis. Drying Technology. 1993;**11**(4):784-814

[13] Vesilind PA. The role of water in sludge dewatering. Water Environment Research. 1994;**36**:4-11

[14] Zhou J, Liu Z, She P, Ding F. Water removal from sludge in a horizontal electric field. Drying Technology. 2001;**19**(3–4):627-663

[15] Cornelissen P, Leijnse A, Joekar-Niasar V, Van der Zee S. Pressure development in charged porous media with heterogeneous pore sizes. Advances in Water Resources. 2019;**128**:193-205

[16] Joekar-Niasar V, Mahani H. Nonmonotonic pressure field induced by ionic diffusion in charged thin films. Industrial and Engineering Chemistry Research. 2016;**55**:6227-6235

[17] Godinez-Brizuela O, Niasar VJ. Effect of divalent ions on the dynamics of disjoining pressure induced by salinity modification. Journal of Molecular Liquids. 2019;**291**:111276

[18] Sherwood J, Mao M, Ghosal S. Electroosmosis in a finite cylindrical pore: Simple models of end effects. Langmuir. 2014;**30**:9261-9272

[19] Coelho D, Shapiro M, Thovert JF, P. M. Adler PM. Electroosmotic phenomena in porous media. Journal of Colloid and Interface Science. 1996;**181**: 169-190

[20] Yeung AT. Coupled flow equations for water, electricity and ionic contaminants through clayey soils under hydraulic, electrical and chemical gradients. Journal of Non-Equilibrium Thermodynamics. 1999;**15**(3):247-267

[21] Alshawabkeh AN, Acar YB. Electrokinetic remediation. Theoretical model. Journal of Geotechnical Engineering. 1996;**122**(3):186-196

[22] Hunter RJ. Zeta Potential in Colloid Science: Principles and Applications. London: Academic; 1981

[23] Eykholt GR, Daniel DE. Impact of system chemistry on electroosmosis in contaminated soil. Journal of Geotechnical Engineering. 1994;**120**(5): 797-815

[24] Colin J, Lamon-Black J, Glendinning S. Electrokinetic geosynthetics in hydraulic applications. Geotextiles and Geomembranes. 2011; **29**(4):381-390

[25] Mitchell JK, Soga K. Fundamentals of Soil Behaviour. Hoboken, New Jersey, USA: John Wiley & Sons, Inc; 2005

[26] Nozari MA, Ziaie MR. A simplified analytical approach for coupled injection of colloidal silica with time dependent properties. International Journal of Chemical, Molecular, Nuclear, Materials and Metallurgical Engineering. 2016; **10**(1)

[27] Yeun AT. Electrokinetic Flow Processes in Porous Media and Their Applications. In: Corapcioglu MY, editor. Advances in porous media 2. Amsterdam, The Netherlands: Elsevier Science; 1994. pp. 309-395

[28] Page M, Page C. Electroremediation of contaminated soils. Journal of Environmental Engineering. 2002; **128**(3):208-219

[29] Vijh AK, Novak JP. A new theoretical approach to electroosmotic dewatering (Eod) based on non-equilibrium thermodynamics. Drying Technology. 1997;**15**(2):699-709

[30] Lockhart NC. Combined field dewatering: Bridging the science-industry gap. Drying Technology. 1992; **10**(4):839-874

[31] Ravindra K, Dhir OBE, de Brito J, Mangabhai R, Lye CQ. Use of copper slag in geotechnical application. Sustainable Construction Materials: Copper Slag Book. 2017:211-245. DOI: 10.1016/B978-0-08-100986-4.00006-7

[32] Citeau M, Olivier J, Mahmoud A, Vaxelaire J, Larue O, Vorobiev E. Pressurised electro-osmotic dewatering of activated and anaerobically digested sludges: Electrical variables analysis. Water Research. 2012;**46**(14):4405-4416

[33] Li Q, Lu X, Guo H, Yang Z, Li Y, Zhi S. Sewage sludge drying method combining pressurized electro-osmotic dewatering with subsequent bio-drying. Bioresource Technology. 2018;**263**:94-102

[34] Mitchell JK. Conduction phenomena: From theory to geotechnical practice. Geotechnique. 1991;**41**(3):299-340

[35] Canovas M, Valenzuela J, Romero L, Gonzalez P. Characterization of electroosmotic drainage: Application

to mine tailings and solid residues from leaching. Journal of Materials Research and Technology. 2020;**9**(3): 2960-2968

[36] Brooks R, Corey A. Hydraulic properties of porous media. Hydrology Papers. 1964;**3**:318-333

[37] Brooks R, Corey A. Properties of porous media affecting fluid flow. Journal of the Irrigation and Drainage Division. American Society of Civil Engineers. 1966;**92**(IR2):61-88

[38] Tamagnini C, Jommi C, Cattaneo F. A model for coupled electro-hydro-mechanical processes in fine grained soils accounting for gas generation and transport. Anais da Academia Brasileira de Ciências. 2010;**82**(1):169-193

[39] Boreli M, Vachaud G. Note sur la determination de la teneur en eau residuelle etsur la variation de la permeabilite relative dans les sols non satures. Comptes Rendus de l'Académie des Sciences. 1966;**263**:698-701

[40] Caruso M, Jommi C. An evaluation of indirect methods for the estimation of hydraulic properties of unsaturated soils. In: Bilsen H, Nalbantoglu Z, editors. Problematic Soils. Vol. 1. Eastern Mediterranean University Press; 2005. pp. 183-191

[41] Wei-Hai Y, Hicks M. Numerical evaluation of optimal approaches for electro-osmosis dewatering. Drying Technology. 2017;**36**(8). DOI: 10.1080/07373937.2017.1367693

[42] Gabrieli L, Jommi C, Musso G, Romero E. Influence of electroosmotic treatment on the hydromechanical behaviour of clayey silts: Preliminary experimental results. Journal of Applied Electrochemistry. 2008;**38**(7): 1043-1051

[43] De Wet M, Electro-kinetics, infiltration and unsaturated flow. In: Alonso and Delage (Eds), Unsaturated Soils. A.A. Balkema, Rotterdam; 1995, 1, p. 283–291

[44] Mualem Y, Friedman S. Theoretical prediction of electrical conductivity in saturated and unsaturated soil. Water Resources Research. 1991;**27**(10): 2771-2777

[45] Mattson ED, Bowman RS, Lindgren ER. Electrokinetic ion transport through unsaturated soil: 1. Theory, model development, and testing. Journal of Contaminant Hydrology. 2002;**54**(1–2):99-120

[46] Van Genuchten M. A closed-form equation for predicting the hydraulic conductivity of unsaturated soil. Soil Science Society of America Journal. 1980;**44**:892-898

Chapter 3

Refractories for the Metallurgy of Copper

Andrey Yurkov

Abstract

Copper in the molten state is a rather reactive metal, and it interacts with the refractory lining of the furnaces, but the copper slags and copper matter are much more reactive. The processes in primary metallurgy of copper (purification of copper matte to blister copper) and secondary metallurgy of copper (re-melting of cathode copper and alloying) differ. The processes in primary metallurgy of copper have big differences, as a consequence, the types of furnaces in primary copper metallurgy have considerable peculiarities. However, in reverberatory, flash, electric furnaces and convertors the refractories are more or less similar. In re-melting furnaces, there are principally other silicon carbide-based refractories. A short description of the most common refractories, used in the furnaces and runners, corrosion behavior of refractories in contact with the molten slag and molten copper, corrosion resistance and corrosion tests, are made. There are some words about the service lifetime of the furnaces and repairs with a respect to corrosion testing and structure of refractories, and the possibilities of improving the service lifetime on refractories in the furnaces.

1. Introduction

The annual world production of copper is about 20 million tons, which is *a considerable amount*. However, this big amount is not that big, compared with the annual production of 64 million tons of aluminum and almost 2000 million tons of steel.

The specific consumption of refractories in copper metallurgy is high due to the very aggressive nature of copper melt and the extremely high aggressive nature of copper matte and slags. The literature on the corrosion of refractories in copper production is limited. There is no information on the values of the crucible static corrosion test and rod dynamic corrosion test of refractories to molten copper matte and molten copper slag. Probably the reason for the lack of this information is rather low total refractory consumption in copper metallurgy, that in 1998 was estimated by Schlesinger [1] as 25 thousand tons (copper production in 1996 was 12,772 million tons [2].

The specialists in steel production and refractories application in the ferrous industry use the term "the specific consumption of refractory per ton of melted metal" since 70–80th of the past century. At that time they calculated the specific

consumption of refractories in kilograms per ton, but during the last ten years, they started to calculate the specific consumption in USD per ton [3].

The consumption of refractories plays a certain role in the cost calculations. Untimely shutdowns and unexpected repairs of the furnaces also have certain income in the increase of the cost production of copper.

2. Process stages and the refractories in the copper smelting process

Copper concentrate (produced from ore) is melted in furnaces (reverberatory, flash, electric) to produce matte, that transforms in the convertor to blister copper (**Figure 1**). In the following oxidation refining complex, the casting anodes for the purpose of electrolysis are produced, and electrolytic copper with a grade of up to 99.9% is melted in the shaft furnaces to produce copper alloys [4].

The most used lining refractory material in the metallurgy of copper is chromium-magnesite refractory. Magnesia, magnesia-spinel ($MgO*Al_2O_3$), and dolomite ($MgO*CaO$) refractories are also used in copper metallurgy, but generally speaking, the resistance of chromite-magnesia refractories is superior to all other said above materials.

The exception from this baseline of oxide refractories is silicon nitride bonded silicon carbide refractory lining in the shaft furnaces for re-melting of electrolytic copper.

The ratio of Cr_2O_3 to MgO in Cr_2O_3*MgO - chromite-magnesite refractory is a question of investigations, the specific conditions of the service, and to some extent "know-how" of refractory engineering companies.

The main advantage of adding chrome ore to magnesia raw materials is the increase of the resistance to basic slags. Usually, chrome ore contains alumina, and refractory
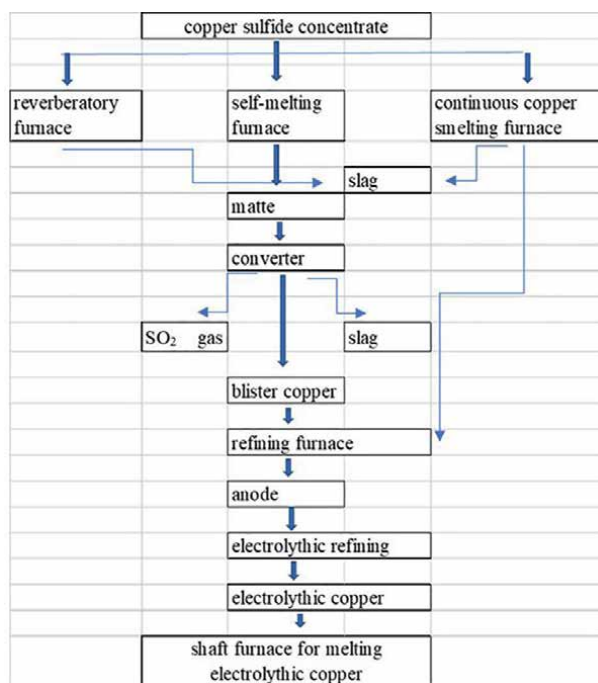

Figure 1.
Copper smelting process according to [5].

Composition, %	Producer						
	A	**B**	**C**	**D**	**E**	**F**	**G**
MgO	59,2	58,9	61	60	55	56,6	24,2
Cr_2O_3	19,6	19,8	19,6	12	20	21	29,3
Al_2O_3	7,2	6,7	5,9			7,5	16,3
SiO_2	1,9	0,9	0,8			1,3	2,8
CaO	1,2	0,9	1,2			1,1	2,4
Fe_2O_3	10,9	12,8	11,4			12,5	22,3
Properties							
apparent density, g/sm^3	3,12	3,25	3,09	3	3,09	3,12	—
open porosity, %	17,5	15,5	18	16	18	17,5	14
cold crushing strength, Mpa	39	45	37	50	40	40–50	40–50
bending strength, Mpa	7	7	4			6–7	6–7
hot modulus of rapture, Mpa	6	6					
linear change at 1700°C	<+0,1%	<+0,1%	<+0,1%			<+0,1%	—

Table 1.
Chemical composition and properties of chrome-magnesia bricks of various producers.

producers do not purify chrome ore from alumina. So, in general, chrome-magnesia bricks contain 20–30% of Cr_2O_3, 25–55% MgO and up to 20% of Al_2O_3 (**Table 1**).

These refractories have a very high temperature of sintering, the firing temperature for such inert materials may be 1800°C or even more.

Some time ago the main type of chrome-magnesia refractories for the copper industry was so-called silicate bonded materials. Silica from chrome ore reacts with magnesia to form a silicate bond (that is deteriorated by fayalite Fe_2O_3-SiO_2 slag in reverberatory, flash, electric furnaces and converters).

The next step in the technology of refractories for copper furnaces is the so-called direct bonded chrome-magnesia refractories. For such types of refractories more high-purity materials are used to achieve the direct bond between the grains of periclase and chromite and grains of spinel without silicate interlayers between the grains.

Another type of chrome-magnesia material is so-called rebounded refractories. Magnesia and chrome ore are melted in an electric arc furnace to produce fused chrome-magnesia aggregate. The ground powders are shaped and fired to receive bricks with excellent corrosion resistance.

The electrolytic cathode copper sheets are melted in a continuous melting shaft furnace, and the alloys are prepared in a mixer – a small drum horizontal furnace. The approved variant for the refractory lining of the shaft furnaces [5] is silicon nitride bonded silicon carbide refractory or N-SiC. In shaft re-melting furnaces, there is almost no contact of the refractory material with slag, ad relatively limited contact with purified copper. Nitride-bonded silicon carbide refractory offer excellent thermal shock resistance and relatively high oxidation and weak resistance. The properties of the materials are in **Table 2**.

	Producer	
Properties	**A**	**B**
SiC, %	72,0	78-75
Si_3N_4, %	27,8	22-25
α-Si_3N_4, %	12,0	α/β ratio is from 1:2 to 2:1
β-Si_3N_4%	12,4	
C free, %	0,15	-
Si free, %	0,21	<0,5
SiO_2%	—	Oxides in total <1,2%
Al_2O_3, %	0,23	
CaO, %	0,25	
Fe_2O_3 %	0,58 (0,4)	
Porosity, %	16,6	14–18
Cold crushing strength, MPa	160	>150
Modulus of rapture, MPa	35	30–40

Table 2.
Chemical composition and properties of Si_3N_4-SiC bricks of various producers.

The conditions in each type of furnace in the copper smelting process differ, but the refractory materials for the furnaces are more or less the same. Barthel summarized the types of transformation of different parts of reverberatory and flash smelting furnaces [5]. The most corrosive agent in the reverberatory furnace is slag, and the most influenced part of the furnace is walls. The picture in the flash smelting furnace is a little bit more complex. The settlers of the furnace are corroded by matte and blister copper very intensively.

In flash smelters, the most corroded zones are the reaction shaft and the slag line. Lower MgO compositions are preferred because magnesia grains react with silicon oxide in the slag. The off-gas shaft and sidewalls are less subjected to slag attack.

In reverberatory furnaces, the situation is approximately the same but the contact of refractories with slag and matte is lower, the consequence is a slightly longer service life.

In fire-refining (anode) furnaces there are almost no silica-containing slags (if compared with flash furnaces and reverberatory furnaces), and refractory engineers often use magnesite refractories. Yet, magnesia-chromite refractories are still popular.

Yet probably the biggest challenge in corrosion resistance and the service lifetime for refractories is in converters, where the matter transforms to slag and blister copper. Slag corrodes the lining, but erosion also has income in the degradation of the lining and the tuyeres.

Magnesia-chromite refractories are used in converters, and the preference is high chromium compositions with high purity materials and low porosity. Fayalite (iron silicate) slag and copper oxide slag strongly deteriorate the refractory lining, especially the borders between grains in silicate bonded magnesia-chromite refractories.

3. Some words on testing of refractories

Refractories should be corrosion-resistant to melts and gases in furnaces and high-temperature devices in copper metallurgy. It is considered [6, 7] that, in general,
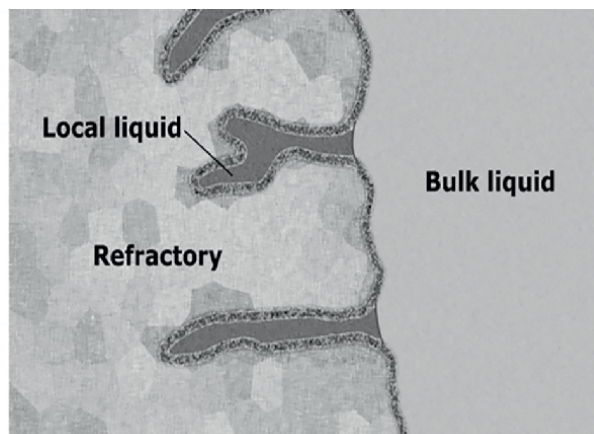
Figure 2.
Porous refractory in contact with molten liquid (metal or slag).

approximately one-third of refractories are damaged because of poor thermal shock resistance at temperatures sufficiently lower than refractoriness, and two-thirds (2/3) of refractories go out of service due to lack of chemical resistance. It means, that 2/3 of shutdowns of the furnaces take place to the poor corrosion resistance of refractories.

Corrosion phenomena are very complex, and it is necessary to consider different processes and mechanisms of degradation and deterioration.

The corrosion includes the chemical reactions on the border of solid refractory and liquid melts, but it is also necessary to take into account the transport of reagents to the reaction zone and the drift of reactants from the reaction zone. In case of refractories, it is necessary to consider the penetration of aggressive liquids in open permeable pores (**Figure 2**), the wetting, the diffusion of the aggressive melts (or constituents of the aggressive melts) into the structure of refractory materials, and others.

In metallurgy, the corrosion behavior of refractories is estimated by corrosion tests. Laboratory corrosion tests may be divided into static cup tests and dynamic rod tests. Static and dynamic laboratory corrosion tests are carried out from 2 to 50 hours and provide information on the corrosion resistance of refractory material to liquid metal or slag.

There is no universal standard cup test for corrosion resistance, but metallurgists use the cup test (**Figure 2**), for comparative investigations [6] for almost a century. The test is simple and provides the information.

In order to make a cup test, a hole about 35–58 mm in diameter and about 40 mm deep is drilled in a brick (**Figures 2** and **3**), and either the corrosive liquid (metal or slag) is poured into the hole, but more frequently the corrosive agent in the solid state is placed in this hole before testing. The brick with the corrosive agent in a "cup" (hole) and with a lid above is placed in a furnace for 8–24 hours. The cup (hole) in a refractory castable may be made in advance without drilling, and for dry barrier mixtures, a cup with sloped sides is formed with a help of a special shape mold. After cooling, the sample brick with a cup and aggressive liquid is cut into two pieces, and the infiltrated area in the tested brick is measured (in square centimeters). This infiltrated area is a measure of corrosion resistance. The standards for cup corrosion resistance ASTM C768–99 [8] and DIN 51069–2-1972 [9] were withdrawn. However, the method of testing fireclay brick for corrosion resistance to cryolite is in standard ISO 20292 [10], and the standard DIN [11] guidelines for corrosion testing are valid.
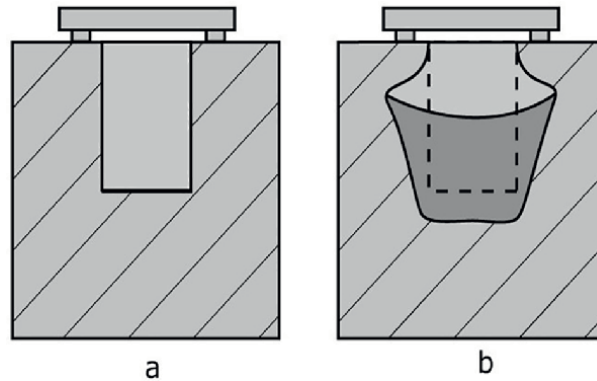
Figure 3.
Static corrosion cup test. a – The cross-section of refractory brick with a hole for metal or slag before the test; b – The cross-section of a refractory brick after exposure to reactive metal or slag. The increased surface of the cross-section after exposure is a measure of the corrosion resistance of the refractory.

The dynamic rod test (**Figure 4**) is more complex from the point of apparatus [12–14], and is used **not** so often. The dynamic rod tests are produced in big crucibles or vessels, filled with at least one corrosive agent. The dimensions of the tested rods (usually rectangular bars) may vary from "25 mm*25 mm*100 mm" to "10 mm*10 mm*150 mm". The bars of investigated materials may be rotated in aggressive liquid or be dipped in aggressive liquid and pulled out. There are variants of testing without rotation (**Figure 5**) [13].

The term "static corrosion test" means that the corrosive liquid in the cup is in a stationary condition, it does not move against or around the tested refractory, so the system "corrosive liquid–refractory" may reach equilibrium. During a "dynamic" test, there is a movement of the tested sample in the corrosive liquid, there are no stationary conditions between the refractory surface and the corrosive liquid, and the thermodynamic and chemical equilibria between the tested refractory and corrosive liquid will not be reached.

The corrosion resistance in dynamic testing is estimated in the decrease of the weight of the tested materials or the decrease of the volume of the tested rods.

Figure 4.
The results of the corrosion resistance cup test of refractory material to molten aluminum (Mg alloy). a – Conventional refractory fireclay shamotte brick; b – Special refractory with anti-wetting (for molten aluminum) additives (almost undamaged).
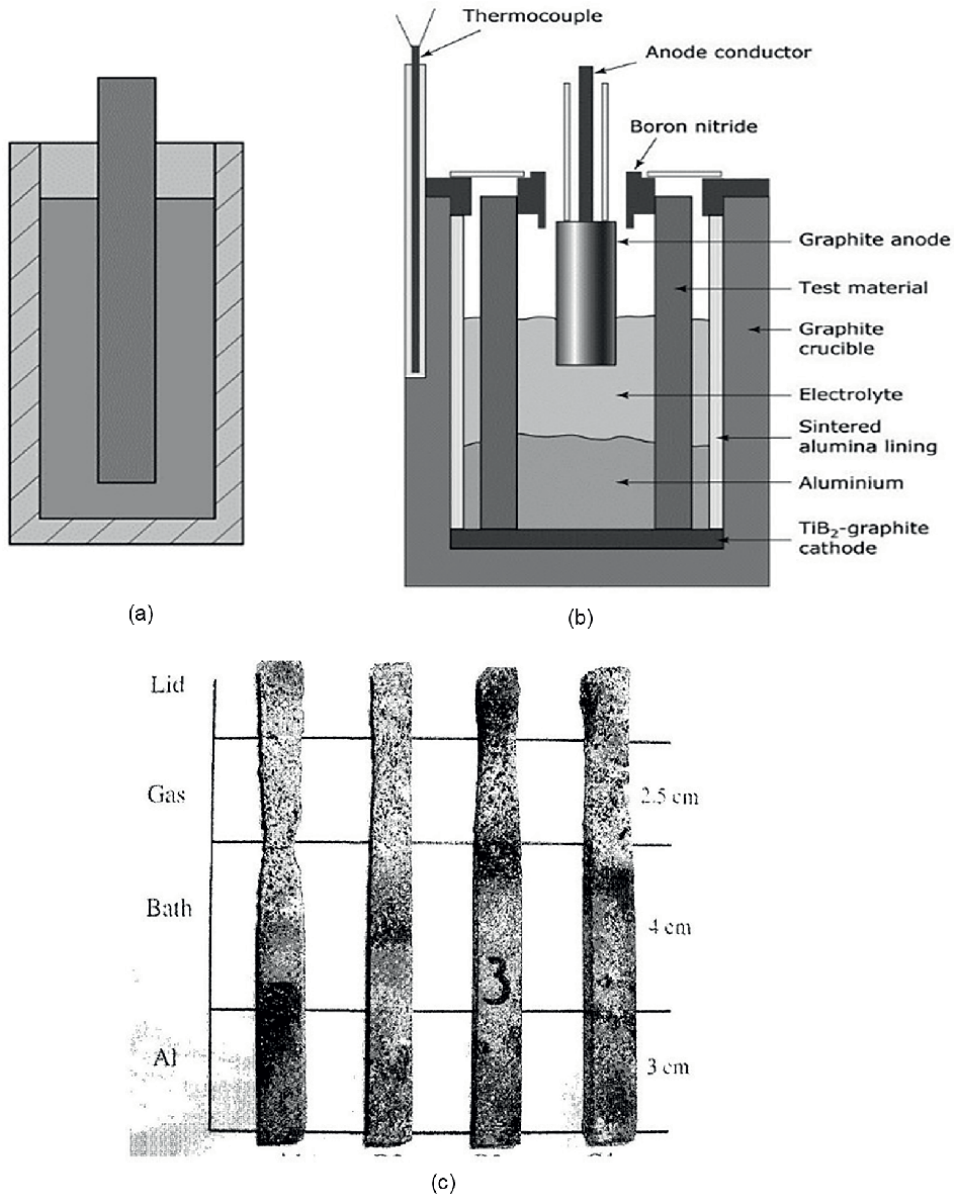
Figure 5.
The scheme (a) of dynamic rod test; the scheme of dynamic rod test for SiC refractory (b) in molten cryolite and aluminum [13]; the rods after exposure to molten cryolite and aluminum after 50 hours at 965°C [7].

Usually, corrosion tests are isothermal. If there are possibilities, it is very good to investigate the structure of the corroded materials (the shape of the corroded grains, the depth of penetration of the liquids in the pores, etc.) with the help of a microscope.

At copper plants sometimes "industrial" testing of corrosion resistance is performed. Such kind of testing, although time-consuming, opens the way to the understanding of the processes, that take place at the service of materials. The investigation of corrosion of Si_3N_4-SiC refractory by the melt of copper and the copper slag was performed in the

slag collector [15]. The tested refractory plate was the siphon block (the separator of slag) of the slag collector in the runner of the cathode shaft furnace. This plate (siphon block) is exposed to the permanent flow of copper with a small amount of slag. The slag on the surface of the melt is stopped by a refractory plate (separator). The refractory plate is exposed to the most extensive corrosion wear. However, this refractory plate is a good object for investigation of corrosion resistance, because different parts of this plate are exposed to intensive corrosion by flowing copper and flowing copper slag. General observations had shown that the corrosion of Si_3N_4-SiC refractory by slag is more extensive (the wear is about 3 mm per month), while the wear of Si_3N_4-SiC refractory by the flowing copper is below 1 mm per month.

Microscopic investigations of Si_3N_4-SiC refractory after 6 months of the service in said above conditions had shown 4–5 zones of a different color. There were no changes in the material in direct contact with molten copper without exposure to air. This show on the slow dissolution of silicon carbide and silicon nitride in the flowing melt of copper (physical dissolution in case of permanent removal of reactants). The most severe wear of Si_3N_4-SiC refractory was by copper slag.

Big refractory companies make investigations on corrosion resistance of refractories to copper and copper matte and perform cup testing [14], but publish results without details on the structure of refractories.

So, there is no information on more or less systematic investigations on corrosion resistance of refractories for copper metallurgy with a respect to the structure of refractories.

4. Some words on the structure of the refractory materials for metallurgy

The corrosion tests of refractories are made already for a century. The corrosion tests are performed to estimate if the specific refractories with being resistant to the attack of corrosive liquids (molten metal and slag) with a forecast for a long-term service lifetime of the furnace in a specific metallurgical process.
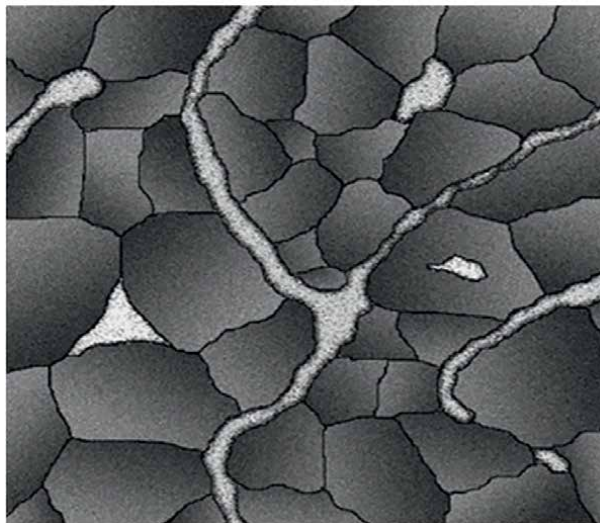
Figure 6.
The scheme of the pore structure of conventional refractory with closed pores, tunnel pores and open dead-end pores [7].
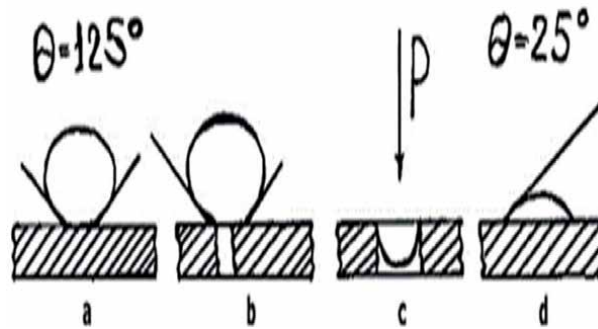
Figure 7.
The variants of appearance of the liquid in the open pores of refractory depending on the wetting contact angle [7].

In real metallurgical processes, many factors affect corrosion [11]. However, in general, they may be divided into two – the chemical inertness of refractory and pore structure.

In **Figure 2**, it is shown that the liquid may penetrate tunnel permeable pores and open dead-end pores. The possibility of penetration of corrosive liquid in the open pores depends on the wetting of refractory and the pore size (**Figure 6**). Sometimes liquid cannot penetrate in the small pores but can easily penetrate in the pores with big diameters.

The value of open porosity (**Tables 1** and **2**) is essential in the estimation of the service of the refractory in corrosive media, but the pore size distribution (**Figure 7**) is much more important. The value of the average pore size may correlate with the gas permeability, which is also very important in the estimation of the correlation between the laboratory corrosion test, the chemical composition, and the structure of refractory
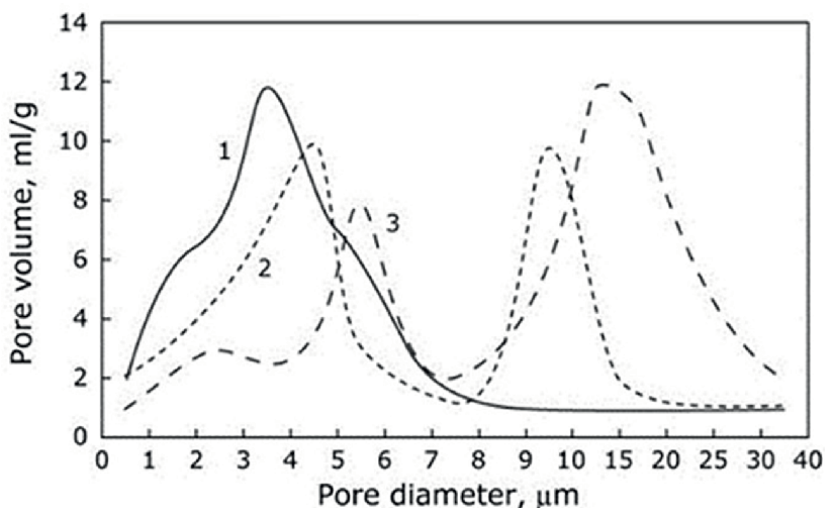
Figure 8.
The variants of the pore size distribution in alumina-silica refractory depend on the processing of refractory. The possibility of intrusion of corrosive liquid in the pores of material 1 (pore size 3,5 μm) is sufficiently lower than in materials 2 (pore size up to 10 μm) and 3 (pore size up to 15–20 μm) [7].

material. The values of gas permeability and pore size distribution may say something on the forecast of the service life of refractory in metallurgical vessels (**Figure 8**).

5. Conclusions

1. Copper in the molten state is a rather reactive metal, and it interacts with the refractory lining of the furnaces, but the copper slags and copper matter are much more reactive, which causes a limited-service lifetime of the furnaces in copper metallurgy.

2. The most used lining refractory material in the metallurgy of copper is chromium-magnesite refractory. Magnesia, magnesia-spinel (MgO*Al2O3) and dolomite (MgO*CaO) refractories are also used in copper metallurgy, but generally speaking, the resistance of chromite-magnesia refractories is superior to all other said above materials.

3. The corrosion resistance investigations of refractories for copper metallurgy, coupled with the investigations on pore structure and gas permeability, may give rise to an increase in the service lifetime of the furnaces, that finally may have certain income in the reduction of the cost.
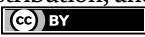
Author details

Andrey Yurkov
Mendeleev University of Chemical Technology of Russia, Moscow, Russia

*Address all correspondence to: and-yur@mail.ru; andrey.yurkov@muctr.ru

IntechOpen

References

[1] Schlesinger MA. Refractories for copper production. Mineral Processing and Extractive Metallurgy Review;**16**(2):125-146

[2] Annual Data 2017 Copper Supply & Consumption — 1996-2016, Copper Development Association, Copper Alliance. Availale from: www.coppper.org

[3] Shinichi T. Trends in Refractories R & D Overseas, Nippon Steel Technical Report No. 125, UDC 666.76. 2016

[4] Refractories Handbook. Japan; 1998. p. 578

[5] Yje B. Wear of chrome magnesite bricks in copper smelting furnaces. Interceram. 1981;**30**:250-255

[6] Poirier J, Rigaud M. Corrosion of Refractories. Baden Baden: Göller Verlag; 2017. p. 454

[7] Yurkov A. Refractories for Aluminum: Electrolysis and the Cast House. 2nd ed. Springer International Publishing AG; 2017

[8] ASTM. C768-99 Standard Practice for Drip Slag Testing Refractory Materials at High Temperature. 2004

[9] DIN 51069-2. Testing of ceramic materials; comparing test of the resistance of refractory bricks to the attack of solid and liquid materials at high temperature, crucible method. 1972

[10] ISO 20292. Materials for the production of primary aluminium — Dense refractory bricks — Determination of cryolite resistance. 2009

[11] DIN CEN/TS 15418:2006-09. Methods of test for dense refractory products – Guidelines for testing the corrosion of refractories caused by liquids. 2006

[12] Quirmbach P. Laboratory testing methods up to 1600°C. In: Corrosion of Refractories: Testing and Characterization Methods. Baden-Baden: Göller-Verlag. pp. 1-22

[13] Skybakmoen E, Kvello J, Darrel O, Gudbransen H. Test and analysis of nitride bonded SiC sidelining materials: Typical properties analysed 1997-2007. Light Metals. 2008;**137**:943-948

[14] Drew C. Metallurgical and materials transactions B cup test. 2007

[15] Yurkov A, Malakho A, Avdeev V. Corrosion behavior of silicon nitride bonded silicon carbide refractory material by molten copper and copper slag. Ceramics International. 2017;**43**:4241-4245

Section 2

Copper Applications

Chapter 4

Metallic Copper as Dehalogenation Catalyst in the Treatment of Water and Wastewaters

Ali Shee and Katrin Mackenzie

Abstract

Most halogenated organic compounds (HOCs) are toxic and carcinogenic, hence unwanted in the environment. Several technologies exist for the treatment of both legacy and newly contaminated zones. In many contaminated subsurface environments, nano zero-valent iron (nZVI) as a reagent is the tool of choice, while palladium (Pd) as a catalyst faces technical challenges. A system comprising metallic copper and borohydride as a reducing agent (referred herein as copper-borohydride system, CBHS) provides an alternative to nZVI and Pd. This chapter presents a deeper understanding of the CBHS for the treatment of HOCs by highlighting the state of knowledge related to the i) type and classes of compounds that are treatable, ii) possible reaction pathways for their transformation, iii) specific metal activities for transformation of selected classes of HOCs, iv) influence of common water constituents on catalyst stability, and v) future perspectives regarding its application in water treatment applications. Furthermore, an up-to-date discussion is presented regarding the available techniques for the synthesis of copper nanoparticles. Based on the evaluation criteria including product selectivity patterns, amount and the fate of intermediates, and metal cost and stabilities in water, the most suitable application areas for Cu, Pd, and nZVI are presented as recommendations.

1. Introduction

Environmental contamination of soil, surface water, and groundwater with halogenated organic compounds (HOCs) continues to pose a serious threat to both human and ecological health. HOCs are indispensable in many consumer products and industrial processes, e.g. as solvents, refrigerants, and feedstocks in the manufacture of pharmaceuticals, veterinary drugs, paints, adhesives, and lacquers [1]. HOCs commonly enter the environment by improper use. That includes accidental discharge from the chemical industries, surface runoff, and improper disposal and usage. The low-molecular-weight HOCs including haloacetic acids and halomethanes are also prominent members of disinfection byproducts which are produced when natural

waters containing organic matter are treated with chlorine and chlorine-based disinfectants [2]. Chlorinated compounds become more and more insoluble in water with growing carbon chain length of 10–13 and higher chlorine content which also makes them susceptible to long-range atmospheric transport [3]. In aquatic environments, such substances undergo bioaccumulation and biomagnification in aquatic organisms, e.g. fish, crabs, oysters, etc.; thus, they enter the food chain [3–5]. In addition, human exposure to HOCs occurs via dermal absorption, inhalation, and drinking contaminated water and consumption of contaminated food [1]. Most HOCs are also toxic and possible carcinogens even at very low concentrations [6–8]. Due to their associated public health risks, the production and use of HOCs is under strict control. Many of them are placed under the Stockholm Convention on Persistent Organic Pollutants and are also placed on toxic release inventory in the European Union, Japan, Canada, and the United States [1, 3–5]. When released into the environment, most HOCs are resistant to biodegradation; hence, they are persistent. The removal of HOCs from contaminated environments is therefore of utmost importance. Several technological processes based on biological, physical, and chemical methods have been evaluated for various contaminant types. So far, there is no single technology that can be applied for the detoxification of all contamination problems. Important factors which need to be considered before selecting a treatment technology include the chemical nature of the HOCs, the nature of contaminated media, the extent of contamination, overall treatment time, cost of the treatment system, degree of detoxification, and fate of the treated media.

Biological processes in most cases are characterized by low conversion degrees of the contaminant and slow reaction rates but low maintenance. Hence, long treatment times are necessary for bringing the contaminants concentrations to levels of low toxicity. Also, microbial processes such as methanogenesis are sometimes inhibited by the presence of high concentrations of some target contaminants, e.g. chloroform (CF) [9, 10]. Air-stripping and adsorption processes for removal of HOCs from water only transfer the contaminants from one phase into another, where further treatment of the resultant effluents is necessary [11]. For adsorption processes, regeneration of the adsorber (e.g. activated carbon) or its frequent replacement is not only expensive but also time-consuming. Incineration which is sometimes applied to more complex and toxic industrial effluents is energy-intensive and costly. The major environmental problem associated with incineration of HOCs include the release of incomplete combustion products, fly ash generation, and particularly the generation of toxic byproducts, especially polychlorinated dibenzo-p-dioxins and dibenzofurans (PCDD/Fs), polychlorinated biphenyls (PCBs), and polychlorinated naphthalenes (PCNs) [12, 13].

Chemical destruction techniques based on photooxidation, Fenton's reagent, and advanced oxidation processes (AOPs) when applied to HOCs are characterized by low reaction selectivity and a higher probability of generating toxic and recalcitrant byproducts. Hence, the provision of excess redox equivalents is necessary when full mineralization is desired [14, 15]. Reduction processes are more suited for the treatment of HOCs than oxidation processes. Reduction involves the selective removal of the halogen (X) atoms by H-atoms (R–X + reducing agent → R–H + H–X). Generally, the replacement of X atoms from higher halogenated contaminants results in significant detoxifications. However, there are exceptions. A prominent example is vinyl chloride (VC), which is more toxic than the higher chlorinated chloroethene homologs, e.g. perchloroethylene (PCE) [16]. The coupling of reduction processes with biological processes can sometimes be used to achieve significant detoxification [17, 18].

For about three decades (since 1994) [19], technologies employing microscale zero-valent iron (mZVI) or nano zero-valent iron (nZVI) as reagents to reduce HOCs were

the methods of choice for *in situ* groundwater treatment of HOCs [20, 21]. Due to the higher HOCs reaction rates and better particle mobility, nZVI is widely used for direct injection into the aquifer. In the presence of water, nZVI as a reagent is consumed, thereby releasing electrons (and consecutively also hydrogen) that are essential for the cleavage of the R–X bond ($R-X + Fe^0 + H_2O \rightarrow R-H + Fe^{2+} + X^- + OH^-$). Reducing agents based on metallic iron are comparably cheap, environmentally compatible, and offers long-term treatment solutions for contaminated aquifers under anaerobic conditions. nZVI can be applied to treat mainly the halogenated alkanes and alkenes. It shows very low activity for the reduction of saturated aliphatic compounds with lower chlorination degrees such as dichloromethane (DCM) and 1,2-dichloroethane (1,2-DCA) [22, 23]. Also, iron's limitations are its inability to reduce C–Cl bonds attached to aromatic structures, especially those with lower chlorination degrees [24, 25], its tendency to deactivate under aerobic conditions, its loss of activity at pH > 10, and its consumption with time by anaerobic corrosion in water ($Fe^0 + 2H_2O \rightarrow Fe^{2+} + H_2 + 2OH^-$). The consumption of nZVI in water due to corrosion is pH-sensitive. When pH < 7 is applied, nZVI is consumed quickly producing hydrogen as the major product. At pH > 10, the coating of nZVI core with iron oxides/hydroxides occurs inhibiting further reaction. Hence for the reduction of HOCs in water by nZVI, the pH need to be maintained in the range 7–10 using suitable buffers [26].

Reduction processes catalyzed by H-activating metals, especially rhodium (Rh), platinum (Pt), and Pd, are applicable to treat a broader spectrum of compounds which include the reduction of C–X bonds attached to aromatic structures. Among the noble metals, Pd is the most potent hydrodehalogenation (HDH) catalyst. However, Pd is sensitive to deactivation due to poisoning and even self-poisoning by released hydrogen halide (HX). Nevertheless, the effect of HX can be prevented by its withdrawal from the surface through uptake by the water bulk phase or by the addition of a base, e.g. NaOH [27–30]. Whereas nZVI does not require the addition of an additional reductant, Pd must be used together with H-donors (reducing agents) such as H_2, borohydride (BH_4^-), Fe^0 as H_2 producer, formic acid, hydrazine, or alike [31, 32]. The HDH reaction occurs at Pd surfaces and is mediated by activated H-species (H^*) or adsorbed surface hydrogen ($Pd-H_{ads}$) [33–35]. The cleavage of R–X bonds by Pd catalyst and in the presence of hydrogen as the reductant can be described as ($R-X + H_2 + Pd^0 \rightarrow R-H + HX + Pd^0$). The specific metal activity (A_m), which will be discussed later in this chapter, can be used to formally compare the treatment efficiencies of reagents and catalysts. A_m is a second-order parameter that tells us the amount of metal required to treat a given amount of contaminated water per time (required number of half-lives until desired treatment goal is reached). For similar compounds and under comparable reaction conditions, the specific Pd activity (A_{Pd}) seems to depend on the nature of H-donors [32]. Nevertheless, for all HOCs classes, A_{Pd} is found to be between two and five orders of magnitude higher than the specific nZVI activity (A_{nZVI}) [36, 37]. Pd as a catalyst is reusable several times and is required only in very small amounts. Therefore, in comparison with nZVI, only a small amount of Pd metal is necessary to treat large volumes of contaminated water in very short times. Another advantage of Pd compared to nZVI is that it can be applied over a broad range of pH (2–9) and to nearly all HOCs classes including the reduction of chlorinated aromatics [38, 39]. In comparison with nZVI, the application of Pd for the reduction of HOCs in water is not limited by pH. Nevertheless, dissolution of Pd metal under highly acidic conditions can occur [40].

Despite the huge potential of Pd in HDH reactions, its use in water treatment applications under field conditions is limited due to major drawbacks. Pd is more

expensive and rarer than nZVI and is readily deactivated by manifold processes which inhibit or even destroy the catalyst function. The Pd catalyst loses its activity in the presence of macromolecular and ionic poisons such as heavy metals, organic matter (e.g. natural organic matter (NOM), humic acids (HA), and fulvic acids) [40–44]. The most significant substances with a detrimental effect on Pd are reduced sulfur compounds (RSCs), e.g. SO_3^{2-} and S^{2-} [45]. Under anaerobic conditions, S^{2-} can also be produced in aqueous environments by sulfate-reducing bacteria, especially in the presence of hydrogen. Regeneration of deactivated Pd catalysts using oxidants, e.g. hypochlorite is tedious, expensive, and time-consuming, results in loss of metal due to leaching and may not restore original (baseline) catalyst activity [40, 41, 44]. Also, A_{Pd} values are extremely low for saturated aliphatic compounds with lower chlorination degrees such as dichloromethane (DCM) and 1,2-dichloroethane (1,2-DCA) [22, 23, 38, 39]. DCM, 1,2-DCA, and similar compounds are contaminants of interest to water treatment professionals, since they are toxic and possible carcinogens. Saturated aliphatic compounds with lower chlorination degrees such as chloromethane (CM), DCM, and chloroethane (CA) are also produced as stable byproducts during the dechlorination of the corresponding higher chlorinated homologs. For example, the dechlorination of CF and carbon tetrachloride (CTC) by nZVI and Pd produces CM and DCM as recalcitrant byproducts [22, 38, 46, 47]. Similarly, CA is usually a dead-end byproduct during the dechlorination of 1,1,1-trichloroethane (1,1,1-TCA) by nZVI and Pd [23, 38].

Cu is the eighth most abundant element of the earth's crust, and its unique properties such as good ductility, malleability, high thermal and electrical conductivity, and high corrosion resistance make it suitable for a broad range of applications. Common applications for metallic Cu catalysts include oxidative degradation of HOCs [48], NOx reduction [49], CO_2 reduction [50], electrocatalytic reduction of chlorinated alkanes [51–53], and aryl coupling reactions [54, 55]. Despite this widespread application, the utilization of metallic Cu as reduction catalysts for the treatment of HOCs in water is limited. Under ambient conditions (1 atm and 25°C) and in water, metallic Cu is less reactive toward the activation of H_2 into H^*. Hence, it must be used together with a more reactive reductant such as BH_4^- ($E° = -1.24$ V vs. standard hydrogen electrode (SHE)) [56]. In this chapter, CHBS represents $Cu + BH_4^-$. The HDH reaction by the copper-borohydride system (CBHS) may be mediated by several reactive species. The cleavage of R–X bonds could be mediated by surface adsorbed H-species or hydrides [57–59]. Like in hydrosilylation reactions, the insertion of Cu species may as well be implicated [60, 61]. In this chapter, we review important literature to provide a deeper understanding of the CBHS for the reductive treatment of HOCs in water. Consideration will focus on product selectivity patterns, specific Cu activities (A_{Cu}), and catalyst stability in water. For a broad spectrum of HOCs, the HDH ability of the CBHS is compared with the common reduction tools based on nZVI and Pd. The comparison is intended to provide a guide to water treatment professionals during the decision-making process in selecting an appropriate tool that is best suited to a particular class of HOCs under certain reaction conditions. In order to do the comparison, several essential criteria are defined in this chapter.

2. Evaluation criteria for reagents and catalysts

The evaluation of the efficiency of a treatment system involves several parameters which are discussed in this section. Conversion (X_{HOC}) which shows the fraction of a given contaminant transformed at any given time can be calculated using Eq. (1):

$$X_{\text{HOC}} = \left(1 - \frac{n_{\text{HOC,t}}}{n_{\text{HOC,0}}}\right) \times 100\% \qquad (1)$$

where $n_{\text{HOC,t}}$ represents the moles of educt at any given time (mol) and $n_{\text{HOC,0}}$ refers to the initial moles of educt fed into the batch reactor at t = 0 (mol). The product yield ($Y_{\text{i,product}}$) which shows the amount of product formed with respect to the initial moles of educt fed into the reactor is calculated based on Eq. (2):

$$Y_{\text{i,product}} = \frac{n_{\text{i,product}}}{n_{\text{HOC,0}}} \times 100\% \qquad (2)$$

where $n_{\text{i,product}}$ represents the moles of product i obtained at a given time (mol). In order to determine the actual amount of product formed with respect to the actual amount of educt transformed at any given time, product selectivity ($S_{\text{i,product}}$) can be calculated based on Eq. (3):

$$S_{\text{i,product}} = \frac{n_{\text{i,product}}}{n_{\text{converted HOC}}} \times 100\% \qquad (3)$$

where $n_{\text{converted,HOC}}$ represents the moles of educt converted at the given time (mol). In order to determine the reaction rates for the transformation of HOCs using nZVI, Pd, and Cu, the pseudo-first-order kinetics as shown in Eq. (4) can be applied:

$$\frac{dc_{\text{i}}}{dt} = -k_{\text{obs}} \cdot c_{\text{i}} \qquad (4)$$

where c_{i} represents the concentration of HOCs (mg/L), while k_{obs} is the pseudo-first-order rate constant (1/min). For slow-reacting compounds, such as CA, that are characterized by lower conversion degrees, k_{obs} can conveniently be calculated from products formation as shown in Eq. (5):

$$In\left(1 - \frac{c_{\text{i,product}}}{c_{\text{product, max}}}\right) = -k_{\text{obs}} \cdot t \qquad (5)$$

where $c_{\text{i,product}}$ and $c_{\text{product,max}}$ represent the concentration of product at the given time (mg/L) and the maximum concentration of product (mg/L), respectively, while t refers to the reaction time (min). The value of k_{obs} calculated based on Eq. (4) and Eq. (5) and for metal particles with similar particle sizes can be used to compare the HDH ability of a remediation tool only for HOCs transformation reactions carried out under similar reaction conditions (same metal concentrations and reaction pH). Since in most cases reaction conditions are hardly the same, the surface area-normalized rate constant (k_{SA} in [L/(m^2·min)]) that is calculated based on Eq. (6) can be used:

$$k_{\text{SA}} = \frac{k_{\text{obs}}}{c_{\text{m}} \cdot a_{\text{s}}} \qquad (6)$$

where c_{m} is the concentration of the metal (g/L) and a_{s} is the metal-specific surface area (m^2/g). The value of a_{s} is commonly obtained from N$_2$ adsorption/desorption (Brunauer–Emmett–Teller (BET)) measurements. The use of k_{SA} assumes that the entire exposed surface area of the metal participates in the reaction. Based on this understanding, nanosized particles which have larger available surface areas are

preferred for HDH reactions compared to their micro-sized particles. However, it is noteworthy to point out that for heterogeneous systems, only a fraction of the available surface area takes part in the HDH reaction. Specifically, only the available surface atoms as determined by dispersion data (from CO chemisorption measurements) are involved. In the absence of metal dispersion data, the specific metal activity (A_m) which is calculated as shown in Eq. (7) can be used:

$$A_m = \frac{V_w}{m \cdot \tau_{\frac{1}{2}}} = \frac{1}{c_m \cdot \tau_{\frac{1}{2}}} = \frac{\ln(c_{t1}/c_{t2})}{\ln 2 \cdot c_m (t_2 - t_1)} = \frac{k_{obs}}{\ln 2 \cdot c_m} \; [\text{L}/(\text{g} \cdot \text{min})] \qquad (7)$$

where V_w is the volume of the water contaminated with HOCs (L), m refers to the metal mass (g), and $\tau_{\frac{1}{2}}$ refers to the HOCs half-life (min) obtained from the pseudo-first-order kinetics profile. The variables c_{t1} and c_{t2} refer to the concentrations of contaminants at any two sampling times t_1 and t_2, respectively. A_m can be used for different metals which have nearly the same particle sizes to provide a solid comparison where dispersion data is not available. In terms of technical and economical points of view, A_m shows the amount of metal required to treat a given volume of contaminated water in several half-lives. By using A_m as a basis for comparing the dehalogenation abilities of nZVI, Pd, and Cu, it is important to point out that we are comparing three "reduction systems" and not the metals, because different reductants are applied (BH_4^-, H_2, and Fe^0).

3. Synthesis strategies for copper nanoparticles (Cu NPs)

The synthesis of Cu nanoparticles (Cu NPs) can be done by using physical, bio-based, and chemical methods. Top-down or physical methods are used to reduce bulk material into nanosized dimensions by mechanical milling, grinding, cutting, etching, laser ablation, vacuum vapor deposition, and pulsed wire discharge [62, 63]. Top-down methods are less preferred; since it is difficult to obtain Cu NPs with uniform sizes, they are energy-intensive and require specialized equipment and technical knowledge.

Bio-based methods for the synthesis of Cu NPs employ the use of plant extracts and microorganisms. Cu NPs can be produced by heating a mixture of plant extracts and copper salts. The reducing and stabilizing agents present in plant extracts include phenols, flavonoids, proteins, tannins, and terpenoids. Common microorganisms used include bacteria, fungi, and green algae [64, 65]. Bio-based methods are preferred because they are considered cost-effective and environmentally friendly. For the rapid and large-scale synthesis of Cu NPs, chemical reduction techniques are preferred over biological methods.

Bottom-up approaches involve the synthesis of Cu NPs from a copper salt or copper oxide. Common bottom-up methods applied include chemical reduction, sonochemical reduction, micro-emulsion techniques, electrochemical reduction, hydrothermal or sol–gel synthesis, polyol, and microwave irradiation [62, 63]. Chemical reduction techniques for the synthesis of Cu NPs are the most common, since they are simple and usually have the tendency to produce smaller and uniform nanoparticles. Furthermore, in chemical reduction methods, nanoparticles of desired sizes and morphology can be obtained by manipulation of reaction conditions, e.g. time, pH, solvent, and suspension stabilizer. The reduction of a copper salt can be done using reductants such as BH_4^- and hydrazine combined with stabilizers

including ascorbic acid, starch, poly(ethylene glycol), poly(vinylpyrrolidone) (PVP), cetyltrimethylammonium bromide, poly(acrylic acid) (PAA), and carboxymethyl cellulose (CMC). When stabilizers are used, the reaction mixture needs to be refluxed at 60–100°C for about 30–120 min.

The most widely used method for the synthesis of Cu NPs in water and under ambient conditions involves the reduction of a copper precursor with sodium borohydride ($NaBH_4$). This method is preferred, since it is simple to implement and produces nanoparticles with uniform sizes, narrow size distribution range, and uniform surface morphology [66, 67]. Under ambient conditions and in water, BH_4^- is unstable and the decomposition rate is pH-sensitive [58, 68, 69]. Therefore, to control BH_4^- decomposition, reaction pH $\geq$ 10 is ideal for the growth and development of Cu NPs. The recommended molar ratio for Cu^{2+} : $NaBH_4$ is 1 : 8. A lower molar ratio between Cu^{2+} and $NaBH_4$ is characterized by a slower reaction and nonuniform particle sizes. To prevent agglomeration of the freshly prepared nanoparticles, the stabilizers (PVP, PAA, CMC, etc.) are usually introduced already during the synthesis process.

4. Reduction of HOCs in water: Comparison of Cu, Pd, and nZVI

The CBHS for reduction of HOCs in water has received less attention than with Pd + H_2 and nZVI. Previous work applied the CBHS for dechlorination of DCM [66], 1,2-DCA [67], and selected monochloroaromatics [70]. Recently, a deeper understanding of the system was applied to a broad spectrum of HOCs, highlighting product selectivity patterns, reaction rates of the individual compounds, and the efficiency of the system in comparison with Pd and nZVI [36, 37]. The HDH ability of the CBHS for the treatment of saturated aliphatic HOCs is markedly superior to nZVI and Pd. This section provides an extensive overview of the HDH abilities of the three systems. Evaluation criteria include reduction (dehalogenation) rates of individual HOCs, product selectivity patterns, amount and fate of chlorinated intermediates, metal cost, and metal stability in water. It is noteworthy to point out this is not a comparison of the individual metals but rather a comparison of their reduction abilities (Cu + BH_4^-, Pd + H_2, and nZVI). Using both experimental and literature data, Shee (2021) calculated the specific metal activities for the reduction of individual HOCs in water using Cu, Pd, and nZVI as shown in **Table 1**. The data in **Table 1** were calculated using nanoparticles of comparable dimensions ($d_{50,Cu}$ = 50 nm, $d_{50,Pd}$ = 60 nm, and $d_{50,nZVI}$ = 75 nm) [36].

From the data in **Table 1**, for most compounds, the ease of dehalogenation is based on the weakest C–X bond strengths.

Since C–Br (285 kJ/mol) are weaker than C–Cl bonds (337 kJ/mol), brominated compounds show higher A_m values than their chlorinated counterparts. As can be seen in **Table 1**, for Cu, the dehalogenation rates (presented as A_{Cu}) for halogenated methanes and ethanes depend on i) the strength of the weakest C–X bond and ii) the number of geminal X atoms. The A_{Cu} values are generally inversely proportional to the strength of the calculated C–X bonds. For example, $A_{Cu,CTC}$ is five orders of magnitude higher than $A_{Cu,DCM}$. For the chlorinated ethanes, their reactivity depends not only on the number of Cl atoms but also on the number of geminal Cl atoms. An increase in the number of geminal Cl atoms leads to i) a decrease in C–Cl bond strengths and ii) an increase in the initial attachment of Cl atoms to the catalyst surface. This trend in reactivity for chlorinated methanes and ethanes was also observed for reactions carried out in the gas phase using solid metallic Cu [71] and Pd

Halogenated organic compound classes		BDE (kJ/mol)	Specific metal activities A_m [L/(g·min)]		
			m = Cu	m = Pd	m = nZVI
Chlorinated methanes and ethanes with higher chlorination degree	CTC	293	1100 ± 100	200 ± 20	0.30 ± 0.05
	CF	322	130 ± 10	5 ± 1	0.003 ± 0.001
	1,1,1-TCA	309	170 ± 20	n.a.	0.102 ± 0.006
	1,1,2-trichloroethane	318	6 ± 1	1.3 ± 0.2	0.0016 ± 0.0002
	1,1,1,2-tetrachloroethane	295	900 ± 200	380 ± 20	0.36 ± 0.03
	1,1,2,2-tetrachloroethane	314	60 ± 5	n.a.	0.021 ± 0.003
	Hexachloroethane	304	2500 ± 500	n.a.	0.52 ± 0.04
Chlorinated methanes and ethanes with lower chlorination degree	DCM	339	0.22 ± 0.02	n.a.	n.a.
	CM	351	0.0020 ± 0.0002	n.a.	n.a.
	CA	352	0.010 ± 0.005	n.a.	n.a.
	1,1-dichloroethane	328	5 ± 1	3 ± 1	0.000014 ± 0.000003
	1,2-DCA	345	0.10 ± 0.04	0.0010 ± 0.0005	< 0.000003
	1,2-dichloropropane	319	0.40 ± 0.08	0.006 ± 0.001	n.a.
	1,2,3-trichlopropane	n.a.	0.30 ± 0.01	0.007 ± 0.002	n.a.
	1,2-dichlorobutane	n.a.	0.50 ± 0.03	0.004 ± 0.002	n.a.
Brominated compounds	Bromotrichloromethane,	231	1300 ± 100	n.a.	n.a.
	Bromoform	275	2000 ± 300	300 ± 50	0.060 ± 0.005
	Dibromomethane	276	390 ± 20	40 ± 10	0.03 ± 0.01
	Bromomethane	294	20 ± 3	n.a.	n.a.
	Vinyl bromide	338	67 ± 10	2500 ± 500	0.0028 ± 0.0002

Halogenated organic compound classes		BDE (kJ/mol)	Specific metal activities A_m [L/(g·min)]		
			m = Cu	m = Pd	m = nZVI
Chlorinated ethenes	VC	452	4 ± 2	1600 ± 200	n.a.
	1,1-dichloroethene (1,1-DCE)	394[d]	10 ± 1	590 ± 50	n.a.
	trans-DCE (*t*-DCE)	373	17 ± 5	1200 ± 100	n.a.
	cis-DCE (*c*-DCE)	370	5 ± 2	840 ± 60	n.a.
	Trichloroethene (TCE)	392	17 ± 1	220 ± 50	0.00024 ± 0.00004
	PCE	382	3 ± 1	110 ± 10	0.00040 ± 0.00022
Halogenated aromatic compounds	Chlorobenzene (CB)	399	0.00004 ± 0.00001	500 ± 150	n.a.
	Bromobenzene (BB)	337	80 ± 10	900 ± 100	n.a.

Table 1.
Calculated specific metal activities for the dehalogenation of single HOCs in water using Cu-, Pd-, and nZVI-based systems and the corresponding weakest C–X bond dissociation energies.

[72, 73]. The correlation between reactivity and the weakest C–X bond strength shows that the HDH reactions at Cu and Pd surfaces for saturated aliphatic HOCs follow similar reaction mechanisms. Hence, the cleavage of the C–X bond is rate-determining and involves homolytic cleavage of the weakest C–X bond (R–X → R· + X·). It is also important to point out that the adsorption strengths of X atoms at the catalyst surface are essential for bond cleavage. During aqueous phase hydrodechlorination (HDC) of CTC and CF by Cu and Pd, radical coupling byproducts such as ethane and ethene [37, 46] were detected in trace amounts. Homolytic cleavage of CF and CTC to form dichloromethyl and trichloromethyl radicals, respectively, is therefore rate-determining. Radical coupling reactions are only minor. The radical intermediates undergo further reactions to form various products, e.g. methane (CH_4), CM, and DCM [22, 37].

In environmental catalysis, the proportion of the fully dechlorinated product with respect to the chlorinated intermediates, i.e. selectivity, is essential in evaluating the efficiency of a treatment system. By using compounds with the general formula CCl_3–R where R = H, F, Cl, Br, and CH_3, the CBHS was applied to evaluate product selectivity patterns [37]. By using CF (where R = H) as a model compound, it was found that for both Cu and Pd, the selectivity to DCM was 10–15 mol-%. Further assessment of the ratio of specific metal activities for dechlorination of CF and DCM using Cu and Pd, $A_{Cu,CF}/A_{Cu,DCM}$ = 591 and $A_{Pd,CF}/A_{Pd,DCM}$ = 531, respectively, show that both systems have a problem with DCM formation. In the same study, it was reported that for nZVI, CM and DCM selectivities were 30–40 mol-% and 35–45 mol-%, respectively, and A_{nZVI} = 0.003 ± 0.001 L/(g·min). Further assessment of the CBHS showed that variation in reaction conditions, e.g. catalyst amount, type, and concentration of reductants and catalysts support, had no significant effect on DCM selectivity. A multi-catalytic approach was essential in changing DCM selectivity. DCM selectivity was decreased by more than 80% by combining the CBHS with either silver (Ag) or vitamin B_{12}. Whereas CM and DCM remain more-or-less as dead-end byproducts when Pd and nZVI are used for the dechlorination of CF and CTC, the CBHS readily dechlorinates these compounds in subsequent steps [37]. This ability of CBHS to dechlorinate DCM and similar compounds (see **Table 1**) makes it more appropriate for the treatment of saturated aliphatic HOCs. Therefore, metallic Cu can be considered the "agent of choice" for the treatment of these classes of compounds in highly contaminated wastewaters.

Similar to the halogenated methanes and ethanes, brominated ethenes are more easily transformed than their chlorinated counterparts (see **Table 1**). This could be attributed at least to the strength of the C–Br and C–Cl bonds. However, the HDC mechanism for chlorinated ethenes is not as straightforward as that of the chlorinated methanes and ethanes. Both Mackenzie et al. (2006) and Shee (2021) have demonstrated that the HDC rates for chlorinated ethenes are independent of the C–Cl bond strengths. For chlorinated ethenes, two reaction steps are involved: i) cleavage of the C–Cl bond and ii) hydrogenation of the double bond. Mackenzie et al. (2006) have shown that the rate-determining step for HDC of chlorinated ethenes by Pd is a concerted step involving the addition of H* to the double bond and simultaneous cleavage of the C–X bond. The hydrogenation of the double bond occurs later after the cleavage of the C–X bond. For compounds containing pi-systems, the essential step is C=C di-δ bond formation at the catalyst surface (active centers) [39, 74, 75]. However, it is important to point out that in addition to C=C di-δ bonding, the Cl atoms also interact with the catalyst surface. Hence, dissociative adsorption of the C–Cl bonds followed by hydrogenation of C=C bonds are characteristic reaction steps for

chlorinated ethenes. Based on this description, Pd as a potent hydrogenation catalyst smoothly dechlorinates chlorinated ethenes. For all halogenated ethenes (see **Table 1**), A_{Pd} increases with increasing C–Cl bond strengths. Hence, the order of reactivity for Pd is VC > DCE isomers > TCE > PCE. In general, A_{Pd} values for all compounds (see **Table 1**) are two to three orders of magnitude than A_{Cu} values. For the CBHS, there is no clear distinction in the reactivity of the chlorinated ethenes. The A_{Cu} values differ only by one order of magnitude which is less significant. Therefore, in the HDC of chlorinated ethenes by the CBHS, we suggest that the lower A_{Cu} values could be due to i) minimal interaction of the C=C bond with the metallic Cu surface for di-δ bonding, and ii) the actual reductants could be adsorbed hydride species (Cu–H) instead of H* that are predominant in Pd. Although the A_{nZVI} values for reduction of halogenated ethenes are five to eight orders of magnitude lower than A_{Cu} and A_{Pd}, it can be considered the "agent of choice" for *in situ* treatment of the highly chlorinated homologs, PCE and TCE. Fe is abundant in nature; it is cheaper than both Pd and Cu; it is environmentally compatible and does not require the addition of a reductant. Furthermore, the formation of an oxidic layer that protects the metallic nZVI core offers a long-term treatment solution for contaminated plumes and groundwater. Since the transformation of TCE and PCE results to accumulation of VC and the DCE isomers with time, coupling nZVI with microbial processes can achieve significant detoxification. However, for the treatment of chlorinated ethenes derived from industrial processes where rapid detoxification is desired, Cu catalysts are in such cases more appropriate than nZVI.

Other than halogenated alkanes and alkenes, halogenated aromatic compounds (HACs) are also a significant class of environmental contaminants. These compounds are more hydrophobic than the corresponding aliphatic HOCs. In the presence of organic matter, HACs are strongly immobilized in soil compartments and sediments [76, 77]. Hence before treatment, the HACs need to be desorbed using solvents and surfactants. *Ex situ* treatment technologies such as soil washing and pump and treat need to consider that the extraction solvent constitutes a cocktail of HACs, solutes, heavy metals, and organic matter. Most of the matrix components are catalysts inhibitors, and therefore pretreatment steps such as coagulation, flocculation, and filtration need to be considered. For the CBHS, Shee (2021) has demonstrated that Cu is rather resistant to deactivation by most water matrix constituents including S^{2-} and SO_3^{2-}. In contrast, Pd is known to undergo either partial or permanent deactivation in the presence of several solutes from soil washing processes. RSCs are the most dangerous poisons whose presence even in trace levels leads to permanent catalyst deactivation [40, 42, 44, 45, 78]. In order to prolong Pd activity, several protection steps have been investigated with little success. These include i) pretreatment steps such as coagulation, flocculation, sedimentation, and filtration steps to precipitate heavy metals and organic macromolecules, ii) addition of oxidants to convert RSCs into non-deactivating substances, e.g. SO_4^{2-} [78], iii) regeneration of the fouled catalysts by the addition of oxidants such as $KMNO_4$, H_2O_2, and hypochlorite, and iv) minimizing contact between the poisons and catalysts by introducing a protective layer of adsorbent, e.g. zeolites, silica material, and poly(dimethylsiloxane) (PDMS) [40, 79–81].

In addition to water matrix composition, the reaction rates of the individual HACs are important in selecting the appropriate reduction system. Numerous literature studies show that unmodified nZVI is able to dechlorinate chlorobenzene (CB) and dichlorodiphenyltrichloroethane (DDT) [82–84]. However, these studies are subject to debate. nZVI is an electron-transmitting reagent, and the transfer of an electron leading to cleavage of the weakest C–X bond is rate-controlling. For HACs, the

cleavage of the C–X bond involves at least two important steps [85] which are described in Eq. (8) and Eq. (9).

i. Formation of a radical anion as a true intermediate after the first electron transfer step:

$$(ArX + e \rightarrow [ArX])\qquad(8)$$

ii. Formation of an aryl radical and halide anion:

$$([ArX]^- \cdot \rightarrow Ar \cdot + X^-)\qquad(9)$$

If the first step is essential and therefore rate-controlling, then the electron affinity of the substrate is an important consideration. Thus, CB (E_A = −0.14 eV) is less reactive than hexachlorobenzene ((HCB) with E_A = +0.94 eV). Since the electron transfer process (Eq. (8)) occurs with much difficulty, unmodified nZVI is not suitable for the reduction of aromatic C–Cl bonds attached to aromatic structures [24, 25]. Both Cu and Pd are able to reduce C–Br and C–Cl bonds attached to aromatic structures, and the reaction rates are substance- and system-specific. Under similar reaction conditions and for nanoparticles with comparable sizes, Shee (2021) determined that the A_{Cu} for dehalogenation of CB and BB were ($A_{Cu,CB}$ = (4 ± 1) × 10^{-5} L/(g·min)) and ($A_{Cu,BB}$ = (8 ± 1) × 10^1 L/(g·min)), respectively. In the same study, Pd activities were the highest where $A_{Pd,CB}$ = (5 ± 1.5) × 10^2 L/(g·min) and $A_{Pd,BB}$ = (9 ± 1) × 10^2 L/(g·min). Therefore, Cu which is cheaper and stable in water can be applied as the "agent of choice" for the treatment of brominated aromatic compounds. The niche application of protected Pd catalyst is seen only in *ex situ* treatment of chlorinated aromatics such as in soil washing and pump and treat technologies.

5. Future perspectives and application areas of the CBHS

The CBHS has shown potential for use in water treatment technologies for a broad range of compounds. However, the technology is still in its initial stages, and there are still some aspects that need further investigation. First, the possible reductants either hydrides or H* need to be clarified in order to explain the difference in reactivity between halogenated alkanes and alkenes.

Since BH_4^- is used as a reductant, clarification on the exact number of H-atoms (hence electrons) transferred to the contaminant is essential. This clarification is needed for the evaluation of reductant costs. Based on reduction equivalents and unit prices of the reductants, it was estimated that $NaBH_4$ costs more than H_2 by at least a factor of 12 [36].

The comparison of the HDH ability of Cu and Pd has been investigated using two different reductants and in the aqueous phase where a layer of the solvent is introduced around the metal particles. Although nanosized particles were applied and the batch reactors were continuously shaken, mass transfer limitations especially for fast-reacting substances need consideration. For better comparison, we suggest experiments carried out under similar elevated temperature conditions, and that H_2 is used as a reductant. The HDH reactions are then conducted in the gaseous phase at hot solid metal catalysts (Cu and Pd).

Another challenge is connected with effluents at pH values between 9 and 10 when BH_4^- is applied as a reductant, as well as the formation of the undesired borates and boric acid [36]. Removal of boric acid and borates may be necessary before the effluent is discharged.

Trace amounts of Cu are essential for the functioning of various biological processes in humans, plants, and animals. Nevertheless, higher Cu doses are toxic [86]. Therefore, the leaching of Cu into the environment must be controlled. Simple iron beds are effective police filters. Embedding Cu onto cation-exchange resins was also seen to minimize Cu leaching after repeated reaction cycles [36, 87]. Amberlite IRP 69 as support for Cu does not only offer partial protection of the catalysts against S^{2-} but also enables regeneration of the deactivated catalyst simply by washing with water [36]. Apart from cation-exchange resins, other adsorbents such as zeolites may be investigated. The speciation of Cu within these adsorbents and the role of the support on catalyst performance are possible topics for further research. Since contact between the embedded Cu and BH_4^- may not be possible, it is also necessary to identify the nature of reducing species that facilitate the HDH reaction.

6. Conclusions

This chapter shows that CBHS although has received less attention should be considered as an alternative tool to nZVI and Pd in water treatment applications. The high potential of the CBHS is seen in the *in situ* regeneration of HOCs-loaded adsorbents in small-scale treatment plants. For detoxification of contaminated soils, preliminary processes including soil washing, filtration, adsorption, and desorption should be implemented in the initial stages to transfer immobilized HOCs into an aqueous media. The CBHS can then be added into the HOCs concentrated aqueous media for detoxification.

Acknowledgements

Conflict of interest

The authors declare no conflict of interest.

Author details

Ali Shee and Katrin Mackenzie*
Department of Environmental Engineering, Helmholtz Centre for Environmental Research - UFZ, Leipzig, Germany

*Address all correspondence to: katrin.mackenzie@ufz.de

IntechOpen

References

[1] Huang B, Lei C, Wei C, Zeng G. Chlorinated volatile organic compounds (Cl-VOCs) in environment — sources, potential human health impacts, and current remediation technologies. Environment International. 2014;**71**: 118-138

[2] Richardson SD, Postigo C. Drinking water disinfection by-products. In: Barceló D, editor. Emerging Organic Contaminants and Human Health. Heidelberg: Springer Berlin Heidelberg: Berlin; 2012. pp. 93-137

[3] Li H, Fu J, Zhang A, Zhang Q, Wang Y. Occurrence, bioaccumulation and long-range transport of short-chain chlorinated paraffins on the Fildes peninsula at king George Island, Antarctica. Environment International. 2016;**94**:408-414

[4] Huang Y, Chen L, Jiang G, He Q, Ren L, Gao B, et al. Bioaccumulation and biomagnification of short-chain chlorinated paraffins in marine organisms from the pearl river estuary, South China. Science of the Total Environment. 2019;**671**:262-269

[5] Ma X, Zhang H, Wang Z, Yao Z, Chen J, Chen J. Bioaccumulation and trophic transfer of short chain chlorinated paraffins in a marine food web from Liaodong Bay, North China. Environmental Science & Technology. 2014;**48**:5964-5971

[6] Erable B, Goubet I, Lamare S, Legoy M-D, Maugard T. Bioremediation of halogenated compounds: Comparison of dehalogenating bacteria and improvement of catalyst stability. Chemosphere. 2006;**65**:1146-1152

[7] Henschler D. Toxicity of chlorinated organic compounds: Effects of the introduction of chlorine in organic molecules. Angewandte Chemie International Edition in English. 1994;**33**: 1920-1935

[8] Singh A, Kuhad RC, Ward OP. Biological remediation of soil: An overview of global market and available technologies. In: Singh A, Kuhad RC, Ward OP, editors. Advances in Applied Bioremediation. Berlin, Heidelberg: Springer Berlin Heidelberg; 2009. pp. 1-19

[9] Bagley DM, Lalonde M, Kaseros V, Stasiuk KE, Sleep BE. Acclimation of anaerobic systems to biodegrade tetrachloroethene in the presence of carbon tetrachloride and chloroform. Water Research. 2000;**34**:171-178

[10] Duhamel M, Wehr S, Yu L, Rizvi H, Seepersad D, Dworatzek S, et al. Comparison of anaerobic dechlorinating enrichment cultures maintained on tetrachloroethene, trichloroethene, cis-dichloroethene and vinyl chloride. Water Research. 2002;**36**:4193-4202

[11] Li B, Lin K, Zhang W, Lu S, Liu Y. Effectiveness of air stripping, advanced oxidation, and activated carbon adsorption-coupled process in treating chlorinated solvent–contaminated groundwater. Journal of Environmental Engineering. 2012;**138**:903-914

[12] Zhang J, Zhang S, Liu B. Degradation technologies and mechanisms of dioxins in municipal solid waste incineration fly ash: A review. Journal of Cleaner Production. 2020;**250**:119507

[13] Ren M, Lv ZY, Xu L, Lu Q, Zhang X, Yu Y, et al. Partitioning and removal behaviors of PCDD/Fs, PCBs and PCNs in a modern municipal solid waste incineration system. Science of The Total Environment. 2020;**735**:139134

[14] Gawel A, Seiwert B, Sühnholz S, Schmitt-Jansen M, Mackenzie K. In-Situ treatment of herbicide-contaminated groundwater–feasibility study for the cases atrazine and bromacil using two novel nanoremediation-type materials. Journal of Hazardous Materials. 2020;**393**:122470

[15] Hirvonen A, Tuhkanen T, Kalliokoski P. Formation of chlorinated acetic acids during UV/H_2O_2-oxidation of ground water contaminated with chlorinated ethylenes. Chemosphere. 1996;**32**:1091-1102

[16] Mattes TE, Alexander AK, Coleman NV. Aerobic biodegradation of the chloroethenes: Pathways, enzymes, ecology, and evolution. FEMS Microbiology Reviews. 2010;**34**:445-475

[17] Dong H, Li L, Lu Y, Cheng Y, Wang Y, Ning Q, et al. Integration of nanoscale zero-valent iron and functional anaerobic bacteria for groundwater remediation: A review. Environment International. 2019;**124**: 265-277

[18] Vogel M, Nijenhuis I, Lloyd J, Boothman C, Pöritz M, Mackenzie K. Combined chemical and microbiological degradation of tetrachloroethene during the application of carbo-iron at a contaminated field site. Science of The Total Environment. 2018;**628–629**: 1027-1036

[19] Matheson LJ, Tratnyek PG. Reductive dehalogenation of chlorinated methanes by iron metal. Environmental Science & Technology. 1994;**28**: 2045-2053

[20] Mueller NC, Braun J, Bruns J, Černík M, Rissing P, Rickerby D, et al. Application of Nanoscale Zero Valent Iron (nZVI) for groundwater remediation in europe. Environmental

Science and Pollution Research. 2012;**19**: 550-558

[21] Pasinszki T, Krebsz M. Synthesis and application of zero-valent iron nanoparticles in water treatment, environmental remediation, catalysis, and their biological effects. Nanomaterials. 2020;**10**(5):917. DOI: 10.3390/nano10050917

[22] Song H, Carraway E. Reduction of chlorinated Methanes by nano-sized zero-valent iron. Kinetics, Pathways, and Effect of Reaction Conditions. Environmental Engineering Science. 2006;**23**:272-284

[23] Song H, Carraway ER. Reduction of chlorinated Ethanes by nanosized zero-valent iron: Kinetics, pathways, and effects of reaction conditions. Environmental Science & Technology. 2005;**39**:6237-6245

[24] Balda M, Kopinke F-D. The role of nickel traces in fine chemicals for hydrodechlorination reactions with zero-valent iron. Chemical Engineering Journal. 2020;**388**:124185

[25] Kopinke F-D, Sühnholz S, Georgi A, Mackenzie K. Interaction of zero-valent iron and carbonaceous materials for reduction of DDT. Chemosphere. 2020; **253**:126712

[26] Crane RA, Scott TB. Nanoscale zero-valent iron: Future prospects for an emerging water treatment technology. Journal of Hazardous Materials. 2012; **211–212**:112-125

[27] Aramendía MA, Boráu V, García IM, Jiménez C, Lafont F, Marinas A, et al. Liquid-phase hydrodechlorination of chlorobenzene over palladium-supported catalysts: Influence of HCl formation and NaOH addition. Journal of Molecular Catalysis A: Chemical. 2002;**184**:237-245

[28] Aramendía MA, Burch R, García IM, Marinas A, Marinas JM, Southward BWL, et al. The effect of the addition of sodium compounds in the liquid-phase hydrodechlorination of chlorobenzene over palladium catalysts. Applied Catalysis B: Environmental. 2001;**31**:163-171

[29] Benitez JL, Del Angel G. Effect of chlorine released during hydrodechlorination of chlorobenzene over Pd, Pt and Rh supported catalysts. Reaction Kinetics and Catalysis Letters. 2000;**70**:67-72

[30] Urbano FJ, Marinas JM. Hydrogenolysis of organohalogen compounds over palladium supported catalysts. Journal of Molecular Catalysis A: Chemical. 2001;**173**:329-345

[31] El-Sharnouby O, Boparai HK, Herrera J, O'Carroll DM. aqueous-phase catalytic hydrodechlorination of 1,2-dichloroethane over palladium nanoparticles (nPd) with residual borohydride from nPd synthesis. Chemical Engineering Journal. 2018;**342**: 281-292

[32] Kopinke F-D, Mackenzie K, Koehler R, Georgi A. Alternative sources of hydrogen for hydrodechlorination of chlorinated organic compounds in water on Pd catalysts. Applied Catalysis A: General. 2004;**271**:119-128

[33] Conrad H, Ertl G, Latta EE. Adsorption of hydrogen on palladium single crystal surfaces. Surface Science. 1974;**41**:435-446

[34] Coq B, Ferrat G, Figueras F. Conversion of chlorobenzene over palladium and rhodium catalysts of widely varying dispersion. Journal of Catalysis. 1986;**101**:434-445

[35] Teschner D, Borsodi J, Kis Z, Szentmiklósi L, Révay Z, Knop-Gericke

A, et al. Role of hydrogen species in palladium-catalyzed alkyne hydrogenation. The Journal of Physical Chemistry C. 2010;**114**:2293-2299

[36] Shee A. Evaluation of copper-based-catalysts for treatment of halogenated organic compounds in water. PhD Dissertation, Helmholtz Centre for Environmental Research - UFZ: Leipzig, Germany, 2021

[37] Shee A, Kopinke F-D, Mackenzie K. Borohydride and metallic copper as a robust dehalogenation system: Selectivity assessment and system optimization. Science of the Total Environment. 2022;**810**:152065

[38] Lowry GV, Reinhard M. Hydrodehalogenation of 1- to 3-carbon halogenated organic compounds in water using a palladium catalyst and hydrogen gas. Environmental Science & Technology. 1999;**33**:1905-1910

[39] Mackenzie K, Frenzel H, Kopinke F-D. Hydrodehalogenation of halogenated hydrocarbons in water with Pd catalysts: Reaction rates and surface competition. Applied Catalysis B: Environmental. 2006;**63**:161-167

[40] Chaplin BP, Reinhard M, Schneider WF, Schüth C, Shapley JR, Strathmann TJ, et al. Critical review of Pd-based catalytic treatment of priority contaminants in water. Environmental Science & Technology. 2012;**46**: 3655-3670

[41] Chaplin BP, Shapley JR, Werth CJ. Regeneration of sulfur-fouled bimetallic Pd-based catalysts. Environmental Science & Technology. 2007;**41**: 5491-5497

[42] Chaplin BP, Roundy E, Guy KA, Shapley JR, Werth CJ. Effects of natural water ions and humic acid on catalytic

nitrate reduction kinetics using an alumina supported Pd − Cu catalyst. Environmental Science & Technology. 2006;**40**:3075-3081

[43] Lowry GV, Reinhard M. Pd-Catalyzed TCE dechlorination in water: Effect of $[H_2]_{(Aq)}$ and H_2-utilizing competitive solutes on the TCE dechlorination rate and product distribution. Environmental Science & Technology. 2001;**35**:696-702

[44] Lowry GV, Reinhard M. Pd-Catalyzed TCE dechlorination in groundwater: Solute effects, biological control, and oxidative catalyst regeneration. Environmental Science & Technology. 2000;**34**:3217-3223

[45] Angeles-Wedler D, Mackenzie K, Kopinke F-D. Sulphide-induced deactivation of Pd/Al_2O_3 as hydrodechlorination catalyst and its oxidative regeneration with permanganate. Applied Catalysis B: Environmental. 2009;**90**:613-617

[46] Velázquez JC, Leekumjorn S, Nguyen QX, Fang Y-L, Heck KN, Hopkins GD, et al. Chloroform hydrodechlorination behavior of alumina-supported Pd and PdAu catalysts. AIChE Journal. 2013;**59**:4474-4482

[47] Wang X, Chen C, Chang Y, Liu H. Dechlorination of chlorinated methanes by Pd/Fe bimetallic nanoparticles. Journal of Hazardous Materials. 2009;**161**:815-823

[48] Lago RM, Green MLH, Tsang SC, Odlyha M. Catalytic decomposition of chlorinated organics in air by copper chloride based catalysts. Applied Catalysis B: Environmental. 1996;**8**:107-121

[49] Mohan S, Dinesha P, Kumar S. NOx Reduction behavior in copper zeolite

catalysts for ammonia SCR systems: A review. Chemical Engineering Journal. 2020;**384**:123253

[50] Raciti D, Wang C. Recent advances in CO_2 reduction electrocatalysis on copper. ACS Energy Letters. 2018;**3**:1545-1556

[51] Durante C, Huang B, Isse AA, Gennaro A. Electrocatalytic dechlorination of volatile organic compounds at copper cathode. Part II: Polychloroethanes. Applied Catalysis B: Environmental. 2012;**126**:355-362

[52] He J, Ela WP, Betterton EA, Arnold RG, Sáez AE. Reductive dehalogenation of aqueous-phase chlorinated hydrocarbons in an electrochemical reactor. Industrial & Engineering Chemistry Research. 2004;**43**:7965-7974

[53] Isse AA, Huang B, Durante C, Gennaro A. Electrocatalytic dechlorination of volatile organic compounds at a copper cathode. Part I: Polychloromethanes. Applied Catalysis B: Environmental. 2012;**126**:347-354

[54] Cheng L-J, Mankad NP. C–C and C–X coupling reactions of unactivated alkyl electrophiles using copper catalysis. Chemical Society Reviews. 2020;**49**:8036-8064

[55] Lippert T, Wokaun A, Lenoir D. Copper catalyzed aryl dehalogenation reactions and their inhibition. Berichte der Bunsengesellschaft für physikalische Chemie. 1990;**94**:1465-1471

[56] Šljukić B, Santos DMF, Sequeira CAC, Banks CE. Analytical monitoring of sodium borohydride. Analytical Methods. 2013;**5**:829-839

[57] Bennett EL, Wilson T, Murphy PJ, Refson K, Hannon AC, Imberti S, et al.

Structure and spectroscopy of CuH prepared via borohydride reduction. Acta Crystallographica Section B. 2015;**71**:608-612

[58] Schlesinger HI, Brown HC, Finholt AE, Gilbreath JR, Hoekstra HR, Hyde EK. Sodium borohydride, its hydrolysis and its use as a reducing agent and in the generation of hydrogen[1]. Journal of the American Chemical Society. 1953;**75**:215-219

[59] Vaškelis A, Jušknas R, Jačiauskien J. Copper hydride formation in the electroless copper plating process: In situ X-ray diffraction evidence and electrochemical study. Electrochimica Acta. 1998;**43**:1061-1066

[60] Díez-González S, Nolan SP. Copper, silver, and gold complexes in hydrosilylation reactions. Accounts of Chemical Research. 2008;**41**:349-358

[61] Weidlich T. The influence of copper on halogenation/dehalogenation reactions of aromatic compounds and its role in the destruction of polyhalogenated aromatic contaminants. Catalysts. 2021;**11**(3):378. DOI: 10.3390/catal11030378

[62] Gawande MB, Goswami A, Felpin F-X, Asefa T, Huang X, Silva R, et al. Cu and Cu-based nanoparticles: Synthesis and applications in catalysis. Chemical Reviews. 2016;**116**:3722-3811

[63] Khodashenas B, Ghorbani HR. Synthesis of copper nanoparticles: An overview of the various methods. Korean Journal of Chemical Engineering. 2014;**31**:1105-1109

[64] Al-Hakkani MF. Biogenic copper nanoparticles and their applications: A review. SN Applied Sciences. 2020;**2**:505

[65] Rafique M, Shaikh AJ, Rasheed R, Tahir MB, Bakhat HF, Rafique MS, et al. A review on synthesis, characterization and applications of copper nanoparticles using green method. Nano. 2017;**12**:1750043

[66] Huang C-C, Lo S-L, Lien H-L. Zero-valent copper nanoparticles for effective dechlorination of dichloromethane using sodium borohydride as a reductant. Chemical Engineering Journal. 2012;**203**: 95-100

[67] Huang C-C, Lo S-L, Tsai S-M, Lien H-L. Catalytic hydrodechlorination of 1,2-dichloroethane using copper nanoparticles under reduction conditions of sodium borohydride. Journal of Environmental Monitoring. 2011;**13**:2406-2412

[68] Kojima Y, Suzuki K, Fukumoto K, Sasaki M, Yamamoto T, Kawai Y, et al. Hydrogen generation using sodium borohydride solution and metal catalyst coated on metal oxide. International Journal of Hydrogen Energy. 2002;**27**: 1029-1034

[69] Wade RC. Catalyzed reduction of organofunctional groups with sodium borohydride. Journal of Molecular Catalysis. 1983;**18**:273-297

[70] Raut SS, Kamble SP, Kulkarni PS. Efficacy of zero-valent copper (Cu^0) nanoparticles and reducing agents for dechlorination of mono chloroaromatics. Chemosphere. 2016;**159**:359-366

[71] Ahmed OH, Altarawneh M, Al-Harahsheh M, Jiang Z-T, Dlugogorski BZ. Catalytic de-halogenation of alkyl halides by copper surfaces. Journal of Environmental Chemical Engineering. 2018;**6**:7214-7224

[72] Rioux RM, Thompson CD, Chen N, Ribeiro FH. Hydrodechlorination of chlorofluorocarbons CF_3–$CFCl_2$ and CF_3–CCl_3 over Pd/carbon and Pd black catalysts. Catalysis Today. 2000;**62**: 269-278

[73] Zhou G, Chan C, Gellman AJ. Dechlorination of fluorinated 1,1-dichloroethanes on Pd(111). The Journal of Physical Chemistry B. 1999;**103**:1134-1143

[74] Andersin J, Honkala K. First principles investigations of Pd-on-Au nanostructures for trichloroethene catalytic removal from groundwater. Physical Chemistry Chemical Physics. 2011;**13**:1386-1394

[75] Barbosa LAMM, Loffreda D, Sautet P. Chemisorption of trichloroethene on the PdCu alloy (110) surface: A periodical density functional study. Langmuir. 2002;**18**:2625-2635

[76] Girvin DC, Scott AJ. Polychlorinated biphenyl sorption by soils: Measurement of soil-water partition coefficients at equilibrium. Chemosphere. 1997;**35**: 2007-2025

[77] Meijer SN, Ockenden WA, Sweetman A, Breivik K, Grimalt JO, Jones KC. Global distribution and budget of PCBs and HCB in background surface soils: Implications for sources and environmental processes. Environmental Science & Technology. 2003;**37**:667-672

[78] Angeles-Wedler D, Mackenzie K, Kopinke F-D. Permanganate oxidation of sulfur compounds to prevent poisoning of Pd catalysts in water treatment processes. Environmental Science & Technology. 2008;**42**:5734-5739

[79] Comandella D, Woszidlo S, Georgi A, Kopinke F-D, Mackenzie K. Efforts for long-term protection of palladium hydrodechlorination catalysts. Applied Catalysis B: Environmental. 2016;**186**:204-211

[80] Kopinke F-D, Angeles-Wedler D, Fritsch D, Mackenzie K. Pd-catalyzed hydrodechlorination of chlorinated aromatics in contaminated waters— effects of surfactants, organic matter and catalyst protection by silicone coating. Applied Catalysis B: Environmental. 2010;**96**:323-328

[81] Schüth C, Disser S, Schüth F, Reinhard M. Tailoring catalysts for hydrodechlorinating chlorinated hydrocarbon contaminants in groundwater. Applied Catalysis B: Environmental. 2000;**28**:147-152

[82] El-Temsah YS, Sevcu A, Bobcikova K, Cernik M, Joner EJ. DDT Degradation efficiency and ecotoxicological effects of two types of nano-sized zero-valent iron (nZVI) in water and soil. Chemosphere. 2016;**144**:2221-2228

[83] Poursaberi T, Konoz E, Sarrafi A, Hassanisadi M, Hajifathli F. Application of nanoscale zero-valent iron in the remediation of DDT from contaminated water. Chemical Science Transactions. 2012;**1**:658-668

[84] Ševců A, El-Temsah YS, Filip J, Joner EJ, Bobčíková K, Černík M. Zero-valent iron particles for PCB degradation and an evaluation of their effects on bacteria, plants, and soil organisms. Environmental Science and Pollution Research. 2017;**24**:21191-21202

[85] Andrieux CP, Saveant JM, Su KB. Kinetics of dissociative electron transfer. Direct and mediated electrochemical reductive cleavage of the carbon-halogen bond. Journal of Physical Chemistry. 1986;**90**:3815-3823

[86] de Romaña DL, Olivares M, Uauy R, Araya M. Risks and benefits of copper in light of new insights of copper homeostasis. Journal of Trace Elements in Medicine and Biology. 2011;**25**:3-13

[87] Lin CJ, Lo S-L, Liou YH. Degradation of aqueous carbon tetrachloride by nanoscale zerovalent copper on a cation resin. Chemosphere. 2005;**59**:1299-1307

Chapter 5

Investigation of Non-Covalent Interactions of Copper (II) Complexes with Small Biomolecules

Azadeh Khanmohammadi

Abstract

In this chapter, the influence of non-covalent interactions on the complexes formed by the various biomolecules (mesalazine, para-aminosalicylic acid, acetaminophen, psoralen, and methyl salicylate) with the Cu^{2+} cation is investigated using the density functional theory (DFT) method. Since the interactions involving aromatic rings are crucial binding forces in chemical systems, this is exciting research trying to understand and control the effect of non-covalent interactions responsible for complicated functions in nature. Herein, the calculations are performed in the gas phase and water solvent. The results show that the absolute amounts of energy are reduced by going from the gas phase to the solution. The topological properties of the electron density and the values of charge transfer are evaluated by the Bader theory of atoms in molecules (AIM) and the natural bond orbital (NBO) analysis, respectively. These results are useful for understanding the role of the drug-receptor interactions in the complexes. The electronic descriptors are also important factors in forming a charge-transfer complex between cation and biological target. The results of this study that are ubiquitous in biological systems may be useful for the design and synthesis of a variety of supramolecular complexes with the desired properties.

Keywords: non-covalent interactions, DFT, AIM, NBO, HOMA

1. Introduction

Para-aminosalicylic acid (PAS) or 4-aminosalicylic acid (brand name Paser) is an antituberculosis antibiotic [1]. It is applied in combination with other antituberculosis drugs, such as isoniazid, thiacetazone, and streptomycin [2]. PAS inhibits the folic acid synthesis and is the second antibiotic useful in the treatment of tuberculosis after streptomycin [3]. In 1948, researchers demonstrated that combined treatment with streptomycin and PAS was superior to either drug alone, and established the principle of combination therapy for tuberculosis [4]. Mesalazine (MES) or 5-aminosalicylic acid (also known as mesalamine) is an intestinal aminosalicylate drug [5]. This drug is

very useful for the treatment of inflammatory bowel diseases such as ulcerative colitis and Crohn's disease [6]. The MES is similar to salicylates, but it is structurally and therapeutically different from 4-aminosalicylic acid (or p-aminosalicylic acid). Methyl salicylate (MS) is chemically known as methyl-2-hydroxybenzoate, winter-green oil, and betula oil, which has the empirical formula $C_8H_8O_3$. MS is pharmacologically similar to aspirin and has anti-inflammatory properties [7]. It is used as a rubefacient and analgesic in the treatment and temporary management of aching and painful muscles and joints [8].

Psoralen (PSO) is naturally synthesized in the form of tricyclic aromatic compounds, which is obtained by compressing a coumarin nucleus with a furan ring [9]. Since its chemical structure is similar to coumarin, it is used in the treatment of some cancers, including T-cell lymphomas in patients with AIDS [10]. It can also be utilized to treat hyperproliferative skin disorders such as psoriasis, eczema, vitiligo, and certain types of skin cancer [11]. Acetaminophen (AC) or N-acetyl-p-aminophenol (with trade names of Tylenol and Panadol) is one of the most popular and most generally applied painkillers and antipyretic drugs around the world. It has relatively low anti-inflammatory activity [12] with respect to other drugs, such as aspirin and ibuprofen. It increases the pain threshold by blocking an enzyme called cyclooxygenase (COX) [13, 14].

The non-covalent interactions (NCIs), such as hydrogen bonding, halogen bonding, and cation-π, anion-π and π-π interactions, are very important in supramolecular chemistry, drug design, protein folding, and crystal engineering [15, 16]. The hydrogen bond (HB) is the most popular form of NCI that directs many chemical, physical, and biochemical processes [17]. The HB interaction is designated as X—H⋯Y, in which X—H and Y are the proton-donor and proton-acceptor groups, respectively. Since the hydrogen atom has only one orbital (1s) with sufficiently low energy, HBs are predominantly electrostatic in nature, but covalent and repulsive orbital-orbital interactions are also present. Depending on the type of X and Y, there are strong and weak HBs. In the case of weak HBs, the respective bonding is mainly electrostatic in nature with attractive and repulsive charge-charge, charge-dipole, charge-induced dipole, and charge-multipole interactions between the partially positive charged hydrogen atom and the negatively charged areas of the Y acceptor atom. In the case of strong HBs, in addition to the Coulomb forces, the phenomena of covalent bonding through orbital-orbital overlap attractive and closed-shell repulsive forces are of particular importance.

The cation-π interactions, as another ensemble of NCIs, are significant in biological structures and molecular recognition processes [18]. These interactions represent a strong attraction between the cations and the π-system. The electrostatic and induction interactions are mainly responsible for the attraction. The electrostatic interaction is between the quadrupole of the π-system and the charge of the cation [19]. The magnitude of the induction interaction is proportional to the square of the electric field produced by the cation [20]. Thus, the cations with greater charge have large induction energies.

The importance of cation-π interactions and their physical origin is also vital for understanding the structures and properties of molecular assemblies, improving material and drug design strategies [21]. For example, the role of cation-π interactions in the stability and design of peptides was investigated in 2001 [22]. In this study, the cation-π interactions between amino acid side chains are increasingly recognized as important structural and functional features of proteins and other biomolecules. It is also generally understood that helical proteins are stabilized by a combination of

hydrophobic and packing interactions, together with H-bonds and electrostatic interactions. In 2001 [23], Kallenbach et al. showed that polar side-chain interactions on the surface can play an important role in helix formation and stability.

Interactions of metals with biomolecules play an important role in pharmaceutical chemistry [24] through "classical" organometallic chemistry to environment protection (metal-binding biomass) [25]. The role of metal ions in the structure and function of proteins, nucleic acids, and peptide hormones is essential. The pharmacology of metal-drug interactions may depend on the method of management. A metal-drug complex can be directed as a therapeutic agent, or the drug can be administered and interact with metal ions in the body. In addition, the application of drugs in chelating with metal ions or change in the polarity of the medium may affect their chemical and biological properties [26, 27].

Complexes obtained from M (II) ions with strong bioactive ligands containing N and O donor binding sites are employed for biological, analytical, agricultural, industrial, and medicinal purposes [28]. Metal ions are the ultimate components of a healthy life for humans and animals [29]. Copper (Cu) is biologically an appropriate metal associated with different biomolecules due to crucial physiological activities, and it is an important suggestion element for many biological functions [30]. For example, the biological activities of the isolated metal chelates were screened against different types of bacteria and fungi. Rayan et al. [31] showed that the cetirizine drug and the complexes inhibited the growth of tested bacteria to varying degrees, more pronounced when coordinated with the metal ions.

Cu (II) shows an essential character for improving connective tissue, nerve coverings, and bone in humans. The Cu (II) complexes with their bioessential activity and oxidative nature are applied in various biological activities, including antibacterial [32], antitumor [33], antifungal [34], antioxidant [35], and anti-inflammatory [36]. Due to the biological importance of copper cation, it is necessary to consider complexation with bioactive ligands to identify the function of their complexes and to discover new bioactive compounds.

The main purpose of this study is to analyze the effects of NCIs on the energetic, geometric, topological, charge transfer, and electronic descriptors of considered complexes. For this goal, DFT calculations and AIM and NBO analyses are carried out on the MES, PAS, AC, PSO, and MS biomolecules with Cu^{2+} cation. Furthermore, the effect of these interactions on the aromaticity of the complexes is evaluated by calculating the geometry-based HOMA aromaticity index. In order to deal with this issue in depth, we present an inclusive analysis of the interactions mentioned in the electronic properties of the studied complexes. It should be declared that the importance of theoretical models for these interactions in biological systems has allowed us to study them.

2. Computational procedures

In this study, all calculations are implemented with the Gaussian 09 suite of programs [37]. The geometry optimization is performed at the wB97XD/6-311++G(d,p) level of theory in the gas phase and water solvent. The used basis set is of triple-ζ quality [38] for valence electrons with diffuse functions, which are suitable in computations for ions and structures with lone-pair electrons [39]. The calculations of frequency are carried out at the same level to verify that these structures are local minima on the energy surfaces. The solvent effect for the water solution is obtained using the polarizable continuum model (PCM) [40]. The binding energy with

correction for the basis set superposition error (BSSE) is calculated using the Boys-Bernardi counterpoise technique [41] as follows:

$$\Delta E = E_{cation-\pi} - \left(E_{cation} + E_{\pi-system}\right) + E_{BSSE} \qquad (1)$$

According to this formula, $E_{cation-\pi}$ is the total energy of the complexes and E_{cation} and $E_{\pi-system}$ are the total energies of the free cation and the π-systems, respectively. The stability of the complexes in the presence of water solvent is investigated, and their results are compared with the gas phase. The stabilization energy (E_{stab}) can be calculated from the total energies at the same level of theory as follows:

$$E_{stab} = E_{tot}\,(solvent) - E_{tot}\,(gas) \qquad (2)$$

where E_{tot} (solvent) and E_{tot} (gas) are the total energy of the complexes in the presence and absence of solvent, respectively. The topological electron charge density is analyzed by the atoms in molecules (AIM) method [42]. The natural bond orbital (NBO) analysis [43] is used to determine the direction and magnitude of donor-acceptor interactions. The AIM and NBO calculations are carried out with the AIM2000 [44] and NBO programs [45] under the Gaussian 09 program package, respectively. The harmonic oscillator model of aromaticity (HOMA) [46] index is applied as a geometric criterion of local aromaticity according to the formula suggested by Kruszewski and Krygowski [47]:

$$HOMA = 1 - \frac{\alpha}{n}\sum_{i=0}^{n}\left(R_{opt} - R_i\right)^2 \qquad (3)$$

where n is the number of bonds within the investigated rings, α is a constant, and R_{opt} and R_i are the optimal values of bond lengths for ideally and studied aromatic

(a)

(b)
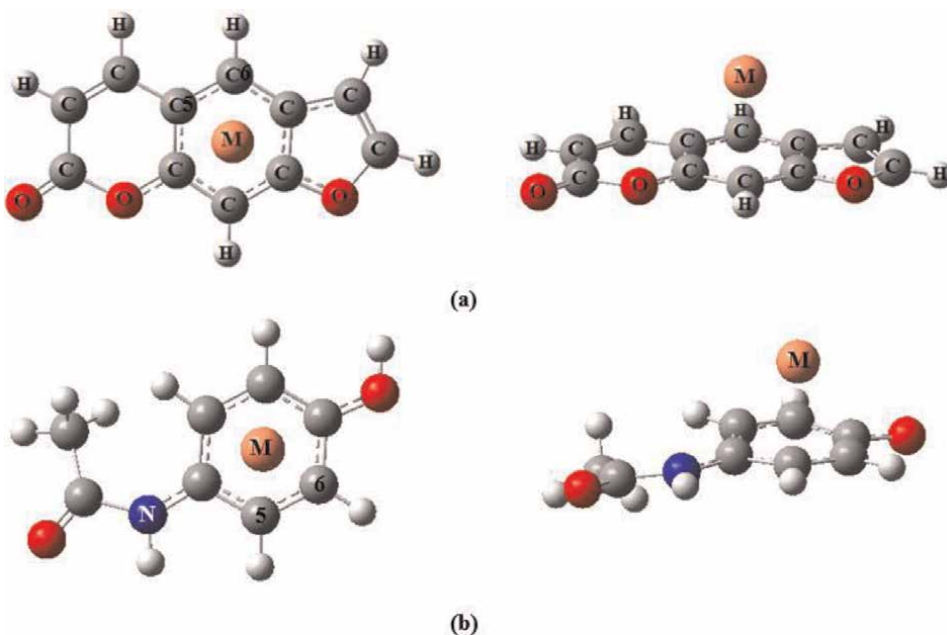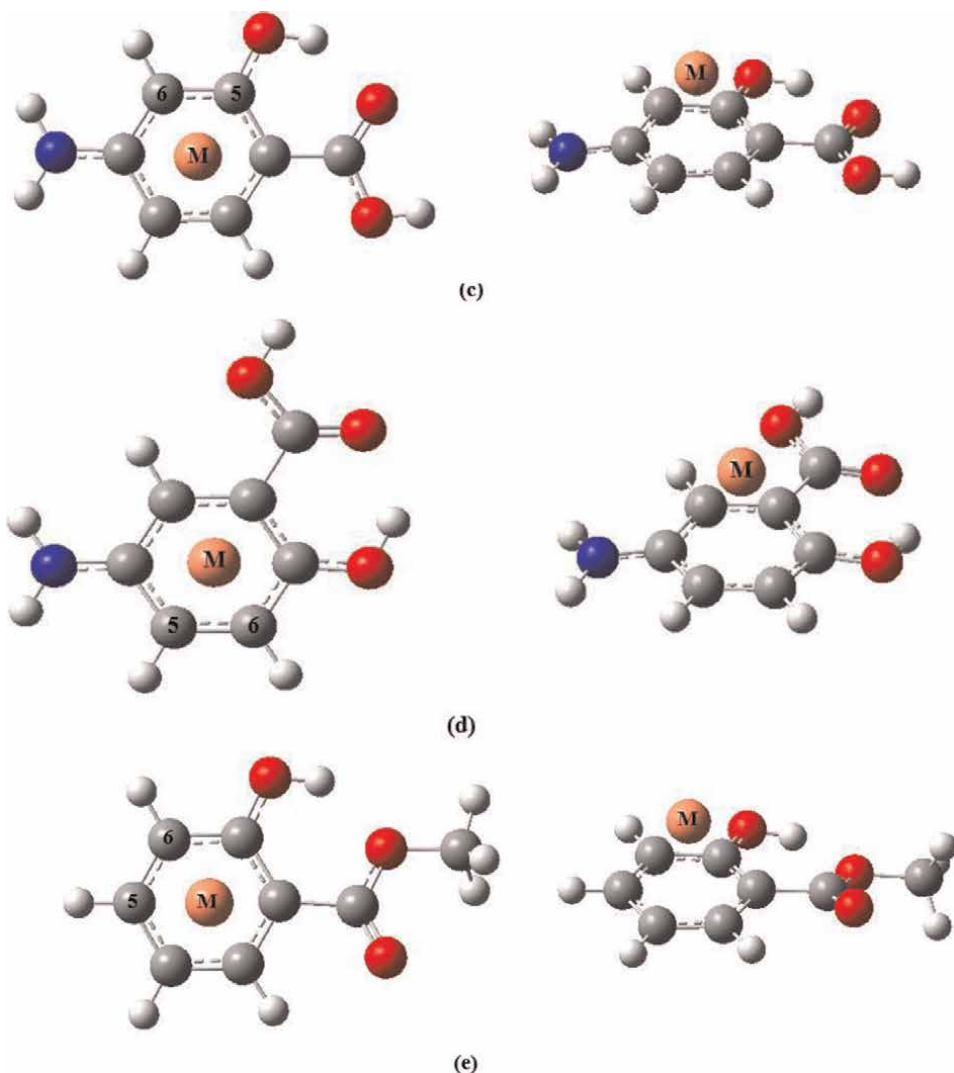
Figure 1.
The model representation for the PSO⋯M (a), AC⋯M (b), PAS⋯M (c), MES⋯M (d) and MS⋯M (e) complexes, with M = Cu²⁺ from front and top views.

systems. In this research, the R_{opt} and α are estimated at the wB97XD/6-311++G(d,p) level of theory (for CC and CO bonds: $R_{opt,CC}$ = 1.393 Å, $R_{opt,CO}$ = 1.270 Å, α_{CC} = 89.34, α_{CO} = 77.22). Here, HOMA = 1 is ideal for aromatic systems and HOMA = 0 is for nonaromatic species. Finally, the molecular orbital calculations, such as the highest occupied molecular orbital (HOMO) and the lowest unoccupied molecular orbital (LUMO) energies, are performed on the explored systems.

3. Results and discussions

In this work, the effects of NCIs on the different biomolecules of MES, PAS, AC, PSO, and MS with Cu²⁺ cation (**Figure 1**) are investigated. As shown in these Figures,

the PSO and AC complexes have only the cation···π interaction, while the PAS, MES, and MS complexes have the two NCIs of cation···π and intramolecular hydrogen bond (IMHB) in their structure.

3.1 Energetic descriptors

The binding energies corrected with BSSE ($\Delta E_{ion-\pi}$) of the complexes are listed in **Table 1**. It is well known that the strength of the cation···π interactions strongly depends on the physical properties of the cations and the π-system, the solvation effects, and the interaction geometry. The results show that the obtained absolute values of $\Delta E_{ion-\pi}$ in the gas phase and water solvent are arranged in MES > PAS > AC > PSO > MS order. It is obvious that these values decrease with going from the gas phase to the solution. For example, the binding energy of the MES···Cu^{2+} complex reduces from −259.87 kcal/mol in the gas phase to −101.24 kcal/mol in the water solvent. However, as shown in **Table 1**, the highest and lowest values of $\Delta E_{ion-\pi}$ in both the gas phase and solution belong to the MES and MS complexes, respectively.

The IMHB energy of the complexes is estimated by means of the Espinosa method [48]. The potential and kinetic energy densities can be determined from the following equations:

$$G(r_{CP}) = \left(\frac{3}{10}\right)\left(3\pi^2\right)^{\frac{2}{3}} \rho^{\frac{5}{3}}(r_{CP}) + \left(\frac{1}{6}\right)\nabla^2\rho(r_{CP}) \qquad (4)$$

$$V(r_{CP}) = \left(\frac{1}{4}\right)\nabla^2\rho(r_{CP}) - 2G(r_{CP}) \qquad (5)$$

where G(r) is the kinetic energy density, V(r) is the potential energy density, and ρ(r) and $\nabla^2\rho$(r) are the electron density and its Laplacian at the critical point (CP),

	$\Delta E_{ion-\pi}$	E_{HB}	E_{tot}	E_{stab}	E_{rel}	ΔH_{298}	ΔG_{298}	ΔS_{298}
Gas phase								
MES···Cu^{2+}	−259.87	−17.65	−59598.2346	—	8.2885	−0.446	7.628	−0.027
PAS···Cu^{2+}	−249.71	−20.44	−59598.0429	—	8.1349	−0.410	7.437	−0.026
AC···Cu^{2+}	−248.78	—	−58619.7787	—	8.3103	−0.342	7.737	−0.027
PSO···Cu^{2+}	−237.65	—	−62235.5111	—	8.1734	0.033	7.216	−0.024
MS···Cu^{2+}	−228.54	−17.85	−59159.6074	—	8.3435	−0.080	7.299	−0.025
Water								
MES···Cu^{2+}	−101.24	−14.78	−59606.5231	−8.2885	0.0000	−0.452	7.760	−0.028
PAS···Cu^{2+}	−87.30	−15.18	−59606.1779	−8.1349	0.0000	−0.383	7.559	−0.027
AC···Cu^{2+}	−88.72	—	−58628.0889	−8.3103	0.0000	−0.651	8.842	−0.032
PSO···Cu^{2+}	−76.58	—	−62243.6845	−8.1734	0.0000	−0.152	7.732	−0.026
MS···Cu^{2+}	−73.71	−14.28	−59167.9510	−8.3435	0.0000	−0.242	7.729	−0.027

Table 1.
The BSSE-corrected binding and IMHB energies ($\Delta E_{ion-\pi}$ and E_{HB}, in kcal mol^{-1}), total energy (E_{tot}, in eV), stabilization energy (E_{stab}, in eV), relative energy (E_{rel}), and thermodynamic parameters of complex formation in the gas phase and water solvent (ΔH, ΔG, and ΔS, in kcal mol^{-1}).

respectively. The simple relationship between the HB energy (E_{HB}) and the potential energy density $V(r_{cp})$ at the critical point corresponding to the H···O contact is assigned to be as follows [49]:

$$E_{HB} = \frac{1}{2} V(r_{CP}) \qquad (6)$$

According to the results, the order of E_{HB} for the selected complexes in the gas phase and in water is PAS > MS > MES and PAS > MES > MS, respectively (see **Table 1**). As shown in this table, the strongest HB is related to the PAS complex, and the E_{HBs} obtained in both the gas phase and solution for the MES and MS complexes are close to each other and lower than the PAS complex.

The values of total energy (E_{tot}), stabilization energy (E_{stab}), and relative energy (E_{rel}) of the complexes are listed in **Table 1**. The calculations show that the PSO and AC complexes have the most and least stability in the gas and water phases, respectively. The structure's stability according to the total energy in the gas phase and solution obeys the following order: PSO > MES > PAS > MS > AC. There is a good linear relationship between the total energy (E_{tot}) and the dipole moment ($\mu°$) of the complexes in the water solvent (see **Figure 2**). This correlation displays that increasing stability is associated with enhancing dipole moment. For the studied complexes, the E_{stab} values follow the MS > AC > MES > PSO > PAS order. In water solvent, the E_{stab} of MS complex is the highest and the lowest value is related to the PAS complex. The results also show a similar trend for the relative energies obtained in the analyzed complexes. **Figure 3** illustrates the stability diagram of different biomolecules in terms of relative energy (E_{rel}) in the gas and water phases. It is clear that the stability changes depend on the dielectric constant. In other words, with increasing dielectric constant, the stability enhances.

To achieve better insight into the mentioned interactions, we have calculated the Gibbs free energy (ΔG), enthalpy (ΔH), and entropy (ΔS) thermodynamic changes at 298.15 Kelvin and 1 atmosphere, which are obtained from the frequency calculations. The results are collected in **Table 1**. As shown in this Table, in most cases, the calculated ΔH values for the complexes are negative and the ΔG values are positive (see **Table 1**). The negative ΔH values reveal that the formation of these complexes is enthalpically favorable. It is well known that the complexes with lower/higher ΔG values are relatively more stable/unstable, respectively. Nevertheless, the smaller
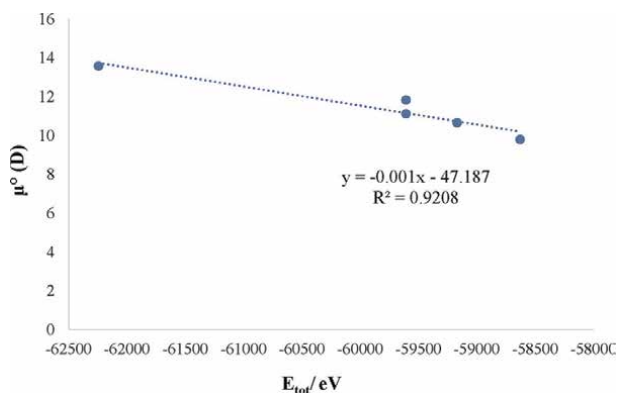
Figure 2.
Correlation between the total energy (E_{tot}) and dipole moment ($\mu°$) in water solvent.
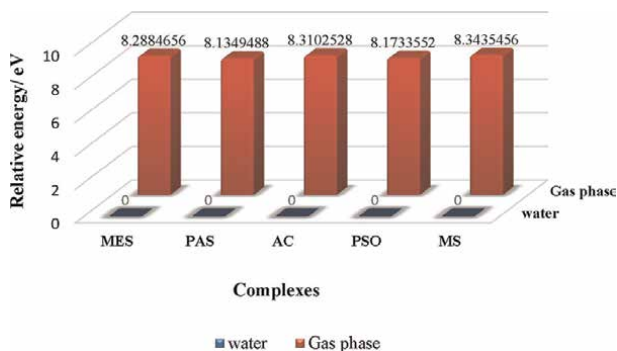
Figure 3.
Chart of the stability order in terms of relative energy (E_{rel}) in gas phase and water solvent.

values of ΔH compared to those of ΔG are due to the entropic effect. This means that the ΔS values are negative in all cases studied, and the $T\Delta S$ values indicate the large entropy changes during the formation of complexes. Since the selected complexes in water solvent are more stable than in the gas phase, in most cases the complexes of this phase are described with higher ΔH values.

3.2 Geometric descriptors

In the selected complexes, after optimizing the geometry, the cations do not remain exactly along the perpendicular symmetric axis of the benzene ring and approach to the ring bonds. It seems that the deviation of cations from the symmetric axis of the benzene ring can be related to the more negative electronic charge of the C5–C6 bond. In the PAS complex, the cation approaches the C6 position. **Table 2** presents the geometrical parameters of the complexes formed between the Cu^{2+} cation

	$d_{\pi\cdots M}$	HOMA	d_{O-H}	$d_{O\cdots O}$	$d_{H\cdots O}$	θ_{OHO}	HOMA	$\mu°$ (D)
Gas phase								
MES$\cdots$Cu^{2+}	2.112	0.866	1.005	2.532	1.644	144.6	0.738	8.30
PAS$\cdots$Cu^{2+}	2.070	0.821	1.011	2.510	1.602	146.9	0.715	7.65
AC$\cdots$Cu^{2+}	2.126	0.886	—	—	—	—	—	4.90
PSO$\cdots$Cu^{2+}	2.126	0.855	—	—	—	—	—	8.52
MS$\cdots$Cu^{2+}	2.162	0.868	1.006	2.520	1.632	144.6	0.669	6.58
Water								
MES$\cdots$Cu^{2+}	2.109	0.901	0.990	2.574	1.698	145.3	0.799	11.83
PAS$\cdots$Cu^{2+}	2.076	0.861	0.989	2.573	1.689	146.6	0.746	11.12
AC$\cdots$Cu^{2+}	2.115	0.900	—	—	—	—	—	9.80
PSO$\cdots$Cu^{2+}	2.116	0.895	—	—	—	—	—	13.58
MS$\cdots$Cu^{2+}	2.126	0.896	0.989	2.556	1.701	142.3	0.728	10.66

Table 2.
The geometrical parameters (bond lengths (d), in Å and bond angles (θ), in °), HOMA values, and dipole moment ($\mu°$ in Debye) of complexes calculated at the wB97XD/6-311++G(d,p) level of theory.

and the different π-systems. The strength of the cation-π interactions can be described by the distance between the cation and the benzene ring ($d_{\pi\cdots M}$). Theoretical results show that the stronger cation-π interaction is associated with the smaller $d_{\pi\cdots M}$ and *vice versa* (except for the MES complex). The minimum and maximum values of $d_{\pi\cdots M}$ in the gas phase and water correspond to the PAS and MS complexes, respectively.

The HB is the most common form of NCIs, which is formed between a hydrogen atom attached to an electronegative donor atom and an adjacent acceptor atom. In this chapter, the strength of the IMHB can change with the geometric parameters of the O—H⋯O unit. The values of bond lengths and their corresponding angles are given in **Table 2**. The obtained results show that in most cases, in both phases, with increasing the strength of HB, the O—H bond length (d_{O-H}) and the OHO angle (θ_{OHO}) increase and the O⋯O ($d_{O \ldots O}$) and H⋯O ($d_{H \ldots O}$) distances decrease. The O—H proton donor bond is usually stretched due to HB formation, and this elongation is greater for stronger HBs. The shorter the H⋯O distance, the stronger the HB. These results are consistent with the calculated HB energies.

The structure, reactivity, and stability of the cyclic organic molecules can be determined by aromaticity indices. The geometric parameters of the rings (CC and CO bond lengths) are applied to estimate the so-called geometrical indices of aromaticity based on the HOMA model [41]. This index is used to assess the aromaticity of the benzene ring and the quasi-ring of the O—H⋯O unit. The data in **Table 2** indicate that the HOMA index of the complexes in the gas and water phases is in the range of 0.821–0.901. Our results display that the maximum and minimum HOMA values of the HB unit are related to the MES and MS complexes, respectively. Based on the calculated data, the complexes in the gas phase have the least aromaticity, while the most aromaticity belongs to the water solvent (see **Table 2**). In fact, higher HOMA values can be attributed to more electron delocalization. Hence, the greater stability of

	π⋯M					HB				
	$\rho(r)$	$\nabla^2\rho(r)$	$H(r)$	$V(r)$	$-G/V$	$\rho(r)$	$\nabla^2\rho(r)$	$H(r)$	$V(r)$	$-G/V$
Gas phase										
MES⋯Cu^{2+}	0.0724	0.1671	−0.0222	−0.0862	0.742	0.0540	0.1427	−0.0103	−0.0562	0.817
PAS⋯Cu^{2+}	0.0804	0.1722	−0.0286	−0.1003	0.715	0.0600	0.1472	−0.0141	−0.0651	0.783
AC⋯Cu^{2+}	0.0710	0.1726	−0.0206	−0.0843	0.756	—	—	—	—	—
PSO⋯Cu^{2+}	0.0716	0.1644	−0.0217	−0.0846	0.743	—	—	—	—	—
MS⋯Cu^{2+}	0.0682	0.1814	−0.0176	−0.0805	0.781	0.0539	0.1518	−0.0094	−0.0568	0.834
Water										
MES⋯Cu^{2+}	0.0749	0.2012	−0.0214	−0.0931	0.770	0.0476	0.1343	−0.0067	−0.0471	0.857
PAS⋯Cu^{2+}	0.0795	0.1677	−0.0282	−0.0984	0.713	0.0485	0.1365	−0.0071	−0.0483	0.853
AC⋯Cu^{2+}	0.0744	0.2044	−0.0208	−0.0926	0.776	—	—	—	—	—
PSO⋯Cu^{2+}	0.0735	0.1801	−0.0220	−0.0891	0.753	—	—	—	—	—
MS⋯Cu^{2+}	0.0747	0.2164	−0.0200	−0.0941	0.787	0.0458	0.1412	−0.0051	−0.0455	0.888

Table 3.
The selected topological properties of electron density (in a.u.) obtained by AIM analysis.

the complexes in the water solvent is due to their more electron delocalization in this solvent.

The dipole moment of the complexes ($\mu°$) in the gas and solution phases is reported in **Table 2**. Dipole moment can be used as a descriptor to represent the motion of a charge across a molecule. Direction of the dipole moment vector in a molecule depends on the centers of positive and negative charges. The computations offer that the difference between the dipole moments can be related to the values of the charge on the metal cation and environmental factors. It is obvious that the PSO complex has the largest dipole moment, while the smallest value is observed in the AC complex. This may be expressed by considering the amount of charge on the Cu^{2+} cation of the complexes. It is worth mentioning that in the PSO complex, the Cu^{2+} cation has the highest positive charge, while there is less positive charge on the Cu^{2+} cation in the AC complex. According to the obtained results, the dipole moment values of the analyzed complexes in the water solvent are higher than their corresponding values in the gas phase.

3.3 Topological descriptors

In order to explore the nature and strength of NCIs in the selected biomolecules, AIM analysis is performed. The charge density, $\rho(r)$, Laplacian of electron density, $\nabla^2\rho(r)$, total electron energy density, $H(r)$, and its components ($G(r)$ and $V(r)$) at the bond critical point (BCP) are utilized to obtain the topological parameters of the studied complexes. The sign of $\nabla^2\rho(r)$ is used to recognize closed-shell and shared-shell interactions. The values of $\nabla^2\rho(r) < 0$ exhibit shared-shell interactions in covalent forces, while the values of $\nabla^2\rho(r) > 0$ indicate closed-shell interactions in HBs, ionic bonds, and van der Waals forces [50]. The molecular graphs of complexes analyzed using the AIM2000 program package are illustrated in **Figure 4**.

According to the results of AIM analysis obtained in **Table 3**, the electron density properties calculated for the complexes show that $\pi\cdots M$ bonding has low $\rho(r)$ (ranging from 0.0682 to 0.0804) and positive $\nabla^2\rho(r)$ values (ranging from 0.1644 to 0.2164) but the corresponding $H(r)$ values are negative (ranging from -0.0176 to -0.0286). These data indicate that the cation-π interactions in the selected systems are at least partially covalent in nature. Our findings in **Table 3** show that the order of the $\rho_{\pi\cdots M}$ values for the complexes in the gas phase and in water is PAS > MES > PSO > AC > MS and PAS > MES > MS > AC > PSO, respectively. As observed, the highest value of $\rho_{\pi\cdots M}$ in both phases belongs to the PAS complex. Contrary to the calculated binding energies, it is evident in **Table 3** that the obtained values of $\rho(r)$ and $\nabla^2\rho(r)$ increase with going from the gas phase to the solution (except for the PAS complex).

The formation of HB in the complexes is confirmed with the presence of a bond critical point between the hydrogen atom of the donor group and the acceptor atom. The calculated topological parameters are given in **Table 3**. As can be seen in this table, the electron density of the $H\cdots O$ contact at BCP ($\rho_{H\cdots O}$) for the PAS complex is higher than the other ones in both the gas phase and the solution. It is also clear that the values of $\rho_{H\cdots O}$ and $\nabla^2\rho_{H\cdots O}$ calculated in the gas phase are larger than the water solvent. Furthermore, the values of $\nabla^2\rho(r) > 0$ and $H(r) < 0$ show that the HB interaction of the complexes is in the category of medium HBs. The $-G/V$ ratio can also be exploited as a criterion for the character of NCIs [51, 52]: for $-G/V > 1$, and the interaction is electrostatic, while for $0.5 < -G/V < 1$, it is partially covalent. The
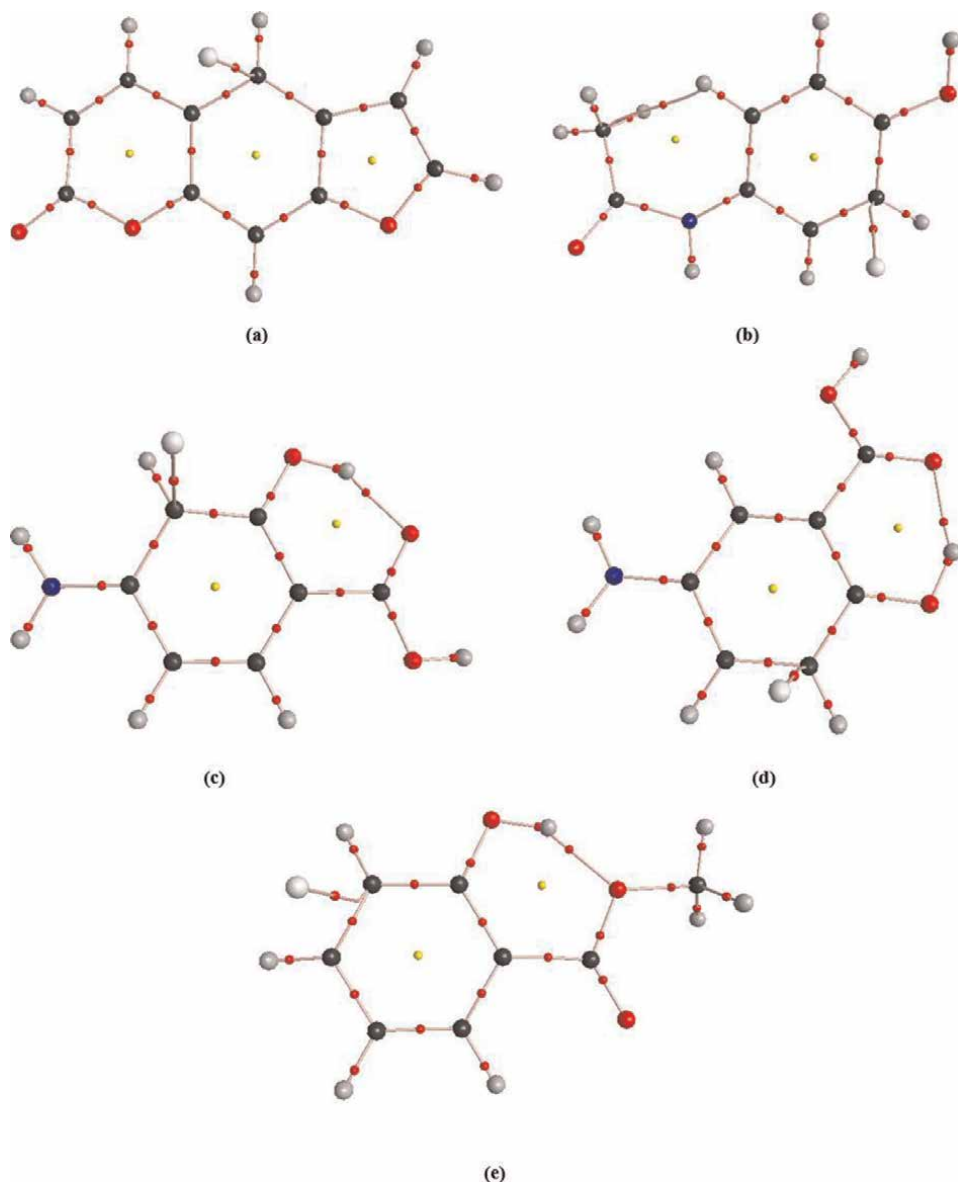
Figure 4.
The molecular graphs of PSO (a), AC (b), PAS (c), MES (d) and MS (e) complexes explored in this study.

results obtained in **Table 3** show that the NCIs in the systems under study are partially covalent.

3.4 Charge transfer descriptors

The NBO analysis explores the orbital interactions and the charge transfer values of the complexes [43]. The stabilization energy ($E^{(2)}$) estimated by the second-order perturbation theory, the occupation numbers of donor (ON_D) and acceptor (ON_A) orbitals, and the values of charge transfer (Δq_{CT}) are given in **Table 4**. The NBO

	π···M interaction				HB interaction				
	$\pi_{(C-C)} \rightarrow LP^*_{(M)}$				$LP_{(O)} \rightarrow \sigma^*_{(O-H)}$				
	$E^{(2)}$	$ON_{\pi(C-C)}$	$ON_{LP^*(M)}$	$\Delta q_{(CT1)}$	$E^{(2)}$	$ON_{LP(O)}$	$ON_{\sigma^*(O-H)}$	$q_{(O)}$	$\Delta q_{(CT2)}$
Gas phase									
MES···Cu^{2+}	19.68	0.886	0.056	1.145	14.12	0.914	0.033	−0.233	0.111
PAS···Cu^{2+}	16.97	0.850	0.061	1.098	17.43	0.911	0.039	−0.227	0.137
AC···Cu^{2+}	19.63	0.885	0.055	1.152	—	—	—	—	—
PSO···Cu^{2+}	16.98	0.875	0.051	1.107	—	—	—	—	—
MS···Cu^{2+}	16.53	0.871	0.046	1.179	14.42	0.959	0.031	−0.293	−0.059
Water									
MES···Cu^{2+}	20.82	0.884	0.057	1.039	11.69	0.917	0.029	−0.319	0.066
PAS···Cu^{2+}	17.93	0.862	0.062	0.995	12.15	0.917	0.031	−0.301	0.112
AC···Cu^{2+}	20.50	0.882	0.057	0.992	—	—	—	—	—
PSO···Cu^{2+}	17.17	0.873	0.051	0.943	—	—	—	—	—
MS···Cu^{2+}	17.91	0.862	0.048	1.060	10.86	0.964	0.025	−0.212	0.012

Table 4.
The values of $E^{(2)}$ correspond to $\pi_{(C-C)} \rightarrow LP^*_{(M)}$ and $LP_{(O)} \rightarrow \sigma^*_{(O-H)}$ interactions (in kcalmol^{-1}), occupation numbers of donor (ON_D) and acceptor (ON_A) orbitals, oxygen atomic charges ($q_{(O)}$), and the charge transfers ($\Delta q_{(CT)}$ in e) in the studied complexes.

analysis is performed to evaluate the intermolecular interactions between biomolecules and the Cu^{2+} cation. The results indicate a charge transfer from π-system of the donor species (π_{C-C}) to the $LP^*_{(M)}$ (an "empty" lone pair of cation) as acceptor species ($\pi_{(C-C)} \rightarrow LP^*_{(M)}$). As shown in **Table 4**, the maximum and minimum values of $E^{(2)}$ in the gas phase belong to the MES and MS complexes, respectively, which correspond to their binding energies. In addition, despite the obtained binding energies, the donor-acceptor energy of the cation-π interaction increases on passing from the gas phase to the solution phase.

The results of the NBO analysis for HB interaction indicate that the lone pairs of oxygen (LP_O) as donor and antibonding orbital of O—H (σ^*_{O-H}) as acceptor provide high stability in the complexes ($LP_{(O)} \rightarrow \sigma^*_{(O-H)}$). As can be seen in **Table 4**, the greatest values of $E^{(2)}$ are related to the gas phase, while the smallest values correspond to the water solvent. The trend of these results is similar to the obtained HB energies. An increase in the occupancy number of the $\sigma^*_{(O-H)}$ antibond orbital (ON_{σ^*O-H}) and further weakening and lengthening of the O—H bond can be observed in HB systems. Inspection of **Table 4** reveals that the highest values of $E^{(2)}$ and ON_{σ^*O-H} and the lowest values of $ON_{LP(O)}$ in both the gas phase and solution belong to the PAS···Cu^{2+} complex. This means that the HB is stronger in this complex compared with the others. Consequently, the changes in the occupation numbers of the $LP_{(O)}$ (ON_{LPO}) and $\sigma^*_{(O-H)}$ (ON_{σ^*O-H}) are in agreement with the energy of charge transfer from $LP_{(O)}$ to $\sigma^*_{(O-H)}$ (E^2) and the HB formation energy (E_{HB}) (except for the MS complex in the gas phase).

The charge transfer is a significant aspect in determining donor and acceptor species. The change of charges leads to charge transfer and molecular polarization in the interaction process. From the difference between the cation charges in the

complex state and the free state, the values of charge transfer (Δq_{CT1}) between the biomolecule rings and the Cu^{2+} cation are obtained. The results of **Table 4** show that the most/least values of $\Delta q_{(CT1)}$ are related to complexes in the gas phase/solution, respectively.

In the NBO analysis of HB systems, the charge transfer between the lone pairs of proton acceptor and antibonds of the proton donor is the most important. The charge transfer (Δq_{CT2}) for these systems is determined by the difference between the atomic charges of oxygen in the complexes and their corresponding monomers as: $\Delta q_{(CT2)} = q_O \text{ (complex)} - q_O \text{ (monomer)}$. As observed in **Table 4**, the highest absolute values of $\Delta q_{(CT2)}$ are observed in the gas phase and the lowest values are obtained in the water solvent, which in most cases correspond to their values of $E^{(2)}$.

3.5 Electronic descriptors

The frontier molecular orbitals (FMOs) are investigated to evaluate the stability and reactivity of the studied biomolecules. The significant FMOs usually express the chemical behavior of complexes. The important concepts in quantum chemistry are the highest occupied molecular orbital (HOMO), the lowest unoccupied molecular orbital (LUMO), and its energy gap. **Figure 5** illustrates the plots of the HOMO and LUMO orbitals of the selected complexes in the gas phase as obtained at the wB97XD/6-311++G(d,p) level of theory. In the corresponding diagrams, the red and green colors denote the positive and negative phases, respectively.

Some chemical concepts, such as energy gap (E_g), chemical potential (μ) [53], global hardness (η) [54], electrophilicity index (ω) [55], global softness (S), and electronegativity (χ) [56], are reported in **Table 5**. These quantities are identified as descriptors of chemical reactivity that are determined from the orbital energies of HOMO and LUMO based on the equations of Koopman's theorem [57]. The chemical potential and chemical hardness are the first and second partial derivatives of $E[\rho]$, respectively, with respect to the number of electrons under the constant external potential, which are given below:

$$\mu = \left(\frac{\partial E}{\partial N}\right)_{V(r),T} \tag{7}$$

$$\eta = \left(\frac{\partial^2 E}{\partial N^2}\right)_{V(r),T} \tag{8}$$

$$S = \frac{1}{2\eta} \tag{9}$$

$$\omega = \frac{\mu^2}{2\eta} \tag{10}$$

The softness (S) is a key factor in the study of the polarizability of molecules [58], and the electrophilic nature of a molecule is expressed by the electrophilicity index.

It is apparent that the larger values of E_g and η display higher molecular stability and lower reactivity in chemical reactions [59]. Inspection of **Table 5** shows that the values of E_g increase in the following order MS > PAS > AC > MES > PSO. As can be seen, the hardest and the most stable system belongs to the MS complex, while the softest and the most reactive system corresponds to the PSO complex. From the results of **Table 5**, it can be observed that the values of the electronic chemical
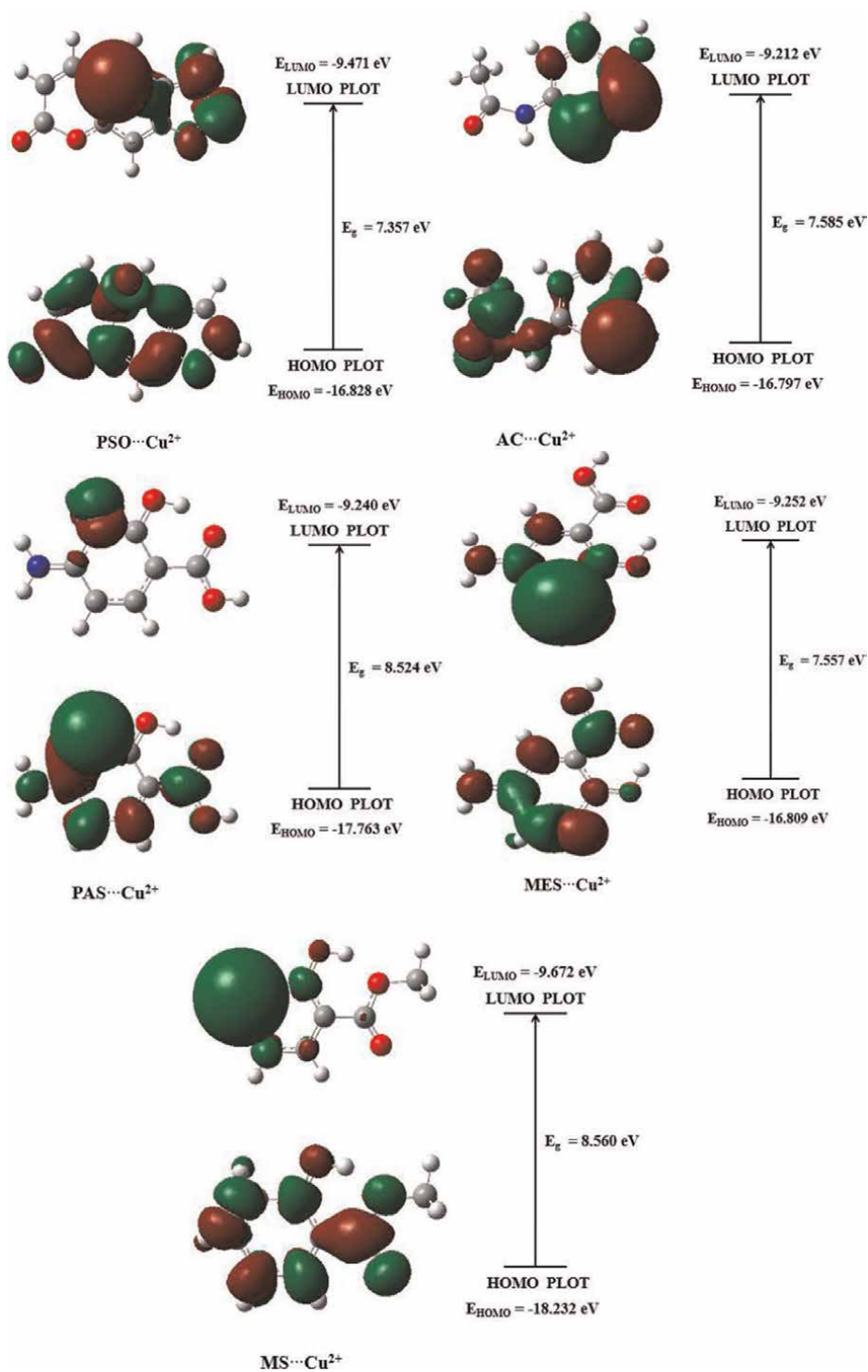
Figure 5.
*HOMO and LUMO plots of PSO, AC, PAS, MES and MS complexes obtained at the wB97XD/6-311++G(d,p) level of theory.*

	E_{HOMO} (eV)	E_{LUMO} (eV)	E_g (eV)	η (eV)	S (eV^{-1})	μ (eV)	χ (eV)	ω (eV)
Gas phase								
MES$\cdots$Cu^{2+}	−16.809	−9.252	7.557	3.779	0.132	−13.031	13.031	22.468
PAS$\cdots$Cu^{2+}	−17.763	−9.240	8.524	4.262	0.117	−13.501	13.501	21.386
AC$\cdots$Cu^{2+}	−16.797	−9.212	7.585	3.792	0.132	−13.004	13.004	22.296
PSO$\cdots$Cu^{2+}	−16.828	−9.471	7.357	3.678	0.136	−13.150	13.150	23.505
MS$\cdots$Cu^{2+}	−18.232	−9.672	8.560	4.280	0.117	−13.952	13.952	22.742
Water								
MES$\cdots$Cu^{2+}	−9.297	−1.604	7.693	3.847	0.130	−5.450	5.450	3.861
PAS$\cdots$Cu^{2+}	−10.183	−1.253	8.929	4.465	0.112	−5.718	5.718	3.661
AC$\cdots$Cu^{2+}	−9.485	−1.079	8.405	4.203	0.119	−5.282	5.282	3.319
PSO$\cdots$Cu^{2+}	−9.836	−2.009	7.827	3.914	0.128	−5.922	5.922	4.481
MS$\cdots$Cu^{2+}	−10.757	−1.724	9.033	4.516	0.111	−6.240	6.240	4.311

Table 5.
Values of the HOMO and LUMO energies (E_{HOMO} and E_{LUMO}), energy gap (E_g), chemical hardness (η), softness (S), electronic chemical potential (μ), electronegativity (χ), and electrophilicity index (ω).

potential are negative. This indicates that all complexes are stable. The electronegativity (χ) is defined as the negative of μ, as follows: $\chi = -\mu$. Our findings display that the maximum and minimum values of electronegativity correspond to the MS and AC complexes, respectively. The trend in the values of electrophilicity index is PSO > MS > MES > AC > PAS. As it is obvious, the maximum electrophilicity index is accompanied by the minimum value of E_g. This is due to the higher electron flow between the HOMO and LUMO orbitals in the related complex.

Molecular electrostatic potential (MEP) surfaces show the three-dimensional charge distributions of molecules. Different colors are used to represent the values of the surface electrostatic potentials. The red and blue regions in the MEP map are related to the electron-rich and electron-poor areas, respectively, while the green color implicates the neutral electrostatic potential. **Figure 6** illustrates the electron density isosurface mapped with the electrostatic potential surface for the complexes selected in this study. As can be seen from the MEP map of these complexes, while the regions

PSO$\cdots$Cu^{2+} AC$\cdots$Cu^{2+}
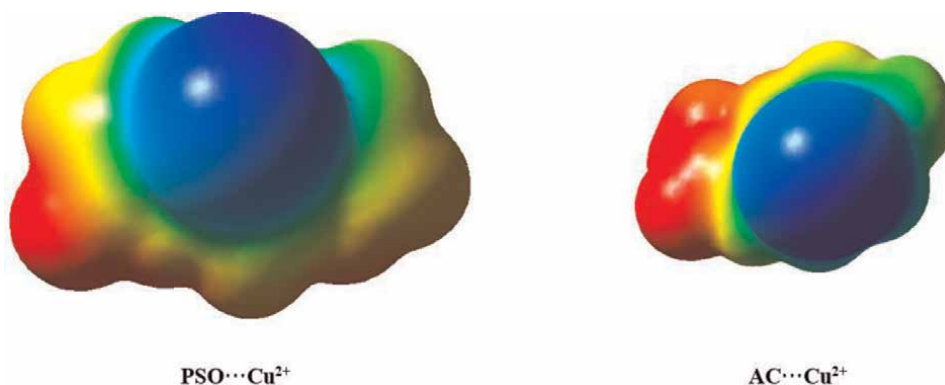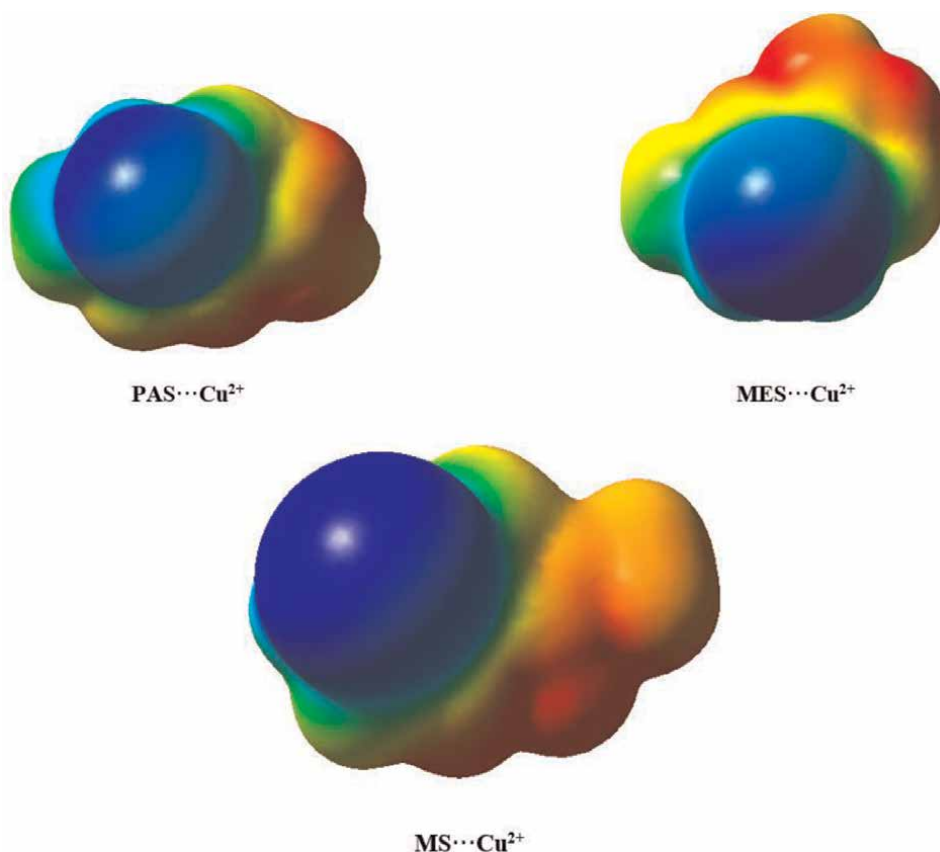
Figure 6.
Electron density isosurface for PSO, AC, PAS, MES and MS complexes calculated by wB97XD method and 6-311 ++G(d,p) basis set.

having the negative potential are over the oxygen electronegative atoms (red and yellow colors), the regions having the positive potential are over the Cu^{2+} cation and the benzene ring plane (blue color).

4. Conclusion

In this study, the influence of NCIs on the complexes formed by the various biomolecules (MES, PAS, AC, PSO, and MS) with the Cu^{2+} cation is investigated using the DFT method. The results show that the absolute values of $\Delta E_{ion-\pi}$ are arranged in MES > PAS > AC > PSO > MS order. It is obvious that these values decrease with going from the gas phase to the solution. For the studied complexes in water solvent, the E_{stab} of MS complex is the highest and the lowest value is related to the PAS complex. From the HOMA results, it can be understood that the greater stability of the complexes in the water solvent is due to their more electron delocalization in this solvent. Contrary to the calculated binding energies, it can be seen that the values of $\rho(r)$, $\nabla^2\rho(r)$, and the donor-acceptor energy increase on passing from the gas phase to

the solution. The formation of HB in the complexes is confirmed with the presence of a bond critical point between the hydrogen atom of donor group and the acceptor atom. The strongest HB is related to the PAS complex, and the E_{HBs} obtained for the MES and MS complexes are close to each other. Furthermore, the values of $\nabla^2\rho(r) > 0$ and $H(r) < 0$ show that the HB interaction of the complexes is in the category of medium HBs. Our data also display that the greatest values of $E^{(2)}$ are related to the gas phase, while the smallest values correspond to the water solvent. The trend of these results is similar to the obtained HB energies. The frontier molecular orbital analysis shows that the hardest and the most stable system belongs to the MS complex, while the softest and the most reactive system corresponds to the PSO complex.

Acknowledgements

Conflict of interest

The author has no conflict of interest.

Abbreviations

DFT	density functional theory
AIM	atoms in molecules
NBO	natural bond orbital
PAS	para-aminosalicylic acid
MES	mesalazine
MS	methyl salicylate
PSO	psoralen
AC	acetaminophen
COX	cyclooxygenase
NCIs	non-covalent interactions
Cu	copper
PCM	polarizable continuum model
BSSE	basis set superposition error
HOMA	harmonic oscillator model of aromaticity
HOMO	highest occupied molecular orbital
LUMO	lowest unoccupied molecular orbital
IMHB	intramolecular hydrogen bond
BCP	bond critical point
FMO	Frontier molecular orbital
MEP	molecular electrostatic potential

Author details

Azadeh Khanmohammadi
Department of Chemistry, Payame Noor University, Tehran, Iran

*Address all correspondence to: az_khanmohammadi@yahoo.com

IntechOpen

References

[1] Stuart MC, Kouimtzi M, Hill SR, editors. WHO Model Formulary. Geneva: Department of Essential Medicines and Pharmaceutical Policies World Health Organization; 2008

[2] Alirezapour F, Khanmohammadi A. Computational study of noncovalent interactions within the various complexes of para aminosalicylic acid and Cr^{2+}, Mn^+, Fe^{2+}, Co^+, Ni^{2+}, Cu^+, Zn^{2+} cations: Exploration of the enhancing effect of the cation–π interaction on the intramolecular hydrogen bond. Theoretical Chemistry Accounts. 2020;**139**:180

[3] Mohammadi M, Alirezapour F, Khanmohammadi A. DFT calculation of the interplay effects between cation–π and intramolecular hydrogen bond interactions of mesalazine drug with selected transition metal ions (Mn^+, Fe^{2+}, Co^+, Ni^{2+}, Cu^+, Zn^{2+}). Theoretical Chemistry Accounts. 2021;**140**:104. DOI: 10.1007/s00214-021-02813-1

[4] Fox W, Ellard GA, Mitchison DA. Studies on the treatment of tuberculosis undertaken by the British Medical Research Council tuberculosis units, 1946-1986, with relevant subsequent publications. The International Journal of Tuberculosis and Lung Disease. 1999;**3**:S231-S279

[5] Rubin G, Hungin APS, Chinn D, Dwarakanath AD, Green L, Bates J. Long-term aminosalicylate therapy is under-used in patients with ulcerative colitis: A cross-sectional survey. Alimentary Pharmacology & Therapeutics. 2002;**16**:1889-1893

[6] Iacucci M, de Silva S, Ghosh S. Mesalazine in inflammatory bowel disease: A trendy topic once again? Canadian Journal of Gastroenterology & Hepatology. 2010;**24**:127-133

[7] Pirgheibi M, Mohammadi M, Khanmohammadi A. A comparative study of interplay effects between the cation-π and intramolecular hydrogen bond interactions in the various complexes of methyl salicylate with Mn^+, Fe^{2+}, Co^+, Ni^{2+}, Cu^+, and Zn^{2+} cations. Structural Chemistry. 2021;**32**:1529-1539. DOI: 10.1007/s11224-021-01728-8

[8] Pirgheibi M, Mohammadi M, Khanmohammadi A. Density functional theory study of the interplay between cation–π and intramolecular hydrogen bonding interactions in complexes involving methyl salicylate with Li^+, Na^+, K^+, Be^{2+}, Mg^{2+}, Ca^{2+} cations. Computational & Theoretical Chemistry. 2021;**1198**:113172. DOI: 10.1016/j.comptc.2021.113172

[9] Bohr V, Nielsen PE. Psoralen-DNA crosslink repair in human lymphocytes: Comparison of alkaline elution with electron microscopy. Biochimica et Biophysica Acta (BBA)—Gene Structure and Expression. 1984;**783**:183-186. DOI: 10.1016/0167-4781(84)90012-5

[10] Mohammadi M, Mahinian M, Khanmohammadi A. Theoretical study of stability and electronic characteristics in various complexes of psoralen as an anticancer drug in gas phase, water and CCl4 solutions. Chemical Research in Chinese Universities. 2022. DOI: 10.1007/s40242-022-1475-5

[11] Wu Q, Christensen LA, Legerski RJ, Vasquez KM. Mismatch repair participates in error-free processing of DNA interstrand crosslinks in human cells. European Molecular Biology Organization Reports. 2005;**6**(6):551-557. DOI: 10.1038/sj.embor.7400418

[12] McKay GA, Walters MR. Clinical Pharmacology and Therapeutics. Hoboken: Wiley; 2013

[13] Mohammadi M, Khanmohammadi A. Molecular structure, QTAIM and bonding character of cation–π interactions of mono- and divalent metal cations (Li^+, Na^+, K^+, Be^{2+}, Mg^{2+} and Ca^{2+}) with drug of acetaminophen. Theoretical Chemistry Accounts. 2019;**138**:101. DOI: 10.1007/s00214-019-2492-4

[14] Mohammadi M, Khanmohammadi A. Theoretical investigation on the non-covalent interactions of acetaminophen complex in different solvents: Study of the enhancing effect of the cation–π interaction on the intramolecular hydrogen bond. Theoretical Chemistry Accounts. 2020;**139**:141. DOI: 10.1007/s00214-020-02650-8

[15] Burley SK, Petsko GA. Aromatic-aromatic interaction: A mechanism of protein structure stabilization. Science. 1985;**229**:23-28. DOI: 10.1126/science.3892686

[16] Lehn JM. Supramolecular Chemistry: Concepts and Perspectives. New York: VCH; 1995

[17] Gilli G, Gilli P. The Nature of Hydrogen Bond. New York: Oxford University Press; 2009

[18] Gallivan JP, Dougherty DA. Cation-π interactions in structural biology. Proceedings of the National Academy of Sciences of the United States of America. 1999;**96**:9459-9464

[19] Ma JC, Dougherty DA. The cation–π interaction. Chemical Reviews. 1997;**97**:1303-1324

[20] Tsuzuki S, Yoshida M, Uchimaru T, Mikami M. The origin of the cation/π interaction: The significant importance of the induction in Li^+ and Na^+ complexes. The Journal of Physical Chemistry A. 2001;**105**:769-773. DOI: 10.1021/jp003287v

[21] Gallivan JP, Dougherty DA. A computational study of cation−π interactions vs salt bridges in aqueous media: Implications for protein engineering. Journal of the American Chemical Society. 2000;**122**:870-874. DOI: 10.1021/ja991755c

[22] Pletneva EV, Laederach AT, Fulton DB, Kostic NM. The role of cation-π interactions in biomolecular association. Design of peptides favoring interactions between cationic and aromatic amino acid side chains. Journal of the American Chemical Society. 2001;**123**:6232-6245. DOI: 10.1021/ja010401u

[23] Shi ZS, Olson CA, Bell AJ, Kallenbach NR. Stabilization of α-helix structure by polar side-chain interactions: Complex salt bridges, cation–π interactions, and C–H ... O H-bonds. Biopolymers. 2001;**60**:366-380

[24] Berthon G, editor. Handbook of Metal-Ligand Interactions in Biological Fluids. New York: Marcel Dekker; 1995

[25] Sousa C, Cebolla A, de Lorenzo V. Enhanced metalloadsorption of bacterial cells displaying poly-His peptides. Nature Biotechnology. 1996;**14**:1017-1020. DOI: 10.1038/nbt0896-1017

[26] Nawaz M, Hisaindee S, Graham JP, Rauf MA, Saleh N. Synthesis and spectroscopic properties of pyridones—Experimental and theoretical insight. Journal of Molecular Liquids. 2014;**193**:51-59. DOI: 10.1016/j.molliq.2013.12.033

[27] Dutta A, Boruah B, Saikia PM, Dutta RK. Stabilization of diketo tautomer of curcumin by premicellar cationic surfactants: A spectroscopic, tensiometric and TD-DFT study. Journal of Molecular Liquids. 2013;**187**:350-358. DOI: 10.1016/j.molliq.2013.09.005

[28] Zhang N, Ayral-Kaloustian S, Nguyen T, Hernandez R, Beyer C. 2-Cyanoaminopyrimidines as a class of antitumor agents that promote tubulin polymerization. Bioorganic & Medicinal Chemistry Letters. 2007;**17**:3003-3005. DOI: 10.1016/j.bmcl.2007.03.070

[29] Lanier MC, Feher M, Ashweek NJ, Loweth CJ, Rueter JK, Slee DH, et al. Selection, synthesis, and structure–activity relationship of tetrahydropyrido [4,3-d]pyrimidine-2,4-diones as human GnRH receptor antagonists. Bioorganic & Medicinal Chemistry. 2007;**15**:5590-5603. DOI: 10.1016/j.bmc.2007.05.029

[30] Howell JMC, Gawthorne JM. Copper in Animals and Man. 1st ed. Boca Raton, FL: CRC Press; 1987

[31] Rayan AM, Ahmed MM, Barakat MH, Abdelkarim AT, El-Sherif AA. Complex formation of cetirizine drug with bivalent transition metal (II) ions in the presence of alanine: Synthesis, characterization, equilibrium studies, and biological activity studies. Journal of Coordination Chemistry. 2015;**68**:678-703. DOI: 10.1080/00958972.2014.994513

[32] El-Sherif AA, Aljahdali MS. Review: Protonation, complex-formation equilibria, and metal–ligand interaction of salicylaldehyde Schiff bases. Journal of Coordination Chemistry. 2013;**66**:3423-3468. DOI: 10.1080/00958972.2013.839027

[33] El-Sherif AA. Synthesis and characterization of some potential antitumor palladium(II) complexes of 2-aminomethylbenzimidazole and amino acids. Journal of Coordination Chemistry. 2011;**64**:2035-2055. DOI: 10.1080/00958972.2011.587004

[34] Alomar K, Landreau A, Kempf M, Khan MA, Allain M, Bouet G. Synthesis, crystal structure, characterization of zinc (II), cadmium(II) complexes with 3-thiophene aldehyde thiosemicarbazone (3TTSCH). Biological activities of 3TTSCH and its complexes. Journal of Inorganic Biochemistry. 2010;**104**:397-404. DOI: 10.1016/j.jinorgbio.2009.11.012

[35] Joseph J, Nagashri K, Janaki GB. Novel metal based anti-tuberculosis agent: Synthesis, characterization, catalytic and pharmacological activities of copper complexes. European Journal of Medicinal Chemistry. 2012;**49**:151-163. DOI: 10.1016/j.ejmech.2012.01.006

[36] Agotegaray MA, Dennehy M, Boeris MA, Grela M, Burrow RA, Quinzani OV. Therapeutic properties, SOD and catecholase mimetic activities of novel ternary copper(II) complexes of the anti-inflammatory drug Fenoprofen with imidazole and caffeine. Polyhedron. 2012;**34**:74-83. DOI: 10.1016/j.poly.2011.12.005

[37] Frisch M, Trucks G, Schlegel H, Scuseria G, Robb M, Cheeseman J, et al. Gaussian 09. Revision D. 01. Wallingford, CT: Gaussian Inc, USA; 2009

[38] Hehre WJ, Radom L, Schleyer PV, Pople JA. Ab Initio Molecular Orbital Theory. New York: Wiley; 1986

[39] Foresman JB, Frisch A. Exploring Chemistry with Electronic Structure Methods. 2nd ed. Pittsburgh, PA: Gaussian, Inc; 1996

[40] Tomasi J, Cammi R, Mennucci B, Cappelli C, Corni S. Molecular properties in solution described with a continuum solvation model. Physical Chemistry Chemical Physics. 2002;**4**:5697-5712. DOI: 10.1039/B207281P

[41] Boys SF, Bernardi F. The calculation of small molecular interactions by the differences of separate total energies. Some procedures with reduced errors. Molecular Physics. 1970;**19**:553-566. DOI: 10.1080/00268977000101561

[42] Bader RFW. Atoms in Molecules: A Quantum Theory. Oxford: Oxford University Press; 1990

[43] Reed AE, Curtiss LA, Weinhold F. Intermolecular interactions from a natural bond orbital, donor-acceptor viewpoint. Chemical Reviews. 1988;**88**: 899-926

[44] BieglerKönig F, Schönbohm J. Update of the AIM2000-program for atoms in molecules. Journal of Computational Chemistry. 2002;**23**: 1489-1494. DOI: 10.1002/jcc.10085

[45] Glendening ED, Reed AE, Carpenter JE, Weinhold F. NBO. Pittsburg, CT: Gaussian, Inc; 2003

[46] Krygowski TM. Crystallographic studies of inter- and intramolecular interactions reflected in aromatic character of π-electron systems. Journal of Chemical Information and Computer Sciences. 1993;**33**:70-78. DOI: 10.1021/ci00011a011

[47] Krygowski TM, Cyranski MK. Separation of the energetic and geometric contributions to the aromaticity of π-electron carbocyclics. Tetrahedron. 1996;**52**:1713-1722

[48] Espinosa E, Molins E. Retrieving interaction potentials from the topology of the electron density distribution: The case of hydrogen bonds. The Journal of Chemical Physics. 2000;**113**:5686-5694. DOI: 10.1063/1.1290612

[49] Abramov YA. On the possibility of kinetic energy density evaluation from the experimental electron-density distribution. Acta Crystallography Sector A. 1997;**53**:264-272

[50] Khanmohammadi A, Mohammadi M. Theoretical study of various solvents effect on 5-fluorouracil-vitamin B3 complex using PCM method. Journal of the Chilean Chemical Society. 2019;**64**:4337-4344. DOI: 10.4067/s0717-97072019000104337

[51] Parra RD, Ohlssen J. Cooperativity in intramolecular bifurcated hydrogen bonds: An ab initio study. The Journal of Physical Chemistry A. 2008;**112**: 3492-3498. DOI: 10.1021/jp711956u

[52] Ziołkowski M, Grabowski SJ, Leszczynski J. Cooperativity in hydrogen-bonded interactions: Ab initio and "atoms in molecules" analyses. The Journal of Physical Chemistry A. 2006;**110**:6514-6521. DOI: 10.1021/jp060537k

[53] Chattaraj PK, Poddar A. Molecular reactivity in the ground and excited electronic states through density-dependent local and global reactivity parameters. The Journal of Physical Chemistry A. 1999;**103**:8691-8699. DOI: 10.1021/jp991214+

[54] Pearson RG. Chemical Hardness-Applications from Molecules to Solids. Weinheim: VCH-Wiley; 1997

[55] Parr RG, Szentpály LV, Liu S. Electrophilicity index. Journal of the American Chemical Society. 1999;**121**: 1922-1924. DOI: 10.1021/ja983494x

[56] Sen KD, Jorgensen CK. Electronegativity, Structure and Bonding. New York: Springer; 1987

[57] Koopmans T. Über die Zuordnung von Wellenfunktionen und Eigenwerten zu den einzelnen Elektronen eines

atoms. Physica. 1933;**1**:104-113. DOI: 10.1016/S0031-8914(34)90011-2

[58] Zhan CG, Nichols JA, Dixon DA. Ionization potential, electron affinity, electronegativity, hardness, and electron excitation energy: Molecular properties from density functional theory orbital energies. The Journal of Physical Chemistry A. 2003;**107**:4184-4195

[59] Arjunan V, Devi L, Subbalakshmi R, Rani T, Mohan S. Synthesis, vibrational, NMR, quantum chemical and structure-activity relation studies of 2-hydroxy-4-methoxyacetophenone. Spectrochimica Acta Part A: Molecular and Biomolecular Spectroscopy. 2014;**130**:164-177. DOI: 10.1016/j.saa.2014.03.121

Chapter 6

Additive Manufacturing of Pure Copper: Technologies and Applications

Tobia Romano and Maurizio Vedani

Abstract

The opportunity to process pure copper through additive manufacturing has been widely explored in recent years, both in academic research and for industrial uses. Compared to well-established fabrication routes, the inherent absence of severe design constraints in additive manufacturing enables the creation of sophisticated copper components for applications where excellent electrical and thermal conductivity is paramount. These include electric motor components, heat management systems, heat-treating inductors, and electromagnetic devices. This chapter discusses the main additive manufacturing technologies used to fabricate pure copper products and their achievable properties, drawing attention to the advantages and the challenges they have to face considering the peculiar physical properties of copper. An insight on the topic of recycling of copper powders used in additive manufacturing is also provided. Finally, an overview of the potential areas of application of additively manufactured pure copper components is presented, highlighting the current technological gaps that could be filled by the implementation of additive manufacturing solutions.

Keywords: additive manufacturing, copper, powder bed fusion, green laser, binder jetting, heat exchangers

1. Introduction

Pure copper is one of the most widely employed materials in electronic, electromagnetic, and heat management applications because it combines superior electrical and thermal properties with high workability and solderability [1]. In recent years, the great advances in additive manufacturing (AM) technologies have shown the ability to create tortuous geometries inconceivable with traditional production methods. AM of pure copper has attracted the interest of both academic and industrial researchers because it now enables the fabrication of complex-shaped components, including novel-design antennas, inductors, radiators, and heat exchangers, with improved performance through topology optimization based on the specific requirements of the application considered.

AM technologies for the processing of pure copper can be roughly classified into powder bed-based and direct deposition technologies. In the first case, the powder is gradually deposited in successive layers and selectively consolidated using an energy source or a polymeric binder. At the end of the printing process, the part is surrounded by the unconsolidated powder bed, from which it is extracted for any subsequent processing steps. On the other hand, in direct deposition processes the material feedstock in powder or wire form is deposited according to the targeted geometry by a printing head (e.g., a laser torch) that enables material delivery and provides the heat required for its consolidation. AM of copper has been studied predominantly in the context of powder bed-based technologies rather than direct energy deposition (DED) methods because they provide higher dimensional accuracy and tolerances [2]. This is of major importance when building tiny intricate features, such as curved channels or lattice structures in complex heat exchangers. On the other hand, flexible DED systems, which use a robotic arm equipped with a nozzle for material dispensing, can more easily create multi-material parts with added functionalities, as each material can be conveniently deposited where needed. This would allow the one-step fabrication of components constituted by dissimilar materials, such as copper and steel, which currently can only be made by other routes through repeated joining operations with high costs and long lead times [3].

2. Additive manufacturing technologies for pure copper processing

Various classes of AM technologies have been employed to successfully fabricate pure copper parts. However, significant processing challenges related to the physical properties of copper and the difficulty of achieving full density in the final parts still represent challenging issues that should be thoroughly investigated for these methods to become established.

2.1 Laser powder bed fusion

Laser powder bed fusion (LPBF) is the most established AM technology for the processing of metallic materials [4]. It uses a laser source to selectively melt the powder spread by a roller system to generate a bed of controlled thickness. Once a laser scan is completed, the build platform is lowered by a distance equal to the layer thickness set for the process, and a new layer of powder is deposited. The process is then repeated layer by layer to build the desired geometry based on the designed STL model. All the procedure is carried out in a closed chamber filled with inert gas to avoid material contamination. The typical setup of LPBF is schematically illustrated in **Figure 1**.

A large number of process variables influence the quality of parts produced by LPBF [5]. Fine powders with an average particle size lower than 50 μm are typically employed [6–8] to allow the generation of thin layer thicknesses, leading to improved resolution and reduced staircase effects, which result in a better surface finish. A major role is also played by the characteristics of the laser and how the material interacts with it. Commercial LPBF machines are normally equipped with infrared laser sources with a wavelength of around 1 μm and power up to 500 W [9]. Although the effective absorbance of the powder bed in LPBF is higher than in bulk materials due to the multiple laser reflections induced by the closely spaced powder particles, it hardly exceeds 30% when processing pure copper powders with infrared lasers [10].
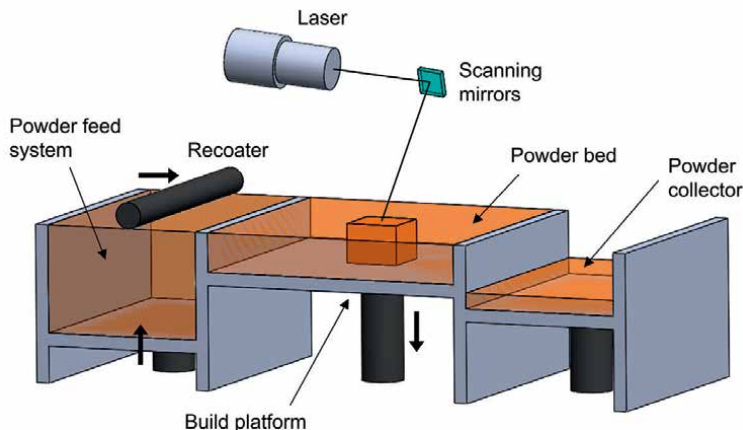
Figure 1.
Schematic layout of the LPBF process.
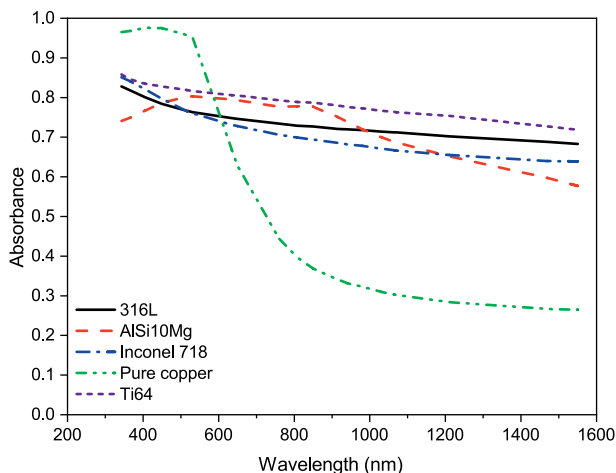
Figure 2.
Absorbance of metal powders in LPBF as a function of laser wavelength. Data extracted from Brandau et al. [10].

This is clearly shown in **Figure 2**, which compares the absorbance of some of the most common metal powders used in LPBF. The poor absorption of the laser energy during the printing process causes incomplete fusion of the powder material. The result is a substantial residual porosity that affects the thermal and electrical performance of the components.

Two main approaches have been adopted to overcome this issue. On the one hand, some researchers [9, 11, 12] have employed high-power infrared lasers combined with low-scanning speeds to ensure complete melting of the powder material despite low absorption. Although relative densities exceeding 99% have been reported, the processing window available for parameter setting is very narrow, and it is difficult to sustain a stable melt track when such high powers are involved, resulting in lower resolution and poor surface finish. Also, the large amount of energy wasted during the printing process leads to high production costs, and the low-scanning speed

results in long lead times. The other strategy relies on the use of blue or green lasers with wavelengths of 450 and 515 nm, respectively, for which copper exhibits a higher absorption rate (**Figure 2**). TRUMPF (Germany) recently launched the first series of commercial LPBF machines equipped with a 515 nm wavelength laser for the manufacturing of copper parts [13]. Gruber et al. [14] achieved almost full density and electrical conductivity of 100% IACS in pure copper samples produced with the green laser-based process.

2.2 Electron beam powder bed fusion

Electron beam powder bed fusion (EB-PBF) features a fabrication approach similar to LPBF but uses a high-energy electron beam as the heat source to selectively melt the powder material. The printing process is conducted inside a high-vacuum chamber to prevent electrons from scattering by collision with gas molecules. A schematic representation of the machine setup is illustrated in **Figure 3**.

Although its use has been limited to date due to a relatively lower number of systems available in industrial and academic research centers, the main advantage of EB-PBF for the processing of pure copper, as compared to its laser-based counterpart, is that the energy absorbed from the incident electrons is not affected by the optical reflectivity of the target material. This leads to highly efficient energy transfer during the printing operation (a rate of absorption of around 80% is estimated [15]). In addition, the high-vacuum environment protects the material from oxidation, ensuring high purity of the final parts.

One well-known issue of EB-PBF is the so-called smoking. Due to the incident electrons, a negative charge tends to accumulate at the surface of particles in the powder bed. The mutual repulsion among neighboring particles may cause them to suddenly jump from the powder bed, generating a cloud of powder inside the work chamber, which may impair the smooth processing of the material [16, 17]. Smoking is not a primary issue in the case of pure copper since its high electrical conductivity can prevent the buildup of a strong negative charge. Still, slightly coarser powders than in LPBF are generally used (in the range of 60–105 μm [15, 18, 19]) because they have a lower tendency to smoking compared to fine powders [17]. Also, each powder
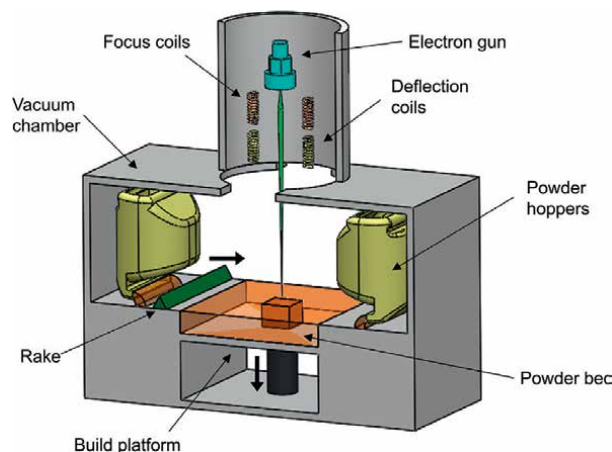
Figure 3.
*Schematic layout of the EB-PBF process.*

layer is preheated around 400–500°C [18] and partially sintered by the beam itself before the actual scanning operation to provide an even improved electrical connection for electrostatic charge dissipation. One difficulty that arises from the high temperatures at which the deposited material is maintained is that copper particles tend to stick together during the raking operation owing to their high propensity to sinter. Particle clusters may impede the correct deposition of the following powder layers, possibly causing interlayer defects. Also, particles that are partially sintered on the external surface of the as-print parts generate a relatively high surface roughness [18]. The electron beam has a relatively large spot size of about 0.5 mm [20], while beams 30–100 μm in diameter are typically used in LPBF [21]. This restricts the capability of EB-PBF of producing minute details in complex parts, which is a nontrivial limitation, for example, in the fabrication of sophisticated heat exchangers made with pure copper. However, higher production rates can be achieved compared to LPBF because preheating, combined with the more effective energy input, ensures complete powder melting even when selecting high beam scanning speeds during the printing process [19].

Few studies [15, 18, 22] have been conducted so far to identify the main variables that affect the quality and reliability of pure copper parts produced by EB-PBF with commercial machines. Feedstock quality, preheating temperature, beam focal point, and scanning strategy are among the parameters that need to be optimized to ensure a robust production with consistent characteristics across runs. Guschlbauer et al. [15] obtained pure copper specimens with a relative density above 99.5% by conveniently combining the beam power and the scanning speed within the ranges 275–750 W and 250–1500 mm/s, respectively.

2.3 Binder jetting

Binder jetting shares with PBF technologies the powder bed strategy for the creation of three-dimensional parts. However, during the printing process, the powder particles are glued together by water- or solvent-based polymeric binder selectively deposited by a print head instead of being melted by a high-energy beam. A curing treatment at moderate temperature is then applied to eliminate the volatile fraction of the binder and induce polymerization. The reticulated polymer provides the green part with sufficient strength to be removed from the unbound powder bed without breaking. The part is finally subjected to a debinding and sintering cycle to burn off the polymer fraction and densify the material by diffusion-assisted mechanisms promoted by the high temperature. Although there exist several sintering strategies for both metallic and ceramic materials, which may involve for instance the formation of a liquid phase to facilitate interparticle bonding, in the case of pure copper densification is achieved by solid-state diffusion only because no low-melting second phases are present. As-sintered parts normally possess a relatively high surface roughness, especially on vertical surfaces due to the effect of the distinct powder layers they are made of [23]. Postprocessing operations involving vibratory abrasion and chemical treatments [24] may be required to achieve a good surface finish in components with complex geometry and internal features. The flowchart of the binder jetting process is illustrated in **Figure 4**.

Feedstock powders with an average size exceeding 20 μm are normally preferred in binder jetting because their relatively low tendency to agglomerate facilitates the spreading operation [25]. However, the development of vibrating devices for powder sieving and dispensing has enabled the use of finer powders with an average size
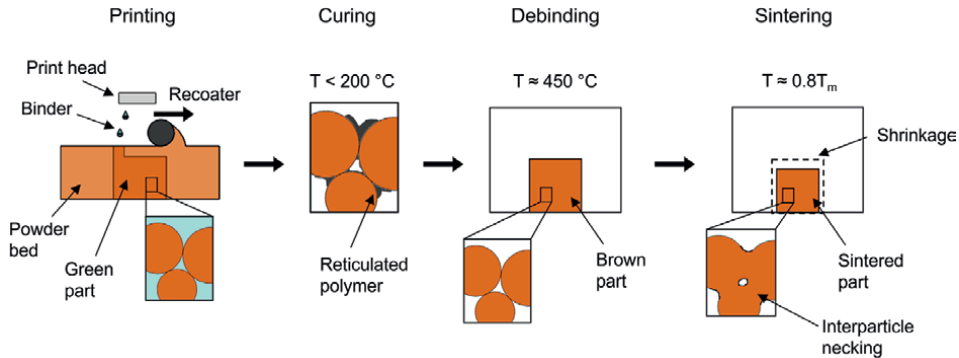
Figure 4.
Schematic flowchart of the binder jetting process.

lower than 5 µm [26, 27] for improved resolution and densification. Bimodal mixtures also showed the potential to improve powder flowability and reduce part shrinkage upon sintering, because particles with different sizes can tightly pack and result in high green part density [28].

The peculiar feature of binder jetting compared to the above-described PBF technologies is that the generation of the three-dimensional geometry and the bonding between powder particles occur in two distinct stages. In addition to those already mentioned, one challenge LPBF faces in processing pure copper is related to its high thermal conductivity. The heat provided by the energy source is rapidly dissipated by the surrounding material. This may cause poor interlayer adhesion and lead to delamination defects in the produced part. Binder jetting does not suffer from this phenomenon, because the material is homogeneously heated in a controlled environment by applying a proper sintering cycle.

Investigation on binder jetting of pure copper showed that the primary challenges consist of attaining complete density and high purity in the sintered parts. The powder particles in the green parts have a low tendency to sinter because they are covered by a low surface energy oxide layer and are not tightly compacted by the recoater during the printing process. Both the surface oxide layer and the large interparticle distance hamper neck formation and growth between neighboring powder particles by solid-state diffusion [25, 29]. In addition, carbon residues may result from incomplete combustion of the polymeric binder during the debinding stage [27], and uneven sintering may occur between the outer and the core regions of the parts due to temperature gradients along the material thickness. Indeed, the rapid stiffening of the outer zones exposed to a higher temperature may hinder inward shrinkage, thus leaving a central volume with a high residual porosity [27]. Therefore, the sintering parameters need to be carefully adjusted in terms of sintering atmosphere, heating ramp, peak temperature, and sintering time to minimize the residual porosity and carbon impurities, which adversely affect the mechanical, thermal, and electrical properties of the final parts [30, 31].

From a design perspective, binder jetting does not require support structures for overhanging features, because the powder bed itself serves as a support. In addition, several parts can be stacked in the vertical direction, allowing the entire volume of the working chamber to be utilized to print large series of parts [32, 33] that can then all be sintered in a single furnace cycle. However, the possible effects of creep activated

by the prolonged exposure to high temperatures during sintering need to be taken into account to avoid undesirable deformations of cantilever elements in the final components [34]. In addition, parts shrink as a result of densification. Because back-to-back powder layers are not well consolidated due to limited binder penetration, a larger amount of porosity is observed among them than within individual layers. This causes a larger shrinkage along the build direction than in the lateral directions upon sintering, which is further accentuated by gravity effects [29]. Therefore, a careful design is needed to compensate for these differential changes in the part dimensions upon sintering.

2.4 Laser metal deposition

Laser metal deposition (LMD) belongs to the family of DED processes. It utilizes a coaxial nozzle equipped with a laser source to melt the feedstock material, while it is simultaneously deposited in a series of weld tracks to generate the designed three-dimensional geometry. A carrier gas transports the powder through the outermost annular channel to the melting zone, while a shielding gas is used to avoid excessive oxygen pickup by the melt pool. The use of copper powders with size ranging from 30 to 110 μm have been reported in the literature [35–38]. The setup of the LMD process is schematically illustrated in **Figure 5**.

The main advantages of LMD over powder bed-based technologies are the high productivity and flexibility, the ability to work without closed chambers with protected environment, and the possibility to add features to the existing part. Also, machining tools can be integrated into the printing system to enable hybrid manufacturing [39]. The multi-axis configuration allows the construction of three-dimensional elements even on non-flat surfaces.

LMD is not commonly employed to fabricate individual components from pure copper because it cannot provide the dimensional accuracy and resolution usually required for its typical applications (e.g., heat exchangers, inductors, and electromagnetic devices). In addition, the shielding gas can only partially prevent oxidation [39]. Oxides reduce the wettability of molten copper on solid surfaces [40], leading to poor adhesion between the substrate and the built features.

A great impetus to LMD of pure copper has been given by the recent introduction of green and blue laser sources, for which copper displays a relatively high absorptivity.
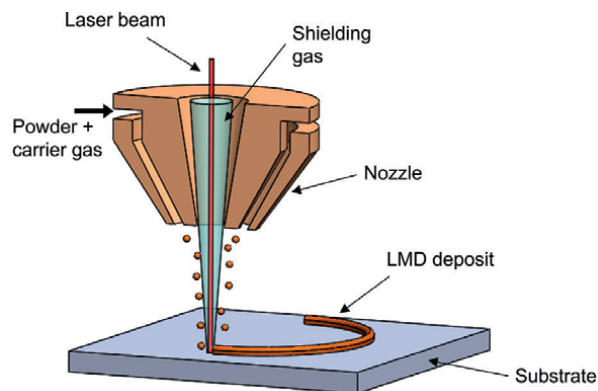
Figure 5.
Schematic layout of the LMD process.

Higher process control can thus be achieved and lower powers are required compared to conventional infrared lasers, ranging from 200 W to 1 kW for green laser sources depending on the physical properties of the substrate material [41] and lower than 87 W for blue diode lasers [35, 36]. However, the real strength of LMD compared to powder-bed technologies is that it enables the relatively easy fabrication of multi-material parts. In principle, different materials can be conveniently placed at specific locations by simply replacing and/or mixing the powder fed during the building process. Therefore, properties such as hardness, thermal and electrical conductivity, or corrosion resistance can be fine-tuned throughout a single component by conveniently customizing its constituent materials.

Copper has been investigated in the context of multi-material LMD mainly in combination with steel. The coupling of copper and tool steels has been proposed to fabricate molds and dies with improved cooling efficiency due to the high thermal conductivity of the copper portion [37, 42]. The more uniform and faster heat extraction would increase both the quality of the formed parts and the productivity. Multi-materials based on copper and stainless steel, on the other hand, may find use in highly demanding applications such as fusion reactors and high-field pulsed magnets [43]. However, the manufacturing of such structures still has to face significant challenges due to the discrepancy in laser absorption, thermal conduction, and thermal expansion behavior between copper and steel and their poor mutual solubility.

3. Recycling of pure copper powders in additive manufacturing

High flowability and chemistry control are key requirements for metallic powders for AM. Gas atomization is normally employed to produce powders for AM, because it can provide higher sphericity, smoother surface morphology, and tighter control of the particle size distribution and the chemical composition, particularly in terms of oxygen content, compared to other processes such as water atomization [44]. Pure copper powders for AM are generally produced from oxygen-free electronic (OFE), oxygen-free, and electrolytic tough pitch (ETP) grades to provide feedstocks with low impurity content despite the tendency to oxidation caused by the large surface area of the fine powder particles [1, 45].

Both the use of high-purity raw materials and the complexity of the gas atomization process result in rather expensive powder feedstocks. While LMD can achieve high material utilization efficiency with optimized process parameters [46], in PBF and binder jetting, most of the powder is used to generate the powder bed. It is a common procedure to collect, sieve, and reuse the excess of feedstock material that is not consolidated during the building process in order to minimize material waste and keep manufacturing costs low. Also, the practice of powder recycling improves the environmental profile of these processes, since gas atomization is a very energy- and material-intensive process [47]. Nevertheless, the powder is normally discarded after a certain number of cycles as it is subjected to various degradation phenomena, depending on the nature of the AM process, which can severely affect the quality of the produced parts. This is particularly critical for materials that are sensitive to oxidation and are used in applications that impose stringent limits on the impurity content, such as pure copper for thermal management and electrical applications.

The complex combination of factors involved in PBF processes can severely affect the quality of copper powders collected after several printing cycles compared to the virgin material. Oxygen pickup occurs due to residual oxygen and moisture in the

work chamber and during part recovery at the end of the printing process [48] when the atmosphere control is turned off. As a result, the thickness of the oxide layer that naturally covers the surface of copper powder particles increases significantly [49]. Surface oxides are not easily removed during the fabrication process and may be incorporated into the final parts, affecting their mechanical, thermal, and electrical performance. Hence the need to reduce the oxygen content of the powder before reuse, typically by heating it in a reducing environment containing forming gas [20]. Speidel et al. [50] have proposed a less expensive and more readily scalable method for treating heavily oxidized copper powders for LPBF, based on chemical etching with a dilute solution of nitric acid.

In binder jetting, the powder in the bed is further subjected to oxidation during the curing stage [27], which is normally carried out in the air. In the case of copper, oxidation is additionally promoted when a water-based binder is employed, as copper is highly sensitive to moisture. Binder splashes may generate massive particle agglomerates in the regions of the powder bed next to the boundaries of the printed parts [51]. Also, the powder particles that remain sticked on the surface of cured parts are usually removed with pressurized air. The applied pressure may deform the highly ductile copper particles [52], reducing their sphericity [51]. However, such particles account for a minimal fraction of the total powder collected at the end of a printing cycle and should not affect the overall powder flowability in the next runs. In **Figure 6**, a comparison between fresh copper powder and the feedstock to be recycled after binder jetting is proposed. No significant morphological differences are observed between the two powder batches.

Sieving is normally conducted to break particle conglomerates and eliminate coarsened and partially sintered particles. However, a significant fraction of fine particles may escape the sieve and is lost by dispersion into the air [51]. This may lead to a nonnegligible shift in the median diameter toward higher values and narrower size distribution, as finer particles are preferentially removed from the feedstock. Therefore, the effect of sieving on powder granulometry should be considered when employing recycled powders in AM. In PBF, processing parameters should be adjusted to account for the varying powder bed density from one cycle to next. In binder jetting, a coarser and narrower powder size distribution results in lower green part density and, consequently, higher shrinkage upon sintering for the same final density. In addition, a higher sintering temperature may be required to attain satisfactory densities, because coarse powder particles have a lower tendency to sinter due to the reduced surface area compared to fine particles [26].
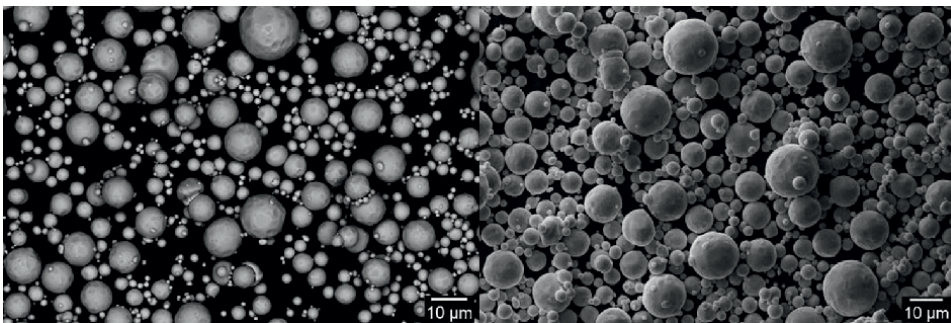
Figure 6.
Copper powder in as-received conditions (left) and collected from the powder bed after binder jetting (right).

4. Applications of additively manufactured pure copper components

In recent years, AM processes have been applied to pure copper, particularly for the manufacturing of high-added-value components for advanced applications in various fields that require excellent thermal and electrical performances. The main barrier to the large-scale adoption of these technologies in the industry is the limited availability of regulations covering the different aspects of AM, including raw material quality, design guidelines, fabrication and postprocessing techniques, material testing, and inspection of the final components. This obliges companies to make considerable efforts in terms of investigation and testing to qualify and certify AM products prior to market launch, which may result in extremely high costs and long lead times [53]. In addition, compared to traditional fabrication methods, AM processes often exhibit poor repeatability and reproducibility [54, 55], and the relationship between manufacturing route, material characteristics, and final product quality still needs to be thoroughly explored [53].

While some standards have already been developed for the AM of metallic materials such as stainless steels and nickel- and titanium-based alloys [53], AM of copper is still in its infancy and is not yet targeted for standardization. However, several examples of additively manufacturing components made of pure copper have already been reported in the literature and in public technical expositions.

4.1 Automotive components

Copper and copper alloys are widely used in the automotive industry to manufacture a variety of vehicle parts, such as electric motor components, ABS and power lock pumps, water and oil coolers, radiators, and heat exchangers for air conditioning [56]. The use of copper in this sector has significantly increased in the past few years with the spread of hybrid and electric vehicles [57].

Pure copper windings and rotors play a key role in the performance of electric motors. Proper winding design optimization can reduce AC and DC loss. However, this is restricted by the limited capability of established manufacturing methods of producing complex geometries with reasonable costs and lead times. Maxwell Motors, a startup based in the USA, recently developed a novel copper winding design to improve the performance of an electric motor that does not use rare-earth-based magnets. They jointly developed and manufactured with ExOne (USA) a monolithic winding assembly by binder jetting, hence obviating the usual steps of manufacturing and welding the individual parts [58]. The same approach can be extended to the fabrication of customized shanks and adaptors for car chassis welding [59].

4.2 Thermal management devices

The high thermal conductivity of pure copper makes it the ideal material for heat dissipation purposes in numerous fields including microelectronics, power plants, and transport. Topological optimization can improve the performance of thermal management devices by maximizing the efficiency of heat transfer. This can be achieved through AM, for instance by building intricate features or even lattice structures with very large specific surface area available for heat exchange [60].
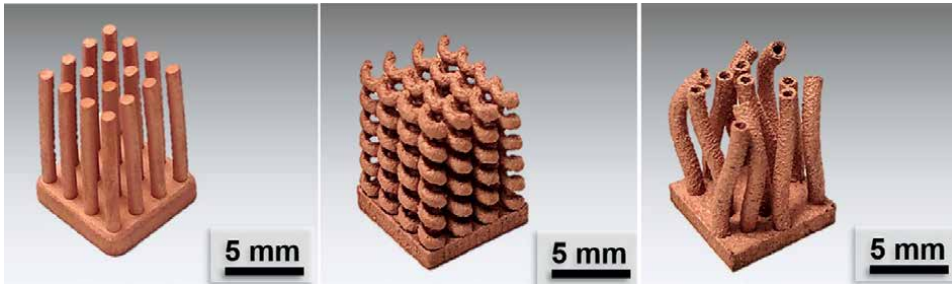
Figure 7.
Columnar (left), helix (center), and bent tube (right) pure copper heat sinks. Adapted from [8].

Constantin et al. [8] fabricated complex-shaped heat sinks consisting of helix and bent-tube structures through LPBF (**Figure** 7). They developed a special experimental setup to evaluate the performance of the additively manufactured heat sinks in comparison with a commercial device featuring a straight columnar structure. Each heat sink was connected to a memory card chip placed on a heater plate and air circulation was provided by a fan. The helix and bent-tube heat sinks exhibited a higher cooling efficiency owing to their larger surface area compared to the commercial device.

Various companies have showcased prototypes of pure copper cooling plates and heat exchangers featuring minute details and mesh structures made by PBF and BJ technologies with optimized processing parameters [61–64].

4.3 Electrical and electromagnetic devices

Due to its remarkable physical properties, pure copper is the preferred material for the fabrication of electrical and electromagnetic devices.

Copper is commonly employed to produce inductors for heat treatments and other hot processes, enabling highly controlled and localized heat delivery to the parts. The shape and size of the coils can be tuned to meet the heat treatment specifications and ensure adequate productivity [65]. Copper inductors are conventionally made by hand-wrapping copper wires on blueprints. Then, individual coils are brazed to match the geometry of the workpiece. This manufacturing route is time-consuming and requires highly skilled labor, resulting in high production costs. Also, the devices have relatively low durability, due to the discontinuities at the brazing joints [66]. On the other hand, monolithic inductors with homogeneous properties could be directly fabricated by AM, resulting in increased productivity and service life. Silbernagel et al. [6] also demonstrated that the cross-section of coils made by LPBF can be conveniently varied to locally control the electrical resistivity. Such inductors may be used in treatments featuring a complex thermal profile or applied to components with variable wall thickness. Hollow structures for cooling fluid circulation can also be produced for applications where particularly high cooling efficiency is required.

The flexibility of AM processes also enables the one-step manufacturing of sophisticated antennas with tunable electromagnetic properties. This would avoid issues, such as uncontrolled shifts in the operating frequency band, which may be caused by imperfect alignment when soldering different pieces. Johnson et al. [67]
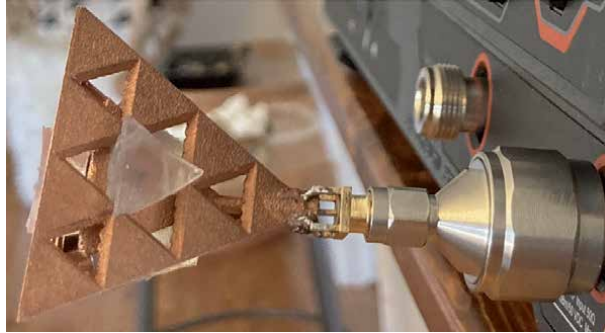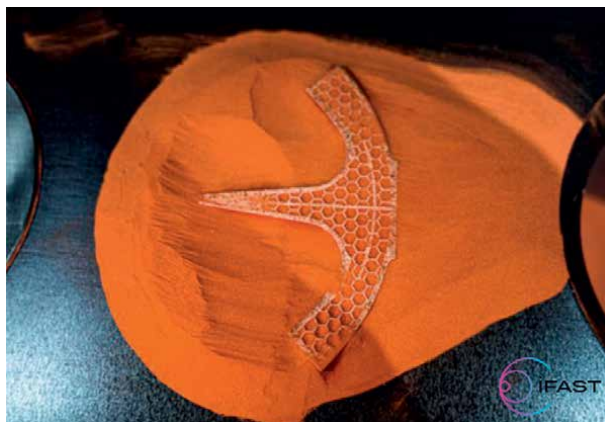
Figure 8.
Pure copper pyramidal fractal antenna made by green laser-based PBF [67].

fabricated a copper pyramidal fractal antenna with an LPBF system equipped with a green laser (**Figure 8**). The radio frequency (RF) performance of the antenna was evaluated with a spectrum analyzer and it was found to be in good agreement with the results of simulations. A novel-design bullhorn antenna made of pure copper has also been manufactured with the high-precision binder jetting technology developed by Digital Metal (Sweden) [64].

4.4 Particle accelerator components

The manufacturing of vacuum devices and particle accelerator components made of pure copper can also benefit from the AM's inherent design freedom and capability of one-step fabrication. Although the market size might appear limited, the sophisticated technologies involved in this sector represent an extremely important test bench for AM development. The layer-by-layer approach of AM technologies facilitates the creation of enclosed envelopes in RF cavities, eliminating the need for sophisticated techniques and highly specialized labor for the assembly of individual parts [66]. This was demonstrated by Mayerhofer et al. [68], who manufactured a monolithic copper RF cavity for a linear accelerator prototype using LPBF. Although the additively manufactured cavity exhibited a slightly lower performance compared to the reference cavity fabricated with conventional methods, the production costs were reduced to a third. Internal channels and lattice structures can also be implemented in RF devices to improve their cooling efficiency, hence eliminating current limitations on the duty cycle and average power [66, 69].

Frigola et al. [69] fabricated a pure copper cathode by EB-PBF and tested it in a RF photoinjector. The performance of the additively manufactured cathode was in line with that of conventionally machined cathodes and it could be further improved by integrating internal cooling channels for liquid helium circulation. Within the frame of the I.FAST project [70], aimed at boosting innovation in the field of particle accelerators, Torims et al. [71] prototyped the quarter sector of a pure copper radio frequency quadrupole (RFQ) by green laser-based LPBF (**Figure 9**). They demonstrated the possibility of rapid manufacturing, avoidance of brazing operations, and improved cooling efficiency offered by AM compared to more restrictive conventional production methods. A full-size four-vane RFQ prototype (**Figure 10**) was recently presented at the 13th International Particle Accelerator Conference (IPAC22) [72].

Figure 9.
Manufacturing of a pure copper RFQ section by LPBF with a green laser source [71].
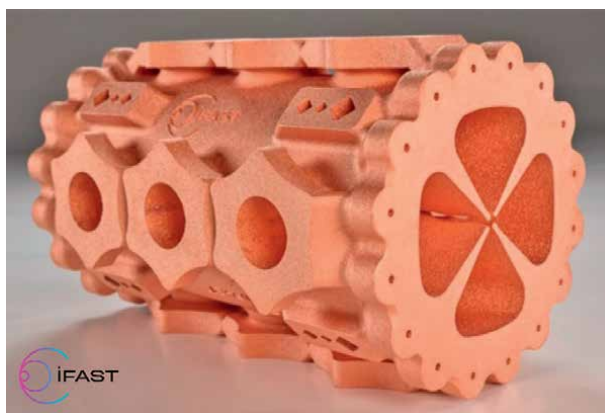
Figure 10.
Additively manufactured pure copper RFQ [72].

5. Conclusion

Additive manufacturing of pure copper has been extensively investigated in the last decade because it has the potential to create complex components with improved thermal and electrical performance. Within this perspective, the component topology can be optimized according to specific needs and requirements, instead of being dictated by the technological constraints imposed by conventional manufacturing methods.

Pure copper has historically been a challenging material to be processed by additive manufacturing. The high reflectivity of pure copper makes the more established laser-based processes difficult to control and energy inefficient. On the other hand, when using an electron beam energy source, high resolution and dimensional accuracy can hardly be achieved due to the relatively large beam spot size and the tendency of copper powder particles to stick on the consolidated surfaces. Binder jetting has also exhibited some drawbacks related to the difficulty in accomplishing adequate density and material purity after sintering.

In the past few years, however, additive manufacturing technologies have made significant progress in the context of pure copper processing. More reliable processes have been developed by optimizing the operating parameters, such as power input, scanning strategy, or sintering setup. In addition, novel robust green and blue laser sources have recently been introduced, for which copper exhibits higher absorption rates. They are expected to extend the stability window for the processing of pure copper so as to create high-quality products competitive with their counterparts produced by more conventional routes.

Several companies and research groups have already showcased a variety of additively manufactured prototypes made of pure copper. These include complex high-added-value components such as heat exchangers, inductors, electromagnetic devices, and motor windings with optimized geometry and tailored functional characteristics. However, the full potential of additive manufacturing still needs to be explored for these methods to truly become an integral part of the industrial supply chain.

Acknowledgements

Conflict of interest

The authors declare no conflict of interest.

Author details

Tobia Romano* and Maurizio Vedani
Department of Mechanical Engineering, Politecnico di Milano, Milan, Italy

*Address all correspondence to: tobia.romano@polimi.it

IntechOpen

References

[1] Davis DJR. ASM Specialty Handbook, Copper and Copper Alloys. ASM Materials Park, OH, USA: ASM International; 2001:3-9. DOI: 10.131/caca2001p003

[2] Gruber S, Grunert C, Riede M, López E, Marquardt A, Brueckner F, et al. Comparison of dimensional accuracy and tolerances of powder bed based and nozzle based additive manufacturing processes. Journal of Laser Applications. 2020;**32**(3):032016. DOI: 10.2351/7.0000115

[3] Pascal C, Chaix JM, Dutt A, Lay S, Allibert CH. Elaboration of (steel/cemented carbide) multimaterial by powder metallurgy. Materials Science Forum. 2007;**534-536**:1529-1532. DOI: 10.4028/www.scientific.net/MSF.534-536.1529

[4] Papadakis L, Chantzis D, Salonitis K. On the energy efficiency of pre-heating methods in SLM/SLS processes. International Journal of Advanced Manufacturing Technologies. 2018;**95**:1325-1338. DOI: 10.1007/s00170-017-1287-9

[5] Hanzl P, Zetek M, Bakša T, Kroupa T. The influence of processing parameters on the mechanical properties of SLM parts. Procedia Engineering. 2015;**100**:1405-1413. DOI: 10.1016/j.proeng.2015.01.510

[6] Silbernagel C, Gargalis L, Ashcroft I, Hague R, Galea M, Dickens P. Electrical resistivity of pure copper processed by medium-powered laser powder bed fusion additive manufacturing for use in electromagnetic applications. Additive Manufacturing. 2019;**29**:1-11. DOI: 10.1016/j.addma.2019.100831

[7] Qu S, Ding J, Fu J, Fu M, Zhang B, Song X. High-precision laser powder bed fusion processing of pure copper. Additive Manufacturing. 2021;**48**:102417. DOI: 10.1016/j.addma.2021.102417

[8] Constantin L, Wu Z, Li N, Fan L, Silvain JF, Lu YF. Laser 3D printing of complex copper structures. Additive Manufacturing. 2020;**35**:101268. DOI: 10.1016/j.addma.2020.101268

[9] Colopi M, Caprio L, Demir AG, Previtali B. Selective laser melting of pure Cu with a 1 kW single mode fiber laser. Procedia CIRP. 2018;**74**:59-63. DOI: 10.1016/j.procir.2018.08.030

[10] Brandau B, Da Silva A, Wilsnack C, Brueckner F, Kaplan AFH. Absorbance study of powder conditions for laser additive manufacturing. Materials and Desing. 2022;**216**:110591. DOI: 10.1016/j.matdes.2022.110591

[11] Ikeshoji TT, Nakamura K, Yonehara M, Imai K, Kyogoku H. Selective laser melting of pure copper. The Journal of The Minerals, Metals & Materials Society (TMS). 2018;**70**(3):396-400. DOI: 10.1007/s11837-017-2695-x

[12] Jadhav SD, Goossens LR, Kinds Y, Van Hooreweder B, Vanmeensel K. Laser-based powder bed fusion additive manufacturing of pure copper. Additive Manufacturing. 2021;**42**:1-15. DOI: 10.1016/j.addma.2021.101990

[13] TruPrint Serie 1000 Green Edition. TRUMPF. Available from: https://www.trumpf.com/en_INT/products/machines-systems/additive-production-systems/truprint-serie-1000-green-edition/. [Accessed: June 1, 2022]

[14] Gruber S, Stepien L, López E, Brueckner F, Leyens C. Physical and

geometrical properties of additively manufactured pure copper samples using a green laser source. Materials. 2021;**14**(13):1-11. DOI: 10.3390/ma14133642

[15] Guschlbauer R, Momeni S, Osmanlic F, Körner C. Process development of 99.95% pure copper processed via selective electron beam melting and its mechanical and physical properties. Materials Characterization. 2018;**143**:163-170. DOI: 10.1016/j.matchar.2018.04.009

[16] Gibson I, Rosen D, Stucker B, Khorasani M. Additive Manufacturing Technologies. 3rd ed. Cham, Switzerland: Springer; 2021. p. 159

[17] Chiba A, Daino Y, Aoyagi K, Yamanaka K. Smoke suppression in electron beam melting of inconel 718 alloy powder based on insulator–metal transition of surface oxide film by mechanical stimulation. Materials. 2021;**14**(16):1-24. DOI: 10.3390/ma14164662

[18] Dadbakhsh S, Zhao X, Kumar P, Shanmugam V, Lin Z, Hulme C. Process and geometrical integrity optimization of electron beam melting for copper. CIRP Annals. 2022;**71**(1):1-4. DOI: 10.1016/j.cirp.2022.03.041

[19] DebRoy T, Wei HL, Zuback JS, Mukherjee T, Elmer JW, Milewski JO, et al. Additive manufacturing of metallic components – Process, structure and properties. Progress in Materials Science. 2018;**92**:112-224. DOI: 10.1016/j.pmatsci.2017.10.001

[20] El-Wardany TI, She Y, Jagdale VN, Garofano JK, Liou JJ, Schmidt WR. Challenges in three-dimensional printing of high-conductivity copper. Journal of Electronic Packaging. 2018;**140**(2):1-12. DOI: 10.1115/1.4039974

[21] Shi W, Liu Y, Shi X, Hou Y, Wang P, Song G. Beam diameter dependence of performance in thick-layer and high-power selective laser melting of Ti-6Al-4V. Materials. 2018;**11**(7):1-17. DOI: 10.3390/ma11071237

[22] Lodes MA, Guschlbauer R, Körner C. Process development for the manufacturing of 99.94% pure copper via selective electron beam melting. Materials Letters. 2015;**143**:298-301. DOI: 10.1016/j.matlet.2014.12.105

[23] Mostafaei A, Elliott AM, Barnes JE, Li F, Tan W, Cramer CL, et al. Binder jet 3D printing — Process parameters , materials , properties, modeling, and challenges. Progress in Materials Science. 2021;**119**:100707. DOI: 10.1016/j.pmatsci.2020.100707

[24] Kumbhar NN, Mulay A. Post processing methods used to improve surface finish of products which are manufactured by additive manufacturing technologies : A review. Journal of The Institution of Engineers (India): Series C. 2018;**99**(4):481-487. DOI: 10.1007/s40032-016-0340-z

[25] Bai Y, Williams CB. An exploration of binder jetting of copper. Rapid Prototyping Journal. 2015;**21**(2):177-185. DOI: 10.1108/RPJ-12-2014-0180

[26] Miyanaji H, Rahman KM, Da M, Williams CB. Effect of fine powder particles on quality of binder jetting parts. Additive Manufacturing. 2020;**36**:1-10. DOI: 10.1016/j.addma.2020.101587

[27] Romano T, Migliori E, Mariani M, Lecis N, Vedani M. Densification behaviour of pure copper processed through cold pressing and binder jetting under different atmospheres. Rapid Prototyping Journal. 2022;**28**(6):1023-1039. DOI: 10.1108/RPJ-09-2021-0243

[28] Bai Y, Wagner G, Williams CB. Effect of particle size distribution on powder packing and sintering in binder jetting additive manufacturing of metals. Journal of Manufacturing Science and Engineering. 2017;**139**(8):1-6. DOI: 10.1115/1.4036640

[29] Kumar A, Bai Y, Eklund A, Williams CB. Effects of hot isostatic pressing on copper parts fabricated via binder jetting. Procedia Manufacturing. 2017;**10**:935-944. DOI: 10.1016/j.promfg.2017.07.084

[30] Yegyan Kumar A, Wang J, Bai Y, Huxtable ST, Williams CB. Impacts of process-induced porosity on material properties of copper made by binder jetting additive manufacturing. Materials and Design. 2019;**182**:108001. DOI: 10.1016/j.matdes.2019.108001

[31] Jadhav SD, Dadbakhsh S, Vleugels J, Hofkens J, Van PP, Yang S, et al. Influence of carbon nanoparticle addition (and impurities) on selective laser melting of pure copper. Materials. 2019;**12**(15):1-17. DOI: 10.3390/ma12152469

[32] Lores A, Azurmendi N, Agote I, Zuza E. A review on recent developments in binder jetting metal additive manufacturing: Materials and process characteristics. Powder Metallurgy. 2019;**62**(5):267-296. DOI: 10.1080/00325899.2019.1669299

[33] Binder Jetting and FDM vs Powder Bed Fusion and Injection Moulding. Available from: https://www.metal-am.com/articles/binder-jetting-fdm-comparison-with-powder-bed-fusion-3d-printing-injection-moulding/. [Accessed: August 1, 2022]

[34] Bai Y, Williams CB. The effect of inkjetted nanoparticles on metal part properties in binder jetting additive manufacturing.

Nanotechnology. 2018;**29**(39):1-11. DOI: 10.1088/1361-6528/aad0bb

[35] Asano K, Tsukamoto M, Sechi Y, Sato Y, Masuno S, et al. Laser metal deposition of pure copper on stainless steel with blue and IR diode lasers. Optics and Laser Technologies. 2018;**107**:291-296. DOI: 10.1016/j.optlastec.2018.06.012

[36] Ono K, Sato Y, Higashino R, Funada Y, Abe N, Tsukamoto M. Pure copper rod formation by multibeam laser metal deposition method with blue diode lasers. Journal of Laser Applications. 2021;**33**(1):012013. DOI: 10.2351/7.0000322

[37] Zhang X, Sun C, Pan T, Flood A, Zhang Y, Li L, et al. Additive manufacturing of copper – H13 tool steel bi-metallic structures via Ni-based multi-interlayer. Additive Manufacturing. 2020;**36**:101474. DOI: 10.1016/j.addma.2020.101474

[38] Zhang X, Pan T, Flood A, Chen Y, Zhang Y, Liou F. Investigation of copper/stainless steel multi-metallic materials fabricated by laser metal deposition. Materials Science and Engineering: A. 2021;**811**:141071. DOI: 10.1016/j.msea.2021.141071

[39] Stepien L, Gruber S, Greifzu M, Riede M, Roch A. Pure copper: Advanced additive manufacturing. In: Shishkovsky IV, editor. Advanced Additive Manufacturing. London, UK: IntechOpen; 2022. DOI: 10.5772/intechopen.103673

[40] Yadav S, Paul CP, Jinoop AN, Rai AK, Bindra KS. Laser directed energy deposition based additive manufacturing of copper: Process development and material characterizations. Journal of Manufacturing Processes. 2020;**58**:984-997. DOI: 10.1016/j.jmapro.2020.09.008

[41] Siva Prasad H, Brueckner F, Volpp J, Kaplan AFH. Laser metal deposition of copper on diverse metals using green laser sources. The International Journal of Advanced Manufacturing Technologies. 2020;**107**(3-4):1559-1568. DOI: 10.1007/s00170-020-05117-z

[42] Polenz S, Kolbe C, Bittner F, López E, Brückner F, Leyens C. Integration of pure copper to optimize heat dissipation in injection mould inserts using laser metal deposition. Journal of Laser Applications. 2021;**33**(1):012029. DOI: 10.2351/7.0000303

[43] Liu ZH, Zhang DQ, Sing SL, Chua CK, Loh LE. Interfacial characterization of SLM parts in multi-material processing: Metallurgical diffusion between 316L stainless steel and C18400 copper alloy. Materials Characterization. 2014;**94**:116-125. DOI: 10.1016/j.matchar.2014.05.001

[44] Abdelwahed M, Casati R, Bengtsson S, Larsson A, Riccio M, Vedani M. Effects of powder atomisation on microstructural and mechanical behaviour of l-pbf processed steels. Metals. 2020;**10**(11):1-21. DOI: 10.3390/met10111474

[45] Ledford C, Rock C, Tung M, Wang H, Schroth J, Horn T. Evaluation of electron beam powder bed fusion additive manufacturing of high purity copper for overhang structures using in-situ real time backscatter electron monitoring. Procedia Manufacturing. 2019;**2020**(48):828-838. DOI: 10.1016/j.promfg.2020.05.120

[46] Mahamood RM, Akinlabi ET. Processing parameters optimization for material deposition efficiency in laser metal deposited titanium alloy. Lasers in Manufacturing and Materials Processing. 2016;**3**(1):9-21. DOI: 10.1007/s40516-015-0020-5

[47] Azevedo JMC, CabreraSerrenho A, Allwood JM. Energy and material efficiency of steel powder metallurgy. Powder Technology. 2018;**328**:329-336. DOI: 10.1016/j.powtec.2018.01.009

[48] Nandwana P, Peter WH, Dehoff RR, Lowe LE, Kirka MM, Medina F, et al. Recyclability study on Inconel 718 and Ti-6Al-4V powders for use in Electron beam melting. Metallurgical and Materials Transactions B. 2016;**47**:754-762. DOI: 10.1007/s11663-015-0477-9

[49] Bojestig E, Cao Y, Nyborg L. Surface chemical analysis of copper powder used in additive manufacturing. Surface and Interface Analysis. 2020;**52**(12):1104-1110. DOI: 10.1002/sia.6833

[50] Speidel A, Gargalis L, Ye J, Matthews MJ, Spierings A, Hague R, et al. Chemical recovery of spent copper powder in laser powder bed fusion. Additive Manufacturing. 2022;**52**:1-13. DOI: 10.1016/j.addma.2022.102711

[51] Mirzababaei S, Paul BK, Pasebani S. Metal powder recyclability in binder jet additive manufacturing. The Journal of The Minerals, Metals & Materials Society (TMS). 2020;**72**(9):3070-3079. DOI: 10.1007/s11837-020-04258-6

[52] Roccetti Campagnoli M, Galati M, Saboori A. On the processability of copper components via powder-based additive manufacturing processes: Potentials, challenges and feasible solutions. Journal of Manufacturing Processes. 2021;**72**:320-337. DOI: 10.1016/j.jmapro.2021.10.038

[53] Chen Z, Han C, Gao M, Kandukuri SY, Zhou K. A review on qualification and certification for metal additive manufacturing. Virtual and Physical Prototyping. 2022;**17**(2):382-405. DOI: 10.1080/17452759.2021.2018938

[54] Pereira T, Kennedy JV, Potgieter J. A comparison of traditional manufacturing vs additive manufacturing, the best method for the job. Procedia Manufacturing. 2019;**30**:11-18. DOI: 10.1016/j.promfg.2019.02.003

[55] Dowling L, Kennedy J, O'Shaughnessy S, Trimble D. A review of critical repeatability and reproducibility issues in powder bed fusion. Materials and Design. 2020;**186**:108346. DOI: 10.1016/j.matdes.2019.108346

[56] Lipowsky H, Arpaci E. Copper in the Automotive Industry. Hoboken, NJ, USA: John Wiley & Sons; 2007. p. 123-125. DOI: 10.1002/9783527611652

[57] Copper's Role in Growing Electric Vehicle Production | Paid for and posted by CME Group. Available from: https://www.reuters.com/article/sponsored/copper-electric-vehicle. [Accessed: June 7, 2022]

[58] ExOne and Maxxwell Motors develop Binder Jetting process for copper winding in electric motors | Metal Additive Manufacturing. https://www.metal-am.com/exone-and-maxxwell-motors-develop-binder-jetting-process-for-copper-winding-in-electric-motors/. [Accessed: June 7, 2022]

[59] Markforged Adds Pure Copper to its Metal X Rapid Additive Manufacturing system. Available from: https://www.metal-am.com/markforged-adds-pure-copper-to-its-metal-x-rapid-additive-manufacturing-system/. [Accessed: June 7, 2022]

[60] Pelanconi M, Barbato M, Zavattoni S, Vignoles GL, Ortona A. Thermal design, optimization and additive manufacturing of ceramic regular structures to maximize the radiative heat transfer. Materials and Design. 2019;**163**:107539. DOI: 10.1016/j.matdes.2018.107539

[61] Farsoon Develops Advanced Pure Copper Additive Manufacturing Process. Available from: https://www.metal-am.com/farsoon-develops-advanced-pure-copper-additive-manufacturing-process/. [Accessed: June 7, 2022]

[62] Alloyed's AM Copper Cooling Plate Key Highlight at Formnext - Alloyed. Available from: https://alloyed.com/alloyeds-am-copper-cooling-plate-key-highlight-at-formnext/. [Accessed: June 7, 2022]

[63] Renishaw and nTopology Collaboration Produces Intricate, Pure Copper Structures. Available from: https://www.metal-am.com/renishaw-and-ntopology-collaboration-produces-intricate-pure-copper-structures/. [Accessed: June 7, 2022]

[64] Digital Metal Adds Pure Copper to its Metals Range. Available from: https://www.metal-am.com/digital-metal-adds-pure-copper-to-its-metals-range/. [Accessed: June 7, 2022]

[65] Goldstein R, William Stuehr F, Black M. Design and fabrication of inductors for induction heat treating. In: Rudnev V, Totten G, editors. ASM Handbook: Induction Heating and Heat Treatment. Materials Park, OH, USA: ASM International; 2014;**4C**: 589-605. DOI: 10.31399/asm.hb.v04c.a0005839

[66] Horn TJ, Gamzina D. Additive manufacturing of copper and copper alloys. In: Bourell D, Frazier W, Kuhn H, Seifi M, editors. Additive Manufacturing Processes. Materials Park, OH, USA: ASM International; 2020

[67] Johnson K, Burden E, Shaffer M, Noack T, Mueller M, Walker J, et al. A copper pyramidal fractal antenna fabricated with green-laser powder bed fusion. Progress in Additive

Manufacturing. 2022. DOI: 10.1007/
s40964-022-00268-9

[68] Mayerhofer M, Mitteneder J,
Dollinger G. A 3D printed pure copper
drift tube linac prototype. Review of
Scientific Instruments. 2022;**93**(2):
023304. DOI: 10.1063/5.0068494

[69] Frigola P, Harrysson OA, Horn TJ,
West HA, Aman RL, Rigsbee JM, et al.
Fabricating copper components
with electron beam melting.
Advanced Materials and Processes.
2014;**172**(7):20-24

[70] Home | IFAST. Available from:
https://ifast-project.eu/. [Accessed:
June 7, 2022]

[71] Torims T, Pikurs G, Gruber S,
Vretenar M, Ratkus A, Vedani M, et al.
First proof-of-concept prototype of an
additive manufactured radio frequency
quadrupole. Instruments. 2021;**5**(4):1-12.
DOI: 10.3390/instruments5040035

[72] Torims T, Ratkus A, Pikurs G,
Krogere D, Cherif A, Gruber SS, et al.
Evaluation of geometrical precision
and surface roughness quality for the
additively manufactured radio frequency
quadrupole prototype. Proceedings of
IPAC2022. 2022:787-791. DOI: 10.18429/
JACoW-IPAC2022-TUOXSP3

Chapter 7

Thermal Tuning of Thermophysical Properties of Single Cu-Ni Alloy

Yong W. Kim

Abstract

The great majority of metallic materials in use are not single crystals but disordered. We model such a material specimen as being composed of nanoclusters, each cluster being a small mutually interacting cluster of atoms. In this modeling, a material specimen is then treated as a mixture of nanocrystalline and glassy-state atoms. If we define the degree of crystallinity of the object by the probability that an atom is a member of a crystallite existing within the specimen, the probability would be smaller than unity. Structural disorder in such metallic alloys affects thermophysical properties of the alloy specimen in myriad ways. Transport properties in turn impact material utilization in significant ways to the extent that the specimen could behave as possessing completely different alloy properties. This approach to changing alloy properties can serve useful purposes. We show how one might approach such modification of alloy properties without changing alloy composition with a sample of copper-nickel alloy.

Keywords: nanocrystallites, structural disorder, copper-nickel alloy, thermophysical properties, thermal forcing

1. Introduction

A general theory [1] has been developed for a wide class of metallic alloys. In this theory, such a specimen codifies the structural disorder by means of broad size distributions of nanocrystallites and population of glassy-state atoms of the given alloy elements. It has been established by experiment that the functional form of the nanocrystallite size distribution depends sensitively on the alloy's elemental composition. A model material specimen is then represented by a compactified mixture of nanocrystallites as large molecules, intermixed with constituent atoms in glassy state. A large system of reaction equilibrium equations is solved numerically iteratively to follow the growth or shrinkage of nanocrystallites as the temperature of the alloy medium is varied.

In this approach, an alloy specimen is regarded as a randomly close-packed (RCP) mixture of a population of nanocrystallites and constituent atoms in glassy state. The disorder is then represented by the size distribution function of the nanocrystallites. Under sustained exposure to thermal, stress, nuclear, or chemical forcing at an elevated temperature, the distribution function becomes modified, and this process is predictable for a given forcing condition and thus controllable. Transport of

excitations is affected by the detail of the distribution function, making it possible to control transport properties, all at a fixed alloy composition. The modeling and experimental support will be presented [2].

The reaction of 2-D randomly close-packed (RCP) structures to thermal forcing through a simulated oven experiment was described in previous work [1, 3]. The suggested dissociation of nanocrystallites seen in this experiment lent itself to a modeling approach for the dissociation of nanocrystallites in a RCP system. The treatment of this dissociation is handled by the law of mass action. To start, we must define the room temperature basis for our binary alloy. We model a metallic binary alloy as a mixture of nanocrystallites and glassy atoms. At room temperature, we define the structure of our binary alloy as having a certain mix of these two states. The degree of crystallinity at the binary alloy composition will determine the ratio of glassy matter to nanocrystallites. To define the structure of the nanocrystallites, we use the crystallite size distribution found by combination of our simulated experiment and numerical simulation study for the composition. These parameters for the structure of the binary alloy are composition-dependent, and we use the lessons learned from RCP modeling to determine the room temperature structure of each binary alloy we investigate.

In this study, the nanocrystallite size distribution is changed by sustained thermal forcing at a temperature close to but below the melting point of the given alloy. The specimen is quenched to capture the new equilibrium size distribution of the nanocrystallites at this temperature, and its thermophysical properties are measured. The protocol as described is used at different forcing temperatures for a single copper-nickel alloy specimen at fixed elemental composition. In this chapter, theoretical modeling and forcing experiments will be presented together with measured thermophysical properties resulting from the forcing runs.

2. Thermal forcing

When we acquire a sample of an alloy from a vendor, it is never clearly known what its thermal history is except that we do have reliable pedigree (composition of 55 W% *Cu* and 45 W% *Ni*). Experimentally, we do know from alloy structure study [1] that our new theory gives rise to the average value of the degree of crystallinity at room temperature [1]. **Figure 1** shows how the degree of crystallinity of the specimen would be expected to change after each round of thermal annealing. We define the degree of crystallinity by the average probability that an atom remains to be part of nanocrystallites within the specimen. **Figure 1** is obtained from our theory [1] making use of the Lennard-Jones constants [4, 5], available in the literature for *Cu* and *Ni*.

We note that we view specimen, which is in the form of a wire, 40.5000 cm long and 1.5875 mm in diameter, is often not straight. It contains many small curved segments, which result from unwinding out of the spool and putting in and out of an electric furnace (Fisher Muffle Furnace). For precise measurements, the specimen has been stretched between two end point locations on an optical bench as follows. The end of the copper-nickel wire specimen was flared by a small hammer to serve as an anchor by means of a metal-ceramic latch in an electrically insulating manner. The opposite end is held in a similar manner. One end of the specimen is struck by the bob of a charged pendulum made of a conductor to charge a grounded capacitor (ceramic capacitor, 0.02 microfarad), generating a short pulse from the pendulum in order to generate a narrow electrical pulse to trigger an oscilloscope (digital oscilloscope 400 MHz bandwidth at 400 M bites per second digitization rate). At the end of the
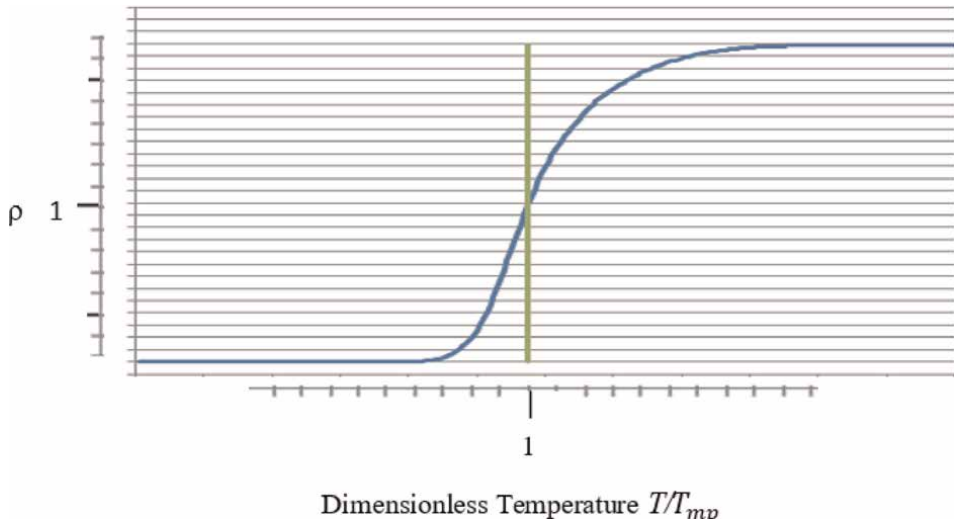
Figure 1.
The dimensionless number density ρ of glassy-state atoms, where $\rho = n/n_o$ and n is given per unit volume, versus dimensionless temperature for the alloy T/T_{mp}. T_{mp} denotes the melting point of the alloy; the intersection of the green line with the blue line in the figure corresponds to unity in dimensionless temperature. n_o denotes the number of single isolated atoms in glassy state at melting point per unit volume.

wire, specimen is pressed by a spring-loaded transducer (piezoelectric), whose output is displayed in the oscilloscope, thus making the determination of the time of flight of the mechanical pulse (acoustic pulse) to travel the full length of the specimen [6].

On further consideration of any bends in the wire specimen, we have prepared a fixture for straightening the wire specimen. The fixture is designed not to compress nor to stretch the specimen after each annealing treatment, as follows. Two long slabs of an optical bread board made out of aluminum, each with a full row of a straight groove machined out between the two rows of threaded holes, and the heat-treated specimen is sandwiched along the full length of the boards, facing each other. The wire specimen is trapped within the two long 90-degree V-grooves facing each other, the two sides of the wire specimen pressed by aluminum walls gently against each other by means of long screws threaded into the rows of holes on either side of the long grooves. This arrangement allows the measurement of the length of the specimen before and after each annealing round. This type of fixtures can be readily prepared in a machine shop.

The interior of a furnace is typically three-dimensional chamber and cube-shaped, and, consequently, the specimen must be bent into a winding roll to be within a furnace. The above-mentioned wire straightener fixture resolves the chores of reshaping the wire specimen before and after the annealing run, while the annealing could be carried out in an inert atmosphere.

As the temperature the specimen may encounter the effect of oxidation as one approaches the melting temperature of the alloy, we developed a method of putting the specimen within a long stainless tubing capped with all-metal (stainless steel) Swagelok's (Parkin-Hannifin). The protective tubing used was 6 mm in outer diameter. The protective tubing can be evacuated and filled with argon and sealed after the wire specimen is inserted. The assembly may easily rolled up in order to insert into the furnace and retrieve the annealed specimen after annealing.

3. Theoretical considerations

The size of nanocrystallites that make up a real alloy specimen changes as a result of annealing. The very interesting question is what happens to the length and volume of the specimen due to annealing and quenching of the specimen. It is also important to know how stable would the size distribution of nanocrystallites be because the new distribution function determines the thermophysical properties of the alloy specimen. The motion of an atom is governed by the size of the energy that binds it to a site relative to available thermal energy, whereas energy variation experienced in normal applications is usually very small.

Another to ask is how the thermal evolution of the nanocrystallite population impacts the thermophysical properties of disordered metallic solids as the temperature is raised. The model calculations have clearly shown that not only the number of the nanocrystallites diminishes in population but also the functional form of their size distribution undergoes significant changes at elevated temperatures. These changes lead to changes in packing fraction of the alloy specimen. From the definition of the degree of crystallinity, which measures the probability that an atom belongs to a nanocrystallite, we can derive the packing fraction of glassy matter, η_{gl}, expressed in terms of the degree of crystallinity, γ, the packing fraction η_{cp} when the alloy medium is crystalline and the packing fraction η_{rcp} when the medium is disordered. We use the composite value for the average packing fraction as compiled by Berryman [7] for the latter. The expression for the packing fraction of fully glassy matter can be found as follows:

$$\eta_{gl} = \frac{(1-\gamma)\eta_{rcp}\eta_{cp}}{\eta_{cp} - \gamma\eta_{rcp}}. \tag{1}$$

For a given alloy specimen η_{gl} is always smaller than either η_{cp} or η_{rcp}, and a transition of crystalline particles into the glassy state of matter directly leads to a volume expansion. It thus impacts thermal expansion of the specimen; this contribution is new and additional to the usual definition of thermal expansion. We propose that the simplest way to incorporate the contribution into the alloy model is to treat the thermal expansion in nanocrystallites and in glassy matter separately from the change of the relative populations of atoms within nanocrystallites and atoms in glassy state of matter. Upon heating, the nanocrystallites within the specimen expand according to the crystalline expansion coefficient. Glassy matter of the specimen would also expand but according to the average expansion coefficient of metallic glass. Both of these expansion coefficients are knowable in principle from the literature.

In prescribing the linear expansion coefficient for a disordered alloy in a functional form, one can express the contributions from these effects to the volume of the specimen as a function of temperature in the following form:

$$V(T) = V(T_o)\Big[\gamma(T)\{(1 + \beta_{cr}(T)(T - T_o)\} + \{1 - \gamma(T)\}\Big(1 + \beta_{gl}(T)(T - T_o)\Big)\}\Big] \tag{2}$$

$V(T)$ and $V(T_o)$ denote the volume of the specimen at temperature T and at a reference temperature T_o, respectively. $\beta_{cr}(T)$ and $\beta_{gl}(T)$ are the volume expansion coefficient at temperature T of the crystallites and glassy matter, respectively. The volume expansion is written out as the sum of the expansions of the nanocrystallites

and glassy matter. The new contribution is included into $\gamma(T)$, which measures the movement of the population of ordered crystalline atoms in the specimen when the temperature is raised [3].

In the conventional treatment, no distinction is made of the nanocrystallites separately from the glassy matter in writing out the linear expansion coefficient; their relative populations are assumed to remain fixed. In the present treatment, the fraction of nanocrystallites in the specimen changes when the temperature is raised, and this change can be determined by first-principle calculation.

4. Concluding remarks

Theoretical analyses of the above kind were carried out for the following singeatom metals: Ag, Al, Au, Ca, Ce, Cu, Ir, Ni, Pb, Pd, Pt, Rh, Th, Ba, Cr, Fe, K, Li, Na, Nb, Rb, Ta, V, W, Be, Cd, Co, Dy, Er, Hf, Mg, Re, Ru, Ti, Tl, Y, Zn, and Zr.. Similar calculations were carried out for binary disordered metallic alloys $AlTi$, Al_3Ti, $AlTi_3$, $AuCu$, and $AuCU_3$. All calculations showed results of the types consistent with those shown in **Figure 1** with varying degrees of agreement for the melting points with known experimentally determined melting point data.

We had a successful thermal forcing run. A 0.382-M-long wire specimen of 55 W% in copper and 45%W% in nickel was used for this run. When forced at 940 K for 16.45 h and the specimen was quenched in water at 10°C, the measured speed of longitudinal sound pulse at room temperature was found to be increased to 5744.36 M/s from the speed of sound in untreated specimen, off the shelf, at 4235.03 M/s. This is an increase by 35.64 percent.

The change of metallic alloy's thermophysical properties stems from the modifications of the equilibrium distribution functions of nanocrystallites within the system by slow thermal forcing (over 15 hours at a selected temperature) at high temperatures (at temperatures above one half of the melting point), and therefore, it is reasonable to expect that the thermophysical property of the system will most likely to remain as modified throughout normal utilization of the material. The melting point of the alloy used here is given to be 1507 K.

The structural disorders that are pertinent in the context of the present discussion may arise partly from the rough (approximate) handling in material processing stages or partly from trace-level impurities that remain within the alloy-making, and these should be considered intrinsic to the industry, and therefore, the current state of the art may present many useful opportunities to be exploited.

Author details

Yong W. Kim
Department of Physics, Lehigh University, Bethlehem, USA

*Address all correspondence to: ywk0@lehigh.edu

IntechOpen

References

[1] Cress R, Kim YW. Statistical physics modeling of disordered metallic alloys. In: Glebovsky VG, editor. Progress in Metallic Alloys. IntechOpen, London, UK; 2016

[2] Cerny R. Crystal structures from powder diffraction: Principles, difficulties and progress. Crystals. 2017; **7**:142

[3] Kim YW, Raffield JH. Sound propagation in thermally-forced copper-nickel alloy. High Temperatures-High Pressures. 2017;**46**:271-280

[4] Zhen S, Davies GJ. Calculation of the Lennard-Jones N-m potential energy parameters for metals. Physica Status Solidi. 1983;**78**:595-618

[5] Kong CL. Combining rules for intermolecular potential parameters. II. Rules for the Lennard-Jones (12–6) potential and the morse potential. The Journal of Chemical Physics. 1973;**59**: 5-23

[6] Goodrich CP et al. Jamming in finite systems: Stability, anisotropy, fluctuations, and scaling. Physical Review E. 2014;**90**:022138

[7] Berryman JG. Random close packing of hard spheres and disks. Physical Review. 1983;**A27**:1053

*Edited by Daniel Fernández-González
and Luis Felipe Verdeja González*

Copper has been an important metal throughout history. Initially, it was used as raw material for the manufacture of tools, weapons, ornamental objects, and more. The later discovery of copper alloys, such as bronze and brass, extended the use of this metal alloy to many different fields based on its mechanical, corrosion, and wear resistance. Nowadays, copper is mainly used in the electrical and thermal conductivity fields, although new uses are being discovered. This book provides a comprehensive overview of copper in two sections on copper mining and processing and copper applications.

IntechOpen